Therapeutic applications for pulsed laser and ultrasound

By David Hazlewood

Submitted to the graduate degree program in Bioengineering Department and the Graduate Faculty of the University of Kansas in partial fulfillment of the requirements for the degree of Doctor of Philosophy.

Chair: Dr. Xinmai Yang

Dr. Jinxi Wang

Dr. Kenneth Fischer

Dr. Lorin Maletsky

Dr. Sara Wilson

Dr. Christopher Fischer

Date Defended: 15 July 2019

The dissertation committee for David Hazlewood certifies that this is the approved version of the following dissertation:

Therapeutic applications for pulsed laser and ultrasound

Chairperson: Dr. Xinmai Yang

Date Approved: 15 July 2019

Abstract

Arthrofibrosis is a condition that causes a painful reduction in joint range of motion, which is caused by a buildup of scar tissue in and around joint. The overall goal of this research project was to develop new non-invasive treatments for the buildup of scar tissue that can occur in joints after major injury or surgeries. Pulsed high intensity laser (PHIL) and pulsed high intensity focused ultrasound (PHIFU) are two methods that have been identified as having the potential to provide a non-invasive method of breaking down scar tissue. These methods can also be combined into a treatment called photo-mediated ultrasound therapy (PUT). These new treatment methods create a stress wave inside the scar tissue without breaking the skin. The strong stress waves physically pull the dense fibers in the scar tissue apart, releasing the stiffness in the joint. These noninvasive treatments can be repeated to slowly break down the scar tissue over the course of several weeks, allowing the body to heal without new scarring.

To test the effectiveness of PHIL, PHIFU, and PUT an appropriate animal model must be developed. This animal model used rabbits and involved a single surgery to create scar tissue in posterior capsule of one of the hind limbs. The range of motion (ROM) of the operated leg was compared to the ROM of the non-operated leg to demonstrate significant loss in joint function. Once the animal model had been established PHIL, PHIFU, and PUT were performed twice weekly on the operated leg. ROM was measured as the primary metric for success. All three treatments were successful and resulted in the same ROM in both the operated and non-operated knees. In vitro experiments were performed on tissue phantoms to explore the underlying mechanisms behind these treatments. Numerical simulations of PUT were performed to explore potential optimizations in treatment parameters. The results of this research is compiled in this dissertation along with ideas on the future direction of the research.

Acknowledgements

I would like to sincerely thank the many people who have supported me throughout my PhD process. I have received help from more people than I could possible list here, and I could not have made it without all of them supporting me through this journey.

I would first like to thank my advisor Dr. Xinmai Yang. His mentorship and guidance have been invaluable in developing the skills needed to be an engineer and a scientist. Additionally, his kindness and patience has helped me through some of the most difficult times my family and I have been through. Dr. Yang has helped me to branch out into many areas a research including experimental design, product development, theoretical work, and numerical simulations. The time that I have spent is his lab has been a gift, one that I will forever be grateful for.

I would also like to thank the members of my committee, Dr. Jinxi Wang, Dr. Kenneth Fischer, Dr. Lorin Maletsky, and Dr. Christopher Fischer. There comments and suggestions for my research have been invaluable, and this dissertation would not have been completed without them.

I would also like to thank my coworkers during my time here, Nima Nejadsadeghi, Rohit Singh, and Madhumithra Karthikes have all been a great help and support. Additionally, Morgan Alters, Jiajun Lui, and Hongrui Zhu have been wonderful collaborators and a variety of projects that helped to expand the research experiences I was able to have during my graduate career

I also need to give the deepest thanks to my family especially my parents Richard and Kathleen Hazlewood. They have provided me with a wealth of support, both emotionally and financially in order to make this PhD possible. My children Lillian, Lavender, and Lupin who gave me a

reason push myself to become the best person I could be and were always understanding through the whole process.

Finally, I would like to thank my wife Elizabeth Woods, who has always supported me as a friend and then as a partner. When we began dating I was a recent college dropout, but she helped me see in myself the potential that others had seen but I never could. Everything meaningful that I have been able to accomplish has been due to her support and encouragement, and I would be completely lost without her.

Table of contents

List of tables

List of figures

Chapter 1 - Introduction

1.1 Motivation

Arthrofibrosis is a debilitating condition where a buildup of scar tissue in a joint causes a painful reduction in range of motion (ROM). Any severe injury or surgery to a joint can cause arthrofibrosis, however more invasive the injuries or surgeries are more likely to result in scarring. This condition can occur in nearly any joint in the body including shoulders (Le, Lee, Nazarian, & Rodriguez, 2017; Wolin, Ingraffia-Welp, Moreyra, & Hutton, 2016), elbows (Wu et al., 2015), or knees (Cheuy et al., 2017; Cosgarea, DeHaven, & Lovelock, 1994; Petsche & Hutchinson, 1999; A. Schiavone Panni, S. Cerciello, M. Vasso, & M. Tartarone, 2009; Schwarzkopf, William, Deering, & Fitz, 2013; Shelbourne & Patel, 1999). For example, in the shoulder arthrofibrosis is often caused by repeated use, causing adhesive capsulitis. A condition that affects an estimated 5% of the population in the US costing $7 billion in direct costs every year (Wolin et al., 2016). In the elbow arthrofibrosis is commonly seen after injuries and occurs in 15% of all fractures, dislocations, and torn tendons (Wu et al., 2015). In the knee arthrofibrosis is commonly seen as a complication after a surgical procedure, occurring in 18% of ACL repairs (Mayr, Weig, & Plitz, 2004) and up to 13% of total knee arthroplasty (TKA) (Cheuy et al., 2017).

Arthrofibrosis in the knee is of particular concern because small changes to ROM can have a profound change in gait and mobility. A reduction of only 10° of extension is considered severe and generally requires surgical interventions (J. G. Enad, 2014; J. R. Hutchinson, E. N. Parish, & M. J. Cross, 2005; Mitsuyasu et al., 2011b; Perry, 1987; A. Schiavone Panni et al., 2009; Schwarzkopf et al., 2013; Tardy et al., 2016; Wong, Trudel, & Laneuville, 2015). According to Veteran Affairs Schedule for Rating Disabilities, a reduction in maximum extension of 30° in the knee is comparable to a below the knee amputation.

Unfortunately, arthrofibrosis of the knee is also relatively common due to the large number of knee replacement surgeries or TKA performed every year. TKA is often the ultimate treatment of osteoarthritis in the knee. Currently there are over 700,000 TKA performed every year (Cheuy et al., 2017). By 2030 this number is expected to reach 3,500,000 per year due to the aging population. Even with modest improvements to arthrofibrosis rates there will be hundreds of thousands of new arthrofibrosis patients every year in the US due to knee replacements alone.

1.2 Scar tissue overview

To properly understand how to treat arthrofibrosis it is important to understand the pathology of fibrosis in general. Fibrosis or scarring occurs when myofibroblasts build up an excess of extra cellular matrix (ECM). The ECM in scars is primarily composed of collagen-1 fibers, which are particularly stiff compared to other ECM materials such as elastin (Kendall & Feghali-Bostwick, 2014). Collagen rich ECM is important for normal wound healing to draw together and hold separated tissues. Unfortunately, excessive ECM can prevent normal function of the soft tissue.

During normal wound healing to a penetrating injury, the body will generate platelet activity and an inflammatory response which will release inflammasomes (Gasse et al., 2007) and cytokines (Di Vita et al., 2006) to signal the immune system. Next mast cells will cause swelling to reduce blood flow, while immune cells arrive to consume bacteria and damaged cells. At the same time fibroblasts are recruited to provide ECM. The previously released cytokines, particularly transforming growth factor beta (TGF-β), will signal the fibroblasts to be converted into myofibroblasts (Watson et al., 2010), which will build up dense ECM with a higher ratio of collagen-1 while applying actin molecules to create additional tension and cross linkages in the collagen fibers. Once the wound has been closed the myofibroblasts should either return into

fibroblasts or go through apoptosis, allowing normal cell proliferation through the ECM to resume with a gradual return to normal function.

Fibrosis follows a nearly identical process as normal wound healing. The main difference is that there is a dramatic increase in inflammatory response and myofibroblast activity. Under these conditions dense ECM is rapidly placed down with thick bundles of collagen which have many disorganized cross linkages (Linares, Kischer, Dobrkovsky, & Larson, 1972). Additionally, myofibroblasts remain active for a longer time, beyond the point of wound closure. The ECM eventually becomes so dense that it becomes cell free and no longer degrades as it should (Sivakumar, Kitson, & Jarai, 2019).

Usher et al. identified multiple positive feedback loops which appear responsible for the unchecked nature of fibrosis (Usher et al., 2019). For example, the initial inflammatory response which starting the healing process is amplified by many of the recruited cells, which release additional inflammatory cytokines. The cytokine TGF-β, which is produced by myofibroblasts among other cells, causes fibroblasts to become myofibroblasts and prevents apoptosis (Watson et al., 2010). This prevents the normal removal of myofibroblast (apoptosis or becoming fibroblasts). As the myofibroblasts pull on the tissue they create mechanical stresses which the body detects as new injuries. Eventually the ECM becomes so dense that the blood supply is interrupted resulting in hypoxia which causes an acidic environment in which TGF-β is more effective (Ruthenborg, Ban, Wazir, Takeda, & Kim, 2014). Finally, prolonged inflammation causes epigenetic changes to the DNA of myofibroblasts which gives them a memory, and when they revert to fibroblasts they will be able to convert back into myofibroblasts more readily (Hinz et al., 2012).

One reason that fibrosis can be so devastating is it is designed to create rapid and strong connections and to wall off the injury site (Ferguson & O'Kane, 2004). The large immune response

during fibrosis was more useful before the very recent advances in sterility and antibiotics. Furthermore, for the vast majority of life on earth, a severe injury to a joint would be fatal. To survive, an organism needs to be able to find food and avoid predators, which is impossible if it needs to rest for several months to recover from an injury. The need to stay mobile to survive puts a limit on survivable injuries. Our body uses similar wound healing mechanisms for both large and small injuries. However, the controls to the healing system do not scale up as efficiently, which sometimes results in unregulated fibrosis (Usher et al., 2019). The scar tissue is generally inferior to the tissue it replaces. The tissue density and lack of cells prevent vascularization to supply of blood and nutrients. The dense ECM is also much stiffer due to the higher ratio of collagen-1 fibers and is under tension, which can put stress on the surrounding tissues and prevent normal motion. Despite the additional stiffness in scar tissue and density of the ECM, the tensile strength is reduced due to the more chaotic alignment of the fibers (Shah, Foreman, & Ferguson, 1994). Additionally once mature scar tissue has formed there is no specific biological pathway for its natural removal, which means that remodeling can be quite slow. (Ferguson & O'Kane, 2004).

1.3 Anatomy and pathology of arthrofibrosis in the knee

When looking at arthrofibrosis in the knee, it may be widespread throughout the knee or it may be more focused, effecting one or more area. In this section several of the common locations where arthrofibrosis occurs in the knee are presented.

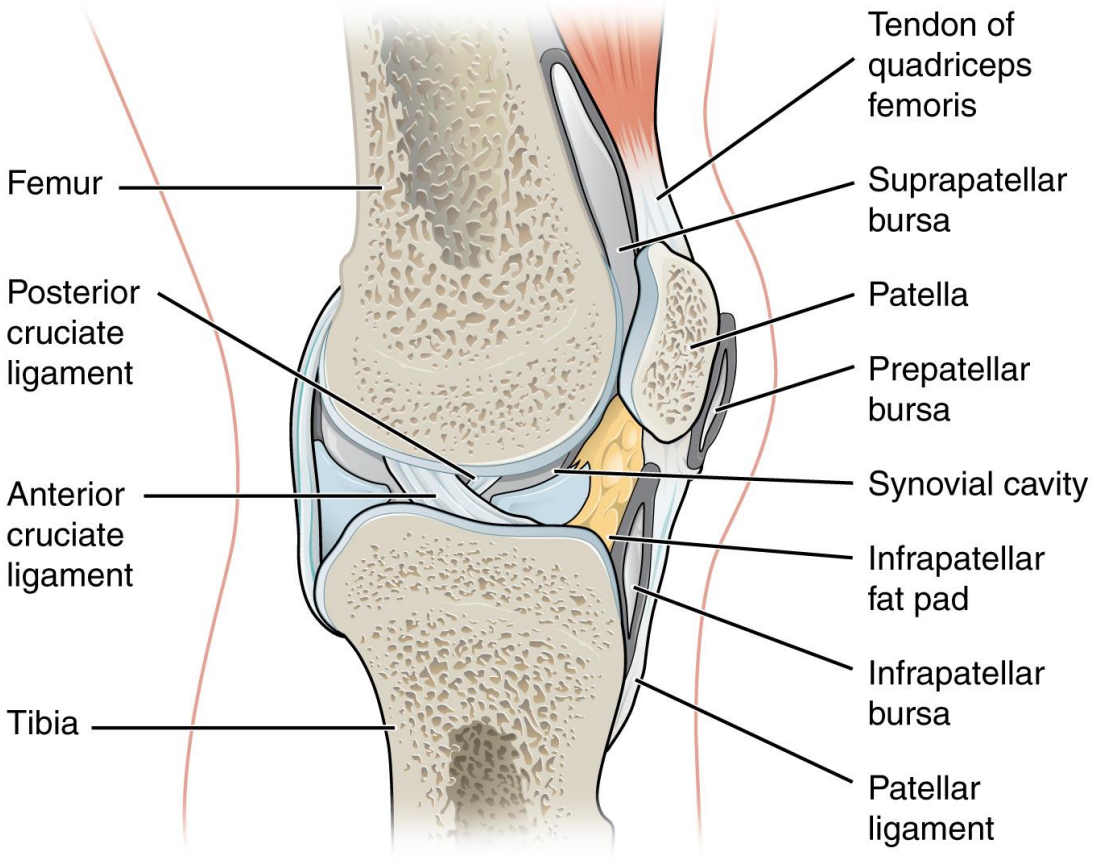

Figure 1.1: A cross sectional diagram of the knee. The bursa are empty spaces that can easily become constricted through arthrofibrosis.

Inter-articular adhesions are among the most common presentation of arthrofibrosis in the knee, with the scar tissue forming between the femur and tibial plateau. This results in stiffness and pain with use of the joint, while also causing long-term damage to the cartilage of the joint from misalignment of the contact surfaces (X. Li et al., 2013). Cyclops lesion is the formation of a fibrous mass in the intercondylar arch of the femur, which is normally only present after ACL repair (Jackson & Schaefer, 1990). While cyclops lesions are present in 25-33% of patients, only 1-9% of patients will display symptoms which will require surgical removal of the lesion (Facchetti et al., 2017). However, if the cyclops lesion becomes impinged with the ACL graft, or otherwise prevents normal extension, removal is required (Fullerton & Andrews, 1984). Fibrosis

can also build up in the synovial space around the femoral condyles. These adhesions connect the medial and lateral sides of the joint capsule to the femoralcondyles (Kim, Gill, & Millett, 2004).

Arthrofibrosis also occurs in the anterior side of the knee in the spaces and tissues around the patella. The suprapatellar pouch is the bursa behind the suprapatellar tendon which connects the quadriceps to the patella. This pouch should remain empty to allow for changes in shape size as the knee bends. When it becomes fibrotic the suprapatellar pouch closes and tightens, reducing mobility of the patella, while at the same time limiting the maximum flexion in the knee. Similarly, Hoffa's syndrome is caused by fibrosis in the infrapatellar fat pad (IFP), which is located distal to the patella. Hoffa's syndrome shifts the patella towards the tibia resulting in reduced patellar mobility by preventing the patella from shifting towards the femur during extension. The anterior interval which is located between the tibial plateau and the IFP can become fibrotic, closing the space and reducing the mobility of the IFP and therefore the patella. This has been shown to increase the patellar femoral force, which in addition to pain and stiffness contributes to osteoarthritis over time (Mikula et al., 2017).

The posterior aspect of the knee is primarily composed of the posterior joint capsule and the insertion of the popliteal tendon. However, it is important to note that the popliteal vein, popliteal artery, and the tibial nerve all run down the back of the knee complicating surgery to the area (Al-Turkaiki, 1986). When arthrofibrosis is present in the posterior capsule, it becomes stiffened and the femoral and tibial ends are pulled together. Additional adhesions also connect the capsule to the bones of the knee which prevent the normal motions of the joint capsule during knee motion. As a result, arthrofibrosis in the posterior capsule can be particularly detrimental to maximum extension of the knee and general mobility. Furthermore, arthroscopic surgery is difficult, and

open surgery is often required to perform capsular release (Gomes, Leie, de Freitas Soares, Ferrari, & Sanchez, 2017).

Due to the substantial role of inflammation in arthrofibrosis (or fibrosis in general), one of the main methods of prevention is to minimize the trauma to the body. Therefore, non-surgical methods such as physical therapy and non-steroidal anti-inflammatory drugs (NSAIDs) are always exhausted first before surgery is considered. If surgery is required, the surgeon focuses on avoiding unnecessary damage by always attempting the least invasive method, such as performing arthroscopic release instead of open surgical release.

Any patient with arthrofibrosis will receive non-steroidal anti-inflammatory drugs (NSAIDs) and aggressive physical therapy (PT), to minimize scarring. During PT, patients are encouraged to use the joint to break apart early ECM formation to prevent contracture of the soft tissue. Aggressive exercise is needed, but patient compliance can be low during this period due to the pain (Kurosaka, Yoshiya, Mizuno, & Yamamoto, 2002). PT which is too aggressive may result in injury or an increased level of inflammation, contributing to future arthrofibrosis (Cheuy et al., 2017). If arthrofibrosis is present the first option is manipulation under anesthesia (MUA), where the joint is forcibly extended rupturing the scar tissue while the patient is under anesthesia. MUA is unfortunately only successful when administered before the scar tissue matures, requires at least 6 weeks of rehabilitation, and may result in new bone fractures or soft tissue trauma (Ipach, Schafer, Lahrmann, & Kluba, 2011; Issa et al., 2014). The next option is surgical intervention to release or remove the scar tissue, which also requires significant rehabilitation. Surgical release may by performed arthroscopically or through open surgery (Ghani, Maffulli, & Khanduja, 2012). Severe scarring requires more invasive surgical procedures for removal, but more invasive the surgeries have a higher risk of new scarring (J. G. Enad, 2014; Schwarzkopf et al., 2013; Werner,

Cancienne, Miller, & Gwathmey, 2015; Wu et al., 2015). If arthrofibrosis was caused by a surgical implant, a final treatment option is a replacement of the implant through a revision surgery. While on average a revision improves a patient's ROM, there is also a significant risk of complications and low patient satisfaction with this treatment (Cheuy et al., 2017; Rutherford et al., 2018). Approximately thirty percent of all patient receiving a revision for arthrofibrosis end up with reduced ROM due to the surgery (Rutherford et al., 2018). The result is a significant population of patients who have undergone a series of surgical procedures, and months or years of rehabilitation and disability, who will never achieve normal knee function. It is difficult to determine the actual number of patients who suffer from arthrofibrosis with reported rates ranging from 8% to 60% (Fitzsimmons, Vazquez, & Bronson, 2010). This wide range is likely due to disagreement on the definition of arthrofibrosis and under counting in many studies (Usher et al., 2019). There are likely many patients who suffer from arthrofibrosis being uncounted because current research typically only tracks the rates of surgical interventions (Werner et al., 2015). As a result, some of the worst patients will not receive surgery due to their high risk of complications and will be excluded from most reporting. Additionally, there may be many patients with milder arthrofibrosis who have avoided surgical intervention due to the risks.

Due to the difficulties in treating arthrofibrosis with the current plan of care it is clear to see that there is a need for new treatments. The new treatment would ideally be minimally invasive to avoid triggering inflammation or scarring. Additionally, new treatments should be highly selective in treating only the scarring in the joint, so that it can be applied in all of the regions of the knee (or other joints) without causing complications. Pharmaceutical solutions, generally targeting TFG-β, are currently under development to prevent the feedback loops causing excessive scarring (Ferguson & O'Kane, 2004; Shah et al., 1994; Watson et al., 2010). However due to the lack of a

biological pathway for efficient scar tissue removal, these treatments are unlikely to be beneficial for patients who already suffer from arthrofibrosis (El Agha et al., 2017; Ferguson & O'Kane, 2004).

1.4 Mechanical disruption of scar tissue through laser and ultrasound

In this manuscript investigations into whether strong pressure waves can be used to mechanically disrupt scar tissues will be performed. The goal is to provide pressure waves which will break apart the collagen-1 rich ECM found in scar tissue. Breaking apart the ECM has two main goals. First by separating the ECM the tension in the tissue will be reduced. Secondly by breaking up the ECM it may be possible for other cells to enter the tissue, allowing it to return to normal function. To generate the necessary pressure waves high intensity focused ultrasound (HIFU), pulsed laser, and combined laser/HIFU treatments will be explored. The treatments are performed using high intensity pulses with very low duty cycles. The high intensity is needed to break apart the stiff collagen-1 fibers, and the low duty cycles are used to prevent a thermal build up which is known to tighten tissue (Lee et al., 2012; Woodward, Fabi, Alster, & Colon-Acevedo, 2014). High amplitude pressure waves can fracture material due to the high compressive and rarefactional pressures. Additionally, there are other mechanical effects such as cavitation, acoustic streaming, and acoustic radiation forces, all of which can be damaging to soft tissue (Daoudi et al., 2017; Feril et al., 2008).

Cavitation occurs when a rarefactional pressure wave causes a separation of a liquid medium (Leighton, 1994). This separation requires a nucleation point, which is usually a nanobubble. If a negative pressure is applied the bubble will grow, and if a positive pressure is applied the bubble will shrink. If the size fluctuations are large enough, a process call inertial cavitation occurs where

the bubble collapses and a shock wave is produced when opposite sides of the bubble crash into each other. The range of the shock wave is of a similar size to the maximum size of the bubble prior to collapse. Inertial cavitation is known to have a defined pressure threshold, where any pressure waves below that threshold cause bubble oscillations instead of collapse (Deng, Xu, Apfel, & Holland, 1996; Hynynen, 1991). By utilizing inertial cavitation our treatment will have a more sharply defined treatment area compared to thermal ablation which can cause damage to the surrounding tissue as the heat spreads.

1.4.1 Pulsed high intensity focused ultrasound (PHIFU)

HIFU utilizes a spherically shaped ultrasound transducer, which allows the generated ultrasound waves to converge at a focal point, where they will have a much higher amplitude. The location of the focal point will be based on the radius of curvature in the transducer. By placing the transducer in such a way that the focal point is inside the tissue, the skin can avoid damage because the ultrasound intensity is lower, as seen in Figure 1.2. This allows for HIFU to internal lesions without the risk of external infection. Furthermore, the lesions will be smaller and can heal without triggering a significant immune response.

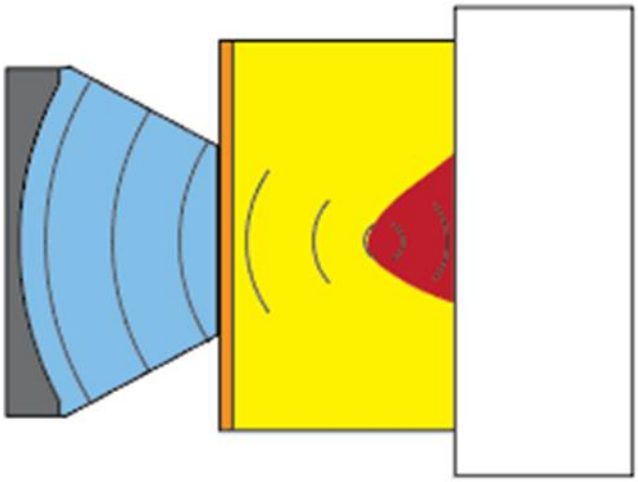

Figure 1.2: A diagram of HIFU traveling through skin and subcutaneous fat to treat a mass of scar tissue near a bone. As the ultrasound waves become more focused near the focal point they also become much stronger. The strength of the ultrasound waves near the skin can be much lower relative to the targeted area.

Previous surgical uses of HIFU are generally based around thermal ablation (Tavakkoli & Sanghvi, 2011). Where a continuous application of high intensity ultrasound waves causes a rise temperature until cell death and coagulation occurs. Alternatively, for the treatments pulsed HIFU (or PHIFU) waves with higher intensity but bursts $\leq$ 1 ms in duration with a pulse repetition frequency (PRF) of 5-30 Hz were used. By avoiding the thermal effects normally associated with HIFU it was possible to apply even larger amplitude pressure waves, resulting in larger mechanical effects.

PHIFU is appropriate in attempting to break down scar tissue due its noninvasive nature, and the concentrated treatment around the focal area. Additionally, it is relatively low cost compared to surgical options, and physical therapists and surgeons are familiar with the use of ultrasound for imaging and thermal applications. On the other hand, one disadvantage to PHIFU is that it will strongly affect whatever tissue is located in the focal point. This means that the exact location of

the scar tissue (or other targeted tissue) relative to the HIFU transducer must be known through some other imaging method.

1.4.2 Pulsed high intensity laser (PHIL)

The second method of generating pressure waves we explored was pulsed high intensity laser (PHIL) to target optically absorbent tissues. This techniques is based around the photoacoustic effect (McDonald & Wetsel, 1978). The photoacoustic effect occurs when a very short laser pulse hits an optical absorber. If the laser pulse has a duration shorter than the thermal relaxation time of the absorber, then highly localized thermal expansion occurs which generates an ultrasound wave. The ultrasound wave will then spread out from the absorber (as seen in Figure 1.3) and can be detected through an ultrasound transducer through a process known as photoacoustic imaging (PAI) (L. V. Wang & Hu, 2012; L. V. Wang & H. Wu, 2007; H. F. Zhang, Maslov, Stoica, & Wang, 2006). The resulting PAI signal often has a small amplitude due to spherical spreading, but can be extremely destructive near the optical absorber (Paltauf & Schmidt-Kloiber, 1999).

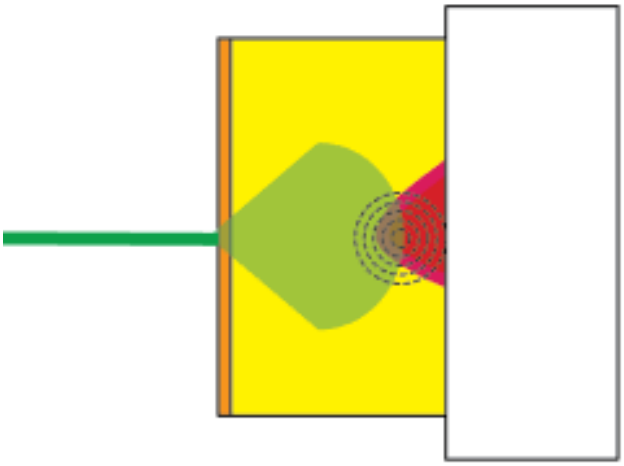

Figure 1.3: A diagram of PHIL traveling through skin and subcutaneous fat to treat a mass of scar tissue near a bone. When the laser beam enters the tissue, spreading of the light occurs. When the light is absorbed by the scar tissue a PAI pressure wave is generated.

One of the advantages of PHIL in treating arthrofibrosis is that the intensity of the resulting pressure wave is proportional to the optical absorption of the targeted tissue, which is wavelength dependent. By selecting an appropriate laser wavelength, it is possible to selectively target the scar tissue, while leaving most surrounding tissue unaffected. This selectivity helps to ensure that a minimal trauma and inflammation is caused. On the other hand, laser treatments have a disadvantage of limited penetration depths, usually less than 1cm. Additionally, the light for PHIL can be absorbed by the melanin in the skin, lowering the effectiveness of deeper areas and potentially damaging the skin.

1.4.3 Photo-mediated ultrasound therapy (PUT)

The third treatment method we are exploring utilizes synchronized applications of PHIL and PHIFU, which we call photo-mediated ultrasound therapy (PUT) as seen in Figure 1.4. While PHIL and PHIFU are combined the resulting pressure wave will be a combination of both sources. By carefully synchronizing the timing of the laser pulse and ultrasound burst, it is possible to overlap the negative phases of the pressure waves to create the largest possible rarefactional pressure.

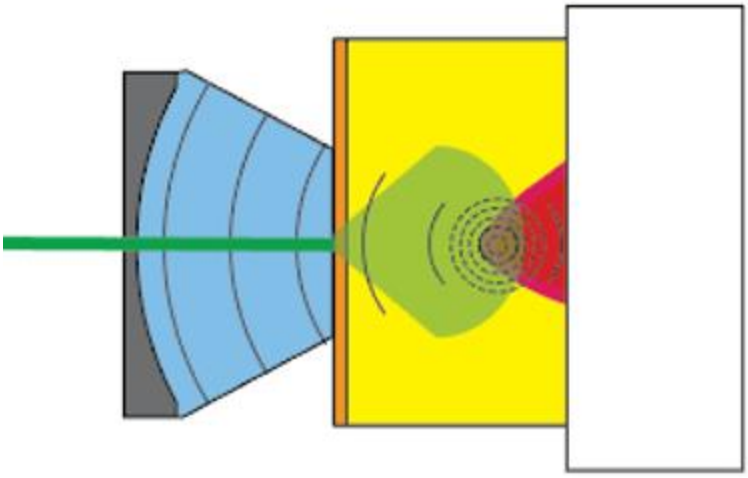

Figure 1.4: A diagram of PUT, which is a combination of PHIFU and PHIL. The laser beam used for PHIL is directed through a central hole in the ultrasound transducer used for PHIFU. The timing of both treatments is carefully adjusted to allow the pressure waves to interfere constructively.

The goal when using PUT is to lower the individual intensities of PHIFU and PHIL to just below the cavitation thresholds. In this way cavitation can only occur when both effects are present. This prevents unwanted targeting of tissues. For example, if the focal point of the ultrasound transducer is not located at an optically absorbent tissue there will be no contribution from PHIL and no cavitation will occur. Similarly, if there is optical absorption at the skin where the intensity of PHIFU is low, there will be no cavitation and the tissue will be preserved. Finally, by utilizing two methods of generating pressure waves the intensity of each individual method can be lower allowing for safer treatments.

1.5 Goals of the research

To test the proposed treatments for arthrofibrosis, an appropriate animal model must be developed. The focus is on joint contracture due to tightening of the posterior capsule of rabbit knees. This was because surgery could be performed on the posterior portion of the knee to produce consistent scarring. Additionally, arthrofibrosis of the posterior capsule has been found to cause significant

joint flexion, meaning that successful treatment will result in quantifiable increase in ROM. A method of reliably taking repeated ROM measurement will be developed to monitor changes throughout the course of treatments. The next focus will be treating the new animal model. A new system will be developed which can deliver PHIL, PHIFU, and PUT to the scarred posterior capsule. ROM measurements of the model leg will be compared to the contralateral control leg to determine when a full recovery has been achieved. Finally, the underlying mechanism of causing cavitation through PUT to optimize the treatment will be investigated while potentially illuminating alternative applications of the treatment.

The results of this research will be presented in the following fashion. Chapter 2 will present the animal model that was developed using a single surgery on rabbit knees. Chapter 3 will present the treatment system, experimentation, and the results of each treatment in the animal model. Chapter 4 investigates the use of PUT on tissue phantoms and presents the effects of changing various parameters. Chapter 5 will numerically solve equations related to PAI waves and bubble growth to examine the effects of different wavelengths and laser geometries. Finally, chapter 6 will discuss how all the results relate to each other and will lay out a path for future work.

Chapter 2 - A Novel Rabbit Model of Moderate Knee Contracture Induced by Direct Capsular Damage

2.1 Abstract

The treatment of joint contracture continues to represent a challenging problem in orthopedic surgery and rehabilitation medicine. Existing animal models of knee contracture for evaluating new treatments are mostly created by extensive joint tissue damage with Kirschner-wire immobilization which requires a second surgery to remove Kirschner-wires. This study aimed to develop a less invasive rabbit model of moderate knee contracture through a single surgery. Skeletally mature New Zealand White rabbits had their right knee operated to create surgical damage to the posterior capsule under direct visualization. Operated knees were then held in a flexed position by suturing the superficial flexion muscles with absorbable sutures. The flexion contracture (net extension loss) was determined by comparing the extension angles between the operated and non-operated knees from 8 to 24 weeks post-surgery. The flexion contracture of the operated knees was significantly greater ($p < 0.01/0.001$) than the non-operated knees at each weekly measurement. The mean flexion contractures were $22 \pm 6°$ at 8 weeks, $19 \pm 8°$ at 16 weeks and $18 \pm 8°$ at 24 weeks. No significant differences in the severity of flexion contracture were observed between 8-week and each of the following weeks, suggesting that the flexion contracture was essentially stabilized by 8 weeks post-surgery. Histopathologic analyses demonstrated intra-articular and peri-articular scar formation. This less invasive rabbit model of moderate knee contracture is more quickly established through a single surgery with lower risk of surgical complications compared to the previously reported invasive models, and could be an alternative animal model for joint contracture research.

2.2 Introduction

Joint contracture restricts the range of motion (ROM) of the affected joint, resulting in joint deformity, reduced motor skills, joint pain, and loss of function. Small impairments of ROM of the knee can cause gait disturbances and significantly increase the energy expenditure for daily activity. A knee flexion contracture of as little as 5° may result in a limp, and a permanent knee contracture of greater than 10° may require surgical interventions (Jerome G. Enad, 2014; J. R. M. Hutchinson, E. N. Parish, & M. J. Cross, 2005; Mitsuyasu et al., 2011b; Perry, 1987; Alfredo Schiavone Panni, Simone Cerciello, Michele Vasso, & Mario Tartarone, 2009; Schwarzkopf et al., 2013; Tardy et al., 2016; Wong et al., 2015).

Joint contractures can be a result of arthrofibrosis, shortening or stiffening of peri-articular tissues, or severe arthritis. Joint injury and surgery may cause arthrofibrosis due to excessive scar formation in and around the joint. Arthrofibrosis of the knee joint is a common complication following a knee surgery. One study found that 27.5% of all patients who were readmitted within 90 days of a total knee arthroplasty (TKA) were due to arthrofibrosis (Schairer, Vail, & Bozic, 2014). Another study examined the causes for TKA revisions and found that arthrofibrosis was a contributing factor in 34 out of 42 cases (Moya-Angeler et al., 2017). The presence of pre-operative flexion contracture was associated with an increased incidence of a persistent post-operative flexion deformity even if the contracture was corrected at surgery (Lam, Swift, & Shakespeare, 2003; Ritter et al., 2007). Once a joint contracture is established, natural recovery can be very slow or may never be complete in human patients. It can be very difficult to surgically remove intra-articular scar tissues without creating new scar tissues (Mitsuyasu et al., 2011a).

Appropriate animal models for joint contractures are important for development and evaluation of new treatments for the disease. Although joint contractures have been created in a

variety of species such as rat, rabbit, canine, and monkey (Akai, Shirasaki, & Tateishi, 1997; Akeson, Woo, Amiel, & Doty, 1977; Finsterbush & Friedman, 1973; Fukui, Fukuda, et al., 2001; Lavigne, 1972; Schollmeier, Sarkar, Fukuhara, & Uhthoff, 1996), the rabbit is the most widely used species. The advantage of rabbit models of joint contracture is that the hind legs of rabbits are much larger than those of rodents, allowing for a wider variety of treatments to be tested. On the other hand, rabbits are still small enough to house and handle easily. The knee and elbow are most commonly used joints for creation of joint contractures in animals as these joints are more prone to stiffness after joint injury or surgery (Morrey, Askew, & Chao, 1981; Perry, 1987).

Previous animal models of joint contractures applied immobilization with or without injury to produce loss of joint motion. The major drawback of immobilizing a normal joint for inducing joint contractures is that the contractures are reversible when the immobilization is discontinued (Akeson et al., 1977; Schollmeier et al., 1996). In an attempt to overcome this problem, Hildebrand et al.(Hildebrand, Sutherland, & Zhang, 2004) developed a rabbit knee model of joint contracture by combining arthrotomy, removal of cortical bone from the medial and lateral femoral condyles to mimic stable intra-articular fractures, and 8 weeks of immobilization using a Kirschner-wire (K-wire) in forced flexion at 150°. The average flexion contractures of the experimental knees in the 0-week and 8-week remobilization groups were 38° and 33°, respectively, which were significantly greater than the unoperated contralateral knees (8°). The average flexion contractures of the 16-week and 32-week remobilization groups were 19° and 18°, respectively, indicating a stabilization of the motion loss (Hildebrand et al., 2004).

Nesterenko et al.(Nesterenko et al., 2009) later modified the early models by creating cortical defects in the femoral condyles, transecting the anterior cruciate ligament (ACL) and posterior cruciate ligament (PCL), hyperextending the knee joint to -45° to indirectly disrupt the

posterior capsule, and immobilizing the knee at 160° flexion angle using a K-wire for 8 weeks (group I). Additional rabbits were operated on using an identical protocol except for the absence of capsular injury (group II). At immobilization release, the average contracture was 76° in group I versus 20° in group II. Sixteen weeks after remobilization, the mean contracture was 49° in group I versus 11° in group II ($p<0.001$), suggesting that injury to the posterior capsule results in a more severe knee contracture (Nesterenko et al., 2009). Nesterenko's model has been used in many recent studies on post-traumatic knee contracture.(Abdel et al., 2012; Barlow et al., 2013; Steplewski et al., 2016; Steplewski et al., 2017) Surgical complications of this model include post-operative bone fractures at the entry point of K-wires (highest incidence), failure of K-wire immobilization, self-mutilation of the operated limbs, and non-orthopedic medical problems. As a result of severe complications, 26% (18/70) to 27% (6/22) of the operated rabbits had to be eliminated from the studies during the 8-week immobilization (Nesterenko et al., 2009; Steplewski et al., 2017).

These previous studies have made substantial contributions to the development and improvement of animal models of joint contractures for evaluating the effectiveness of surgical release and pharmacologic therapy for arthrofibrosis. However, none of the reported models could mimic all clinical conditions of human patients with joint contractures. For example, many patients seeking non-invasive rehabilitation therapies have only mild to moderate joint contractures, which are not caused by extensive joint tissue damage with forced maximum flexion as described in the literature (Abdel et al., 2012; Barlow et al., 2013; Nesterenko et al., 2009; Steplewski et al., 2017). Therefore, it would be necessary to develop a moderate but stable joint contracture model induced by less invasive surgical procedures.

Based on the previous results showing that indirect injury to the posterior capsule results in a severe knee contracture, while forced maximum flexion only leads to a reversible knee contracture (Hildebrand et al., 2004; Nesterenko et al., 2009), we hypothesized that a stable rabbit knee contracture could be induced by direct damage to the posterior capsule with a non-rigid immobilization of the joint. The objective of this study was to develop a new rabbit model of moderate but stable knee contracture induced by direct damage to the posterior capsule with a muscle adhesion-based immobilization.

2.3 Materials and methods

2.3.1 Animals

Eight fresh carcasses of skeletally mature New Zealand White (NZW) rabbits, 4 males and 4 females, were obtained from the research animal facility at the University of Kansas Medical Center for normal structural analysis of rabbit knee joints after harvesting abdominal organs for other studies. Those healthy rabbits were originally purchased from the Charles River Laboratories (Leonard, MI).

Twenty-three skeletally mature NZW rabbits, either sex, weighing between 2.8 and 3.6 kg (Charles River), were used for the knee contracture model study. All animal procedures were performed with the approval of the Institutional Animal Care and Use Committee (IACUC) at the University of Kansas (Protocol No. 188-06) in compliance with all federal and state laws and regulations.

2.3.2 Structural and Functional Analysis of Normal Rabbit Knee Joints

In order to effectively develop a new rabbit model of knee contracture, we performed a detailed structural analysis of normal rabbit knee joints on 8 carcasses of skeletally mature NZW rabbits, with a focus on deep dissection of the posterior, medial, and lateral aspects of the knee joint. After euthanasia, rabbit legs were disarticulated at the hip level and skinned to better visualize the internal structure of the knee joint and its surrounding tissues. Tissues were dissected under a dissecting scope (3X) to clearly visualize small structures such as menisci and attachment sites of ligaments and tendons. Key local tissue structures relevant to the creation of knee contracture such as the femoral condyles and the popliteus tendon were photographed (**Figure 2.1**).

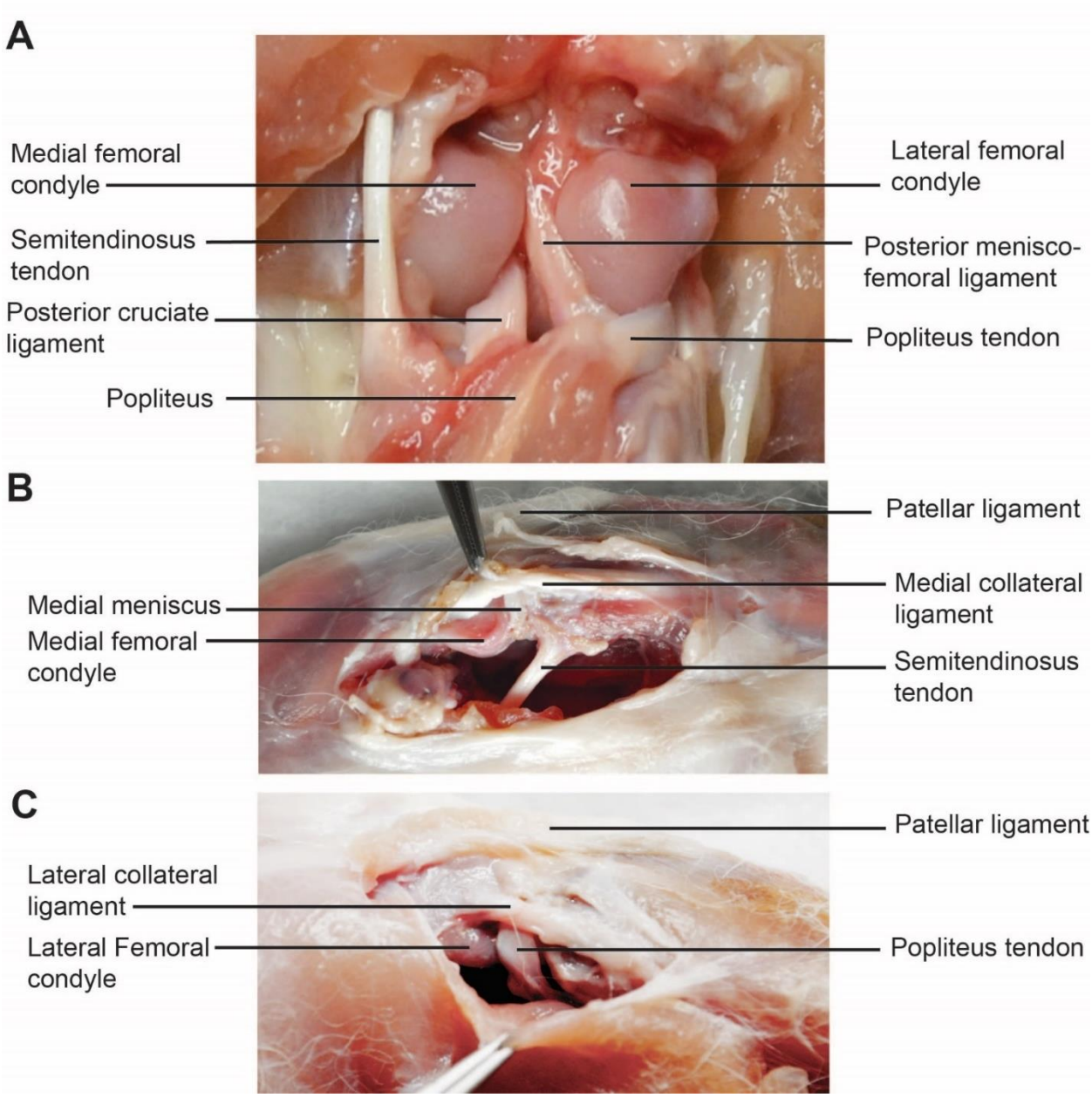

Figure 2.1: Representative photographs of rabbit knee structures relevant to surgical procedures for flexion contracture. (A) Deep tissue structures of the posterior aspect of a right knee. (B) Tissue structures of the medial aspect of a right knee, with the anterior side at the top of the image. (C) Tissue structures of the lateral aspect of a right knee, with the anterior side at the top of the image.

Compared to the relative size of structural tissues seen in human knee joints, most ligaments and tendons adhering to the posterior, medial, and lateral aspects of the synovium and capsule were much wider and thicker in rabbits relative to the size of the femoral condyles and

tibial plateau (**Figure 2.1A-C**). The posteromedial surface of the medial meniscus and the attachment of semitendinosus tendon could be clearly visualized via a medial approach (**Figure 2.1B**), while the oblique popliteal ligament derived from the semi-membranosus seen in human knee joints was not remarkable in rabbits. The posterolateral surface of the popliteus tendon and the upper portion of the popliteus could be visualized via a lateral approach (**Figure 2.1C**). The muscular masses of biceps femoris and gastrocnemius in rabbits were substantially larger relative to the size of the femur and tibia (**Figure 2.2A**).

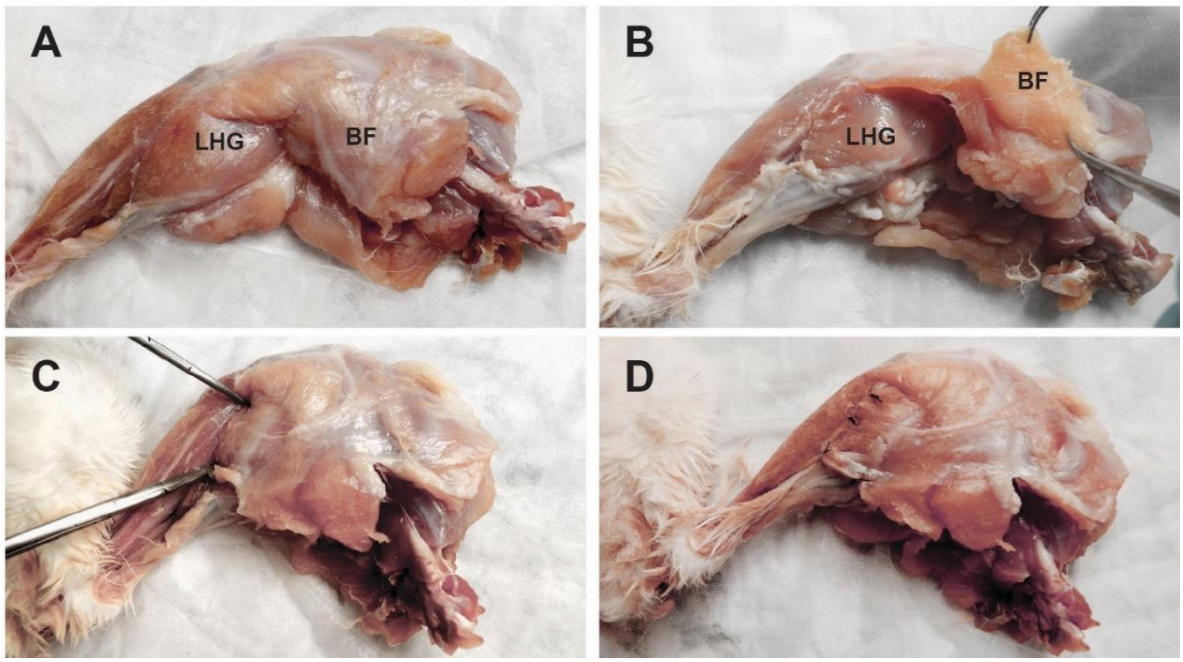

Figure 2.2: Photographs representing the steps of a muscle-flap based immobilization of the rabbit knee. (A) Flexion muscles of a rabbit knee. LHG: lateral head of gastrocnemius; BF: biceps femoris. (B) A muscle-flap created from the biceps femoris. (C) A muscle-flap derived from the biceps femoris being pulled towards the upper tibia overlapping with the LHG. (D) A muscle-flap has been sutured with the LHG to immobilize the knee in a flexed position.

A muscle flap of the biceps femoris could be dissected out through a fascial gap, pulled towards the lateral side of upper tibia, and sutured together with the lateral head of gastrocnemius, thereby holding the knee joint at a flexed position. The degree of flexion positions could be

adjusted by changing the area of overlap between the muscle flap and the surface of the lateral head of gastrocnemius (**Figure 2.2B-D**). These structural and functional analyses of rabbit knee joints greatly helped us design and perform new surgical procedures for knee joint contracture in rabbits.

2.3.3 Surgical Procedures

The surgery was performed on the right knee joint under sterile conditions and general anesthesia. The experimental rabbits underwent inhalation general anesthesia with isoflurane after being sedated with intramuscular injection of ketamine (40 mg/kg) and xylazine (5 mg/kg). The animal was placed in the supine position. The surgical area was shaved, prepped and draped in the sterile fashion. Two 3.5-4 cm long skin incisions were made over the lateral collateral ligament (LCL) and the medial collateral ligament (MCL), respectively. After exposing the posterior capsule on both sides, the adhesion of the posterior capsule to the surrounding tissues was bluntly separated. The lateral 1/3 (posterior to LCL) and the medial 1/3 (posterior to MCL) of the posterior synovium/capsule were transversely incised superficially and then completely disrupted by forceps. The middle 1/3 was partially damaged by forceps without disrupting it. The location of capsular damage is illustrated in **Figure 2.3**. In order to increase rough surfaces for scar formation in the posterior areas of the knee, the posterior surfaces of the medial meniscus was transversely disrupted with a No. 11 surgical blade. Bleeding from the dissected tissues was stopped by manual pressure with a piece of surgical gauze. The ruptured capsule and synovial membrane were left open.

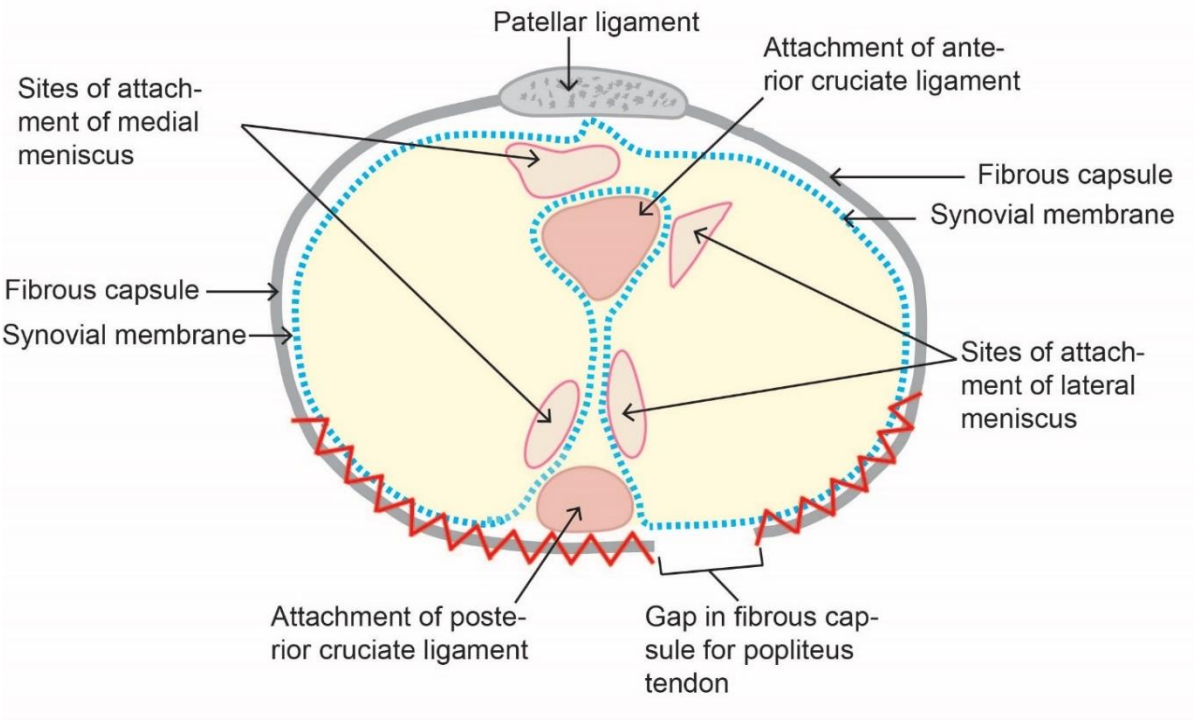

Figure 2.3: An illustrative diagram showing a cross-sectional view of a knee joint. The saw-tooth lines indicate the locations of disrupted posterior capsule and synovial membrane.

In order to facilitate the scar formation in the posterior areas of the knee, a muscle flap was dissected out from the distal portion of biceps femoris, pulled towards the lateral side of upper tibia, and sutured with the superficial layer of the lateral head of gastrocnemius to hold the knee in a flexion position of approximately 60°. This procedure prevented the knee joint from extension (see Figure 2C-D). The flexed immobilization was further enhanced by pulling the superficial layer of the medial flexors together with absorbable sutures (4-0 Vicryl, Ethicon). The deep fascia was closed with absorbable sutures (4-0 Vicryl, Ethicon). The skin incisions were then closed with 4-0 non-absorbable sutures.

A clear plastic E-collar (3M, Maplewood, MN) was placed on each rabbit immediately following surgery to prevent the removal of the sutures and self-mutilation by the operated animals. Following surgery, the rabbits were allowed free cage activity, monitored for

complications, and assessed for pain or stress. The assessments were performed daily for the first week, and three times per week for the rest of the recovery period. Meloxicam (0.2 mg/kg) was injected subcutaneously as needed based on pain assessment as described in **Appendix 1**. The operated rabbits were allowed to recover for 8 weeks after the surgery before their knee contractures were assessed. During this period, the rabbit limbs were only manipulated to examine the incisions, blood circulation and skin sensation. The non-absorbable sutures for skin incisions were removed 10 days post-surgery. The E-collar was removed 12 days post-surgery. The absorbable sutures were absorbed and gradually released the muscle flap held for temporary immobilization, allowing for remobilization of the operated knees without a second surgery.

2.3.4 Joint Angle Measurements

Starting eight weeks after the surgery, weekly measurements were performed to determine the severity of knee contracture. The rabbit was first wrapped in a towel and gently held laying on its side. The leg was exposed and the thigh was held against the body in a manner similar to a natural crouched position. The angle between the longitudinal axis of the femur and tibia were measured, with the center of the patella placed at the vertex of the angle. A strap was placed around the leg with the center 10 cm from the knee. A force of 2 N was applied perpendicularly to the leg in order to extend the knee joint. The force was verified by a spring force gauge. The resulting torque of 0.2 Nm was the same as used in previous studies.(Barlow et al., 2013; Nesterenko et al., 2009) Care was taken to ensure that the rabbit was not resisting or forcing the leg during the measurement. The flexion contracture of each leg was determined to be the angle of maximum extension from the 0.2 Nm torque. Net flexion contracture was calculated by taking the difference in maximum extension between the operated knee and contralateral control knee. Five repeated measurements over the course of a single day resulted in a measurement error of ±3°.

2.3.5 Histology and Histochemistry

At the designated endpoints, both the operated and non-operated knee joints were harvested after euthanasia of the animals. The tissue samples were fixed in 10% buffered formalin (American MasterTech, Lodi, CA), decalcified in 25% formic acid (Sigma, St. Louis, MO), and embedded in paraffin (Leica Biosystems, Richmond, IL), sectioned at 5 μm, and stained with hematoxylin and eosin (H&E) to observe the general tissue structures, while safranin O and fast green were used to identify cartilage cells and matrices as previously described (Rodova et al., 2011; J. Wang, 2000; J. Wang et al., 2009; Xu, Anderson, Lu, & Wang, 2007). The embedded knee joint samples were sectioned in either cross or sagittal orientation to identify the spatial relationship between the joint structure and scar tissues.

2.3.6 Statistical Analysis

The joint extension angles in the post-operative knees were compared to the non-operated knees. The sample size was calculated assuming a 5% type 1 error and 80% power to detect the difference between the groups. A power analysis (based on our preliminary data) suggested that 5 rabbits for each test group were sufficient to detect statistically significant differences between the experimental and control groups. Results are presented as a mean value ± standard deviation (SD). The joint angle measurements from the operated knee and contralateral non-operated knee were compared by a Student's t-test. One-way analysis of variance (ANOVA: Repeated Measures) was used to determine statistical differences between the weekly net flexion contracture measurements. A p value of < 0.05 was considered statistically significant.

2.4 Results

2.4.1 Surgical Complications

Twenty-one of the 23 operated rabbits reached the designated endpoints, while 2 rabbits had to be eliminated from the study due to self-mutilation of their feet in the 3rd week after the surgery. Physical examination of those rabbits indicated that their skin sensation was reduced due to an assumed nerve injury. This complication occurred in the early cases of the study. Additional cautions were taken for the later cases during the dissection of the posterior capsule and the muscle flap for immobilization, which effectively prevented nerve injuries and self-mutilations. No other surgical complications such as infection and bone fracture were observed during the 24-week period of experiments.

2.4.2 Measurements of Flexion Contracture

During the 8 weeks recovery period the gait of operated rabbits was closely observed, but actual joint angle measurements were not conducted. The rabbits were accommodated to being held in the same fashion that would be used for knee measurements after 8 weeks. Immediately after surgery the rabbits did not put weight on the operated leg; however, after several days all of the rabbits began to use both legs with a slightly altered gait. The gait was noted to be modified on the operated leg with the knee more flexed and the ankle more extended to compensate for weight-bearing. The results of the maximum extension measurements are shown in **Figure 2.4b.**

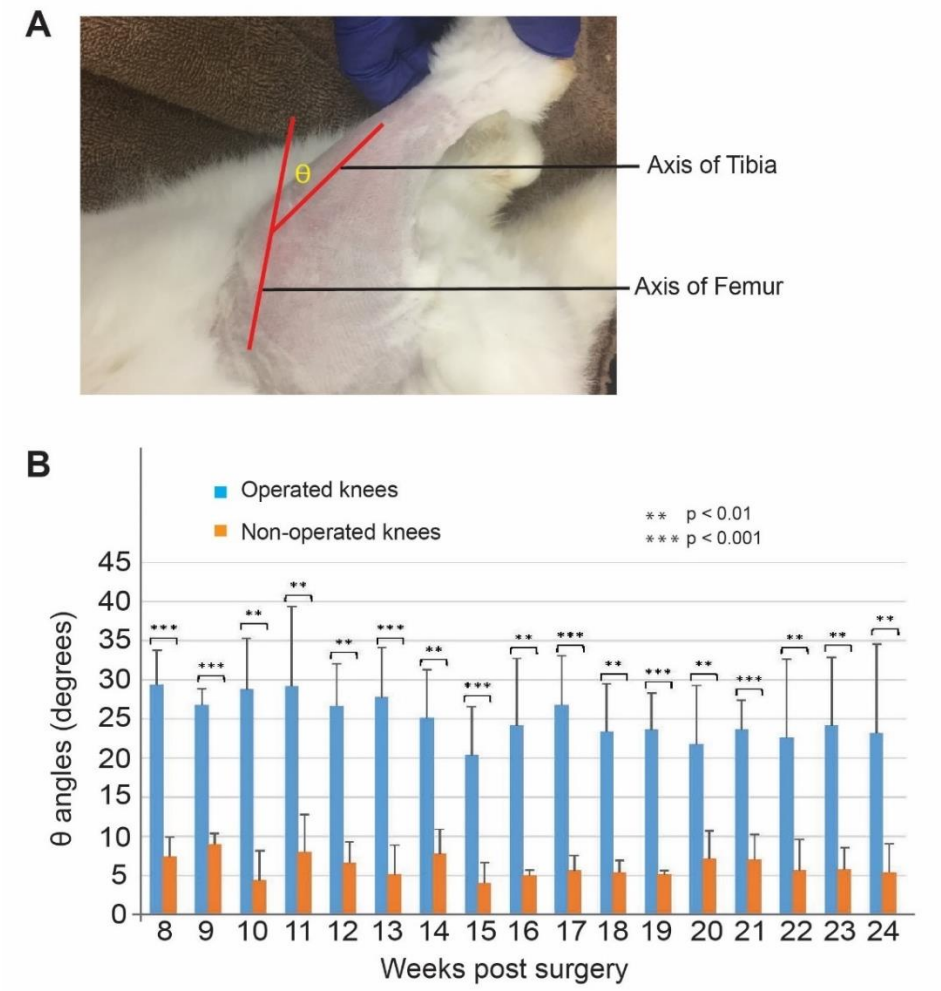

Figure 2.4: Temporal changes in flexion contracture from 8 to 24 weeks post-surgery. (A) The extension angle (θ angle) is determined by measuring the angle between the longitudinal axes of the femur and of the tibia. (B) The differences in maximum extension between the operated and non-operated knees are statistically significant at each weekly measurement from 8 to 24 weeks post-surgery.

At 8 weeks, measurements were taken on 21 rabbits. After the initial measurements, 16 of the 21 rabbits were randomly selected for treatment studies and excluded from the later analyses of this study, but will be reported in a separate communication. One rabbit from each of 5 surgical dates were randomly selected for evaluating the effectiveness of model development without treatment. The staggered surgical dates (spread over 5 months with 1 surgical day per month) were chosen to help prevent seasonal variation or other stressors from impacting the overall results. A

power analysis based on the degree of flexion contracture (mean ± SD) indicated that 5 rabbits could provide 80% power to detect significant group differences between the operated and non-operated knees (controls). A Student's t-Test found no significant difference in flexion contracture between the group of 5 and the group of 16 rabbits at 8 weeks post-surgery. The maximum extension angles of the 5 non-treatment rabbits were then taken weekly from 8 to 24 weeks.

The flexion contracture of the operated knees was significantly greater than the non-operated knees at each weekly measurement (**Figure 2.4B**). The flexion contracture was 22 ± 6° at 8 weeks for the group of 21 rabbits, and was 19 ± 8° at 16 weeks and 18 ± 8° at 24 weeks for the remaining 5 rabbits. The contracture produced in this model appeared to be less severe than that of the previously reported invasive rabbit model of knee contracture at the same post-operative time points (Nesterenko et al., 2009; Steplewski et al., 2017). The results of all weekly net flexion contracture measurements were compared with the measurement at 8 weeks through one-way ANOVA post hoc analyses. This weekly comparison demonstrated no statistically significant differences between 8-week and each of the following weeks, suggesting that the flexion contracture has essentially stabilized by 8 weeks post-surgery (**Table 2.1**).

Table 2.1: Weekly averages of net flexion contracture defined as the difference in maximum extension between the operated knee and the contralateral control knee.

Table 2.1 Weekly Net Flexion Contracture Measurements

Weeks Post Surg.	No. of Rabbits	Net Contracture (mean ± sdv)	p value (vs 8weeks)
8	25	22.0 ± 5.7	---
9	5	17.8 ± 2.6	0.188
10	5	24.4 ± 6.7	0.558
11	5	21.2 ± 6.2	0.837
12	5	20.0 ± 7.1	0.636
13	5	22.6 ± 4.3	0.856
14	5	17.4 ± 5.3	0.222
15	5	16.4 ± 4.2	0.117
16	5	19.2 ± 8.1	0.547
17	5	21.2 ± 4.8	0.817
18	5	18.0 ± 6.3	0.323
19	5	18.4 ± 4.7	0.308
20	5	14.6 ± 5.7	0.074
21	5	16.6 ± 2.3	0.104
22	5	17.0 ± 7.7	0.28
23	5	18.4 ± 7.8	0.43
24	5	17.8 ± 8.0	0.372

2.4.3 Histological Analysis

All experimental rabbits were euthanized for histological analyses of the knee joints at 24 weeks post-surgery. The tissue sections were microscopically examined through both conventional and polarizing lenses. Scar tissues were observed in both intra-articular spaces and peri-articular areas, particularly in the posterior region, of the operated knee joints. The histological characteristics of normal knee joint structure and the histopathological features of intra-articular scar tissues in the posterior region of the operated knees are presented in **Figure 2.5**. In the non-operated knees,

normal joint capsules displayed well organized fibrous structure with intact synovium and synovial cavity (**Figure 2.5, upper panels**). In the operated knees, the areas with disrupted posterior capsule and its attachments displayed disorganized dense scar tissues in the peripheral area of joint cavity, with little evidence of scar resorption (**Figure 2.5**, **lower panels**). The histological characteristics of normal peri-articular tissues and the features of peri-articular scar formation in the posterior region of the operated knees are presented in **Figure 2.6**. Dense scar tissues with disorganized collagen orientations were adhered to the posterior margins of the operated knee joint (**Figure 2.6, lower panels**).

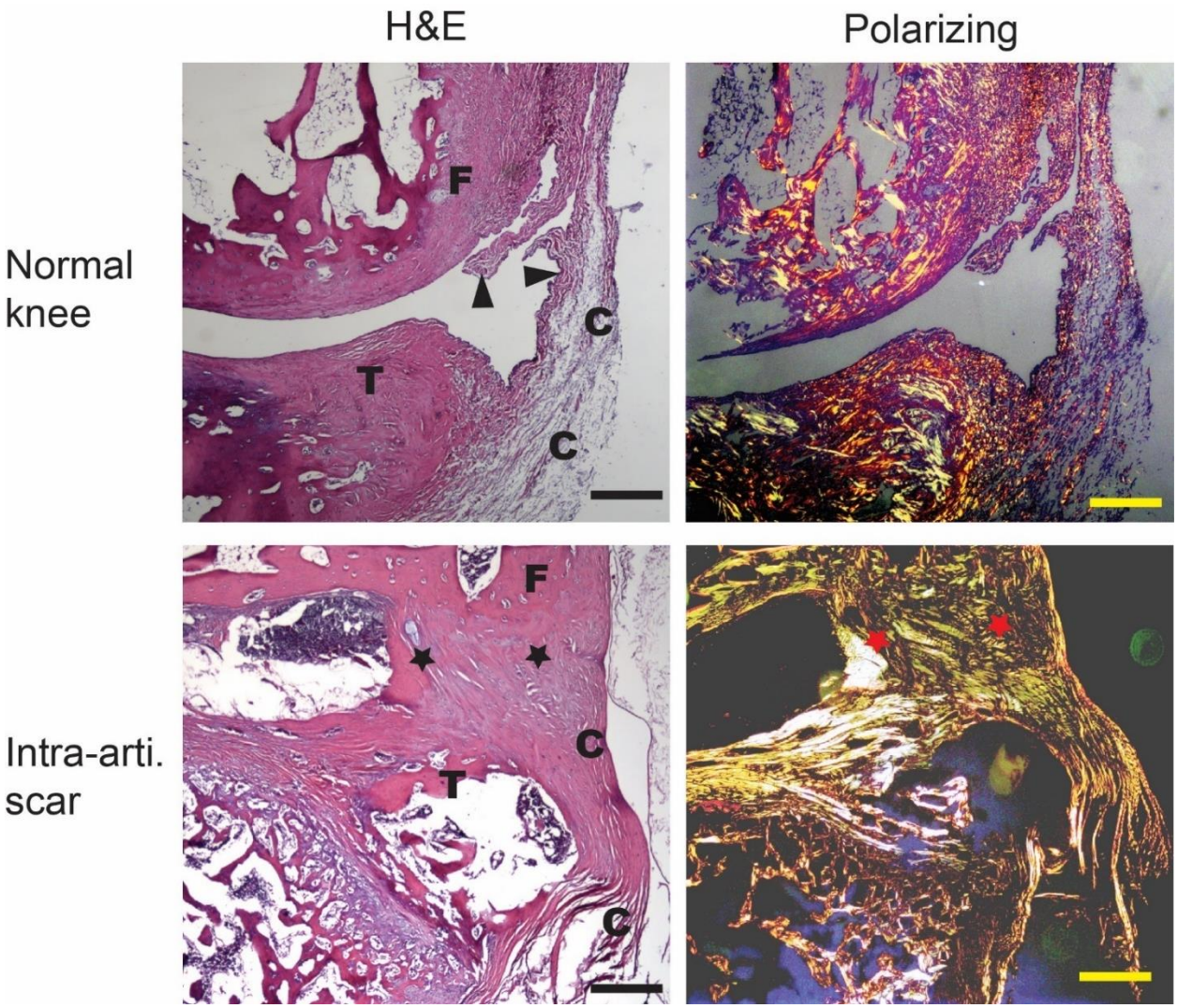

Figure 2.5: Intra-articular (Intra-arti) scar formation at 24 weeks post-surgery. The tissue sections were microscopically examined through both conventional (H&E) and polarizing lenses. Upper panels: A normal joint capsule (C) in a non-operated knee shows a well-organized fibrous structure with intact synovium (arrowheads) and synovial cavity. Lower panels: In an operated knee, the area with disrupted posterior capsule (C) display disorganized dense scar tissues (stars) in the peripheral area of joint cavity. F = femur; T = tibia. H&E staining, scale bar = 200 µm.

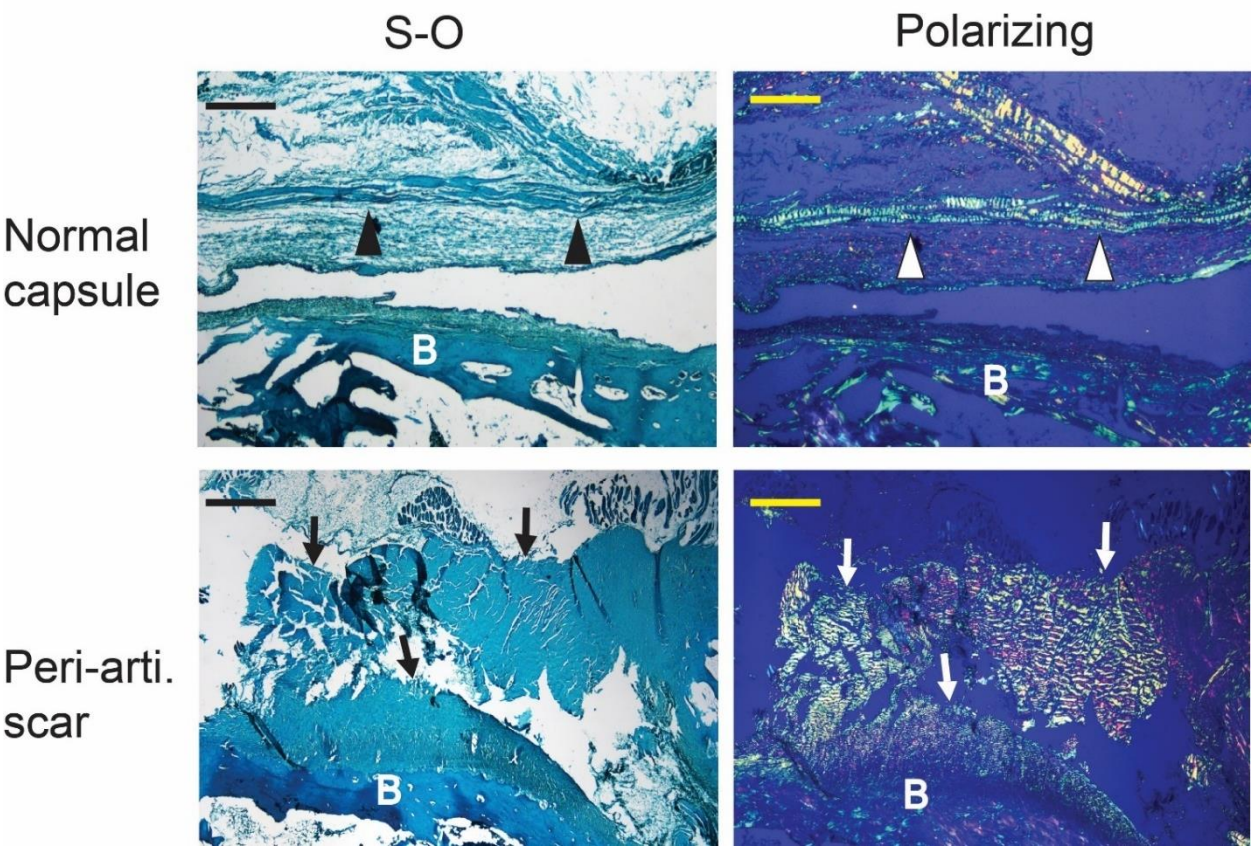

Figure 2.6: Peri-articular scar formation at 24 weeks post-surgery. Upper panels: A normal joint capsule (arrowheads) of non-operated rabbit knee shows a well-organized fibrous structure (arrowheads). Lower panels: Peri-articular (Peri-arti) scar tissues (arrows) are observed in the posterior region of an operated knee joint. Dense scar tissues with disorganized collagen orientations were adhered to the posterior bone margins (B) of the knee joint. Safranin-O (S-O) and fast green staining, scale bar = 200 µm.

2.5 Discussion

The rabbit model of knee contracture developed in the present study is a novel joint contracture model with a moderate but statistically significant extension loss compared to the contralateral intact knee joint. This animal model was successful in its specific goal to provide an alternative model of moderate knee contracture for testing the effectiveness of various rehabilitation therapies. Although the knee contracture created in this study is less severe than that achieved in other more invasive models, it falls within the range of flexion contractures of the knee seen in human patients

following TKA (0-30°) (Hartman et al., 2010; Moya-Angeler et al., 2017) and patients with knee contractures after ACL reconstruction (10-20°) (Tardy et al., 2016; Wierer, Runer, Gfoller, Fink, & Hoser, 2017). Furthermore, the angle of muscle-flap associated knee immobilization is adjustable as desired (Figure 2). The major advantages and potential limitations of this model are discussed below.

This rabbit knee contracture model is induced by direct damage to the posterior capsule (defined as "direct capsular damage model of knee contracture") with much less tissue damage, compared to the previously reported rabbit knee contracture models (Hildebrand et al., 2004; Nesterenko et al., 2009). The present knee contracture model focuses on direct damage to the posterior capsule with a non-rigid immobilization. It does not create bone defects in femoral condyles, does not transect the ACL and PCL, does not apply hyperextension of the knee joint to -45°, and does not use a K-wire for immobilization. The surgical time for this model is one third of the more invasive models reported previously (Hildebrand et al., 2004; Nesterenko et al., 2009) when performed by the same surgical team, which was confirmed by our preliminary studies on rabbit carcasses. Additionally, the operated knee joint is stable after the surgery with less risk for development of posttraumatic osteoarthritis, compared to the knee contracture models with ACL and PCL transections.

As a result of the less invasive procedure, the incidence of surgical complications is much lower (8%) in this model versus 26-27% in the more invasive models with post-operative bone fracture as the most notable complication due to possible mechanical stresses from the K-wire immobilization (Nesterenko et al., 2009; Steplewski et al., 2017). In contrast, no single bone fracture was observed in this study. Self-mutilation (toe chewing) was observed in two rabbits in the early cases of this study, possibly due to nerve injuries. It has been previously reported that

following hind leg intramuscular injections of ketamine, xylazine and acepromazine, 4 of 6 rabbits exhibited self-mutilation of the digits due to sciatic nerve injury (Vachon, 1999). However, our injections of ketamine and xylazine were given in the lumbar muscles to prevent such nerve injuries. In addition, the complication of self-mutilation was successfully prevented in the later cases by more careful dissection around the joint capsule and suturing of the muscle flaps, suggesting that the nerve injury was likely due to the surgical procedure.

The time required to reach a stabilization of flexion contracture (extension loss) in this model is substantially shorter than the previously reported models (Hildebrand et al., 2004; Nesterenko et al., 2009). The present study has established knee contractures by one surgery, and the operated knee joints reached a stable phase of flexion contracture that is significantly different from the contralateral control knees at the end of 8 weeks after the surgery. Although seasonal variation seemed to be a concern while looking at the temporal changes in flexion contracture, our weekly measurements found no statistically significant differences in the severity of flexion contracture between 8 weeks and each of the following weeks. In contrast, the previously reported rabbit knee contractures were produced by two-step surgical procedures (Hildebrand et al., 2004; Nesterenko et al., 2009). The first step was to create joint tissue damage and immobilize the knee by a K-wire; the second step was to surgically remove the K-wire and to start a remobilization 8 weeks after the initial surgery. The flexion contracture of the operated knee joints reached a stable phase at the end of 16 weeks after the remobilization (24 weeks after the initial surgery). The shorter recovery time developed in this study significantly reduces the duration and costs for the development of animal models of joint contracture. Additionally, allowing the rabbits to freely use the operated leg may minimize the muscle atrophy caused by rigid immobilization using a K-wire or a cast.

Direct damage to the posterior capsule is created under direct visualization in this new model. Therefore, the location of post-operative scar formation could be predicted, which helps select appropriate therapeutic modalities. This is in contrast to the indirect capsule damage model produced by a manual hyperextension of the knee to -45°, which may damage not only the capsule but also other joint tissues such as ligaments, muscles, nerves, and blood vessels, and would be difficult to predict the location of scar tissues.

One of the limitations of this model is that the operated knee joint is immobilized by a non-rigid method (suturing overlapped muscle flaps) rather than a rigid immobilization by a K-wire or cast. The rabbits are allowed to use the surgically altered leg with different activities and mechanical forces. This may result in a relatively large variation in flexion contracture among the operated animals. Another limitation would be that the mechanistic study of this project is focused on the structural and functional analyses of the knee joint to establish the rationale for development of this new model, while detailed molecular and cellular mechanisms for scar formation are not included in this project. Additional mechanistic studies will be conducted in the future.

In conclusion, the present study has established a novel rabbit model of knee contracture by direct damage to the posterior capsule and muscle-flap based immobilization, resulting in a moderate but statistically significant extension loss compared to the contralateral control knee. Both intra-articular and peri-articular scar tissues are created in this model. The study succeeds in the goal of creating a rabbit model of moderate knee contracture (~20°) that is stable after eight weeks of recovery from the initial surgery. The severity of the knee contracture in this model is similar to that of the contractures seen in human patients following TKA and ACL reconstruction. This model can therefore be used as an additional option in the area of joint contracture research.

Acknowledgments

This work was supported by a medical research grant from the United States Department of Defense (DoD) under Award Number W81XWH-15-1-0524 and the Mary A. & Paul R. Harrington Distinguished Professorship Endowment. The authors thank Dr. Da Zhang (Professor of Pathology at the University of Kansas Medical Center) for his histopathological analysis of rabbit knee joints.

Chapter 3 - Treatment of post-traumatic joint contracture in a rabbit model using pulsed, high intensity laser and ultrasound

3.1 Abstract

Post-traumatic joint contracture induced by scar tissues following a surgery or injury can leave patients in a permanent state of pain and disability, which is difficult to resolve by current treatments. This randomized controlled trial examines the therapeutic effect of pulsed high-intensity laser (PHIL) and pulsed high-intensity focused ultrasound (PHIFU) for post-traumatic joint contracture due to arthrofibrosis. The peak power levels of both PHIL and PHIFU are much higher than that of laser or ultrasound currently used in physical therapy, while short pulses are utilized to prevent damage. To test the effectiveness of these treatments, a rabbit knee model for joint contracture was established. Twenty-one rabbits were split into four groups: untreated control (n=5), PHIL (n = 5), PHIFU (n = 5), and a PHIL + PHIFU group (n = 6). Maximum extension of the surgically modified rabbit knee was compared to that of the contralateral control knee over the course of 16 weeks. The rabbits in the untreated control group maintained a relatively consistent level of joint contracture, while every rabbit in each of the treatment groups had improved range of motion, eventually leading to a restoration of normal joint extension. Average recovery time was 7.6 ± 1.5 weeks for the PHIL treatment group, 9.8 ± 3.7 weeks for the PHIFU group, and 8.0 ± 2.2 weeks for the combined treatment group. Histopathology demonstrated reduced density and accelerated resorption of scar tissues in the treated knee joints. This study provides evidence that both PHIL and PHIFU are effective in treating post-traumatic joint contracture in rabbits and warrant further investigation into the underlying mechanisms to optimize PHIL and PHIFU based treatments in a larger number of animals.

3.2 Introduction

Patients who can no longer fully extend a joint after it has been injured are considered to have post–traumatic joint contracture, a condition which results in pain, stiffness, and disability for the patient. Post-traumatic joint contracture is often caused by arthrofibrosis, which is defined as a buildup of fibrous scar tissues in the joint, causing a painful reduction in range of motion (ROM) (Petsche & Hutchinson, 1999; Shelbourne & Patel, 1999). Post-traumatic contracture can result from either an initial injury to the joint or as a complication from surgery on the joint, such as anterior cruciate ligament (ACL) reconstruction or total knee arthroscopy (TKA) (Cosgarea et al., 1994). Currently when patients have joint contracture due to arthrofibrosis they will receive either conservative treatment or in more severe cases, surgery to release the contracture, however a complete recovery is not always attained (Cosgarea et al., 1994; J. G. Enad, 2014; J. R. Hutchinson et al., 2005; Kucera, Urban, Karpas, & Sponer, 2007; A. Schiavone Panni et al., 2009; Schwarzkopf et al., 2013).

Conservative treatment usually includes anti-inflammatory medication, stretching, joint mobilization, strengthening exercises, or therapeutic modalities (i.e. ultrasound or laser) to increase the limited ROM in the joint (Shelbourne & Patel, 1999). To achieve meaningful results, the conservative treatment often requires the aggressive use of physiotherapy (Cheuy et al., 2017). Extensive physical therapy can be very uncomfortable and painful for the patient, which can reduce patient compliance to maintain their exercise and treatment plan.

Patients with more severe joint contracture, or who have been unsuccessful with conservative treatments are referred to surgical intervention. While surgery can be successful for some patients, others may never fully recover normal ROM (Kucera et al., 2007). In some cases the surgery

itself may produce scar tissue in and around the joint, resulting in increased joint contracture (Mitsuyasu et al., 2011b).

We have developed a combined laser and ultrasound treatment system to reduce post-traumatic joint contracture due to arthrofibrosis. Our treatment system utilizes pulsed high-intensity laser (PHIL) and pulsed high-intensity focused ultrasound (PHIFU). PHIL and PHIFU can be used independently or can be applied synchronously.

PHIL differs from traditional laser therapies by using high intensity pulses with durations of only a few nanoseconds. For example, the peak intensity of PHIL used in the current study is greater than 10 MW/cm^2; the pulse duration is, however, only 5 ns. These very short pulses cause the photomechanical effect in optically absorbent tissues (McDonald & Wetsel, 1978), such as fresh scar tissue containing high concentrations of hemoglobin. The photomechanical effect creates a stress wave induced by the thermal expansion and contraction after the rapid heating and cooling caused by the short laser pulse. The short pulse duration also prevents the burns and thermal ablation seen in laser resurfacing treatments (Tanzi & Alster, 2002). Laser light has been shown to stimulate cells to promote healing responses through low-level laser therapy (LLLT) (Karu, 1987; Medrado, Pugliese, Reis, & Andrade, 2003). The higher intensity utilized in PHIL is intended to promote healing in deeper tissues than those targeted in LLLT (Karabut, Gladkova, & Feldchtein, 2016).

Ultrasound has been used to some success in the treatment of post-traumatic joint contracture and musculoskeletal disorders (Loyola-Sanchez et al., 2012; Naito et al., 2010; Tsumaki, Kakiuchi, Sasaki, Ochi, & Yoshikawa, 2004; Usuba, Miyanaga, Miyakawa, Maeshima, & Shirasaki, 2006), however the studies investigating its effectiveness mainly utilized low-intensity ultrasound (LIUS) and produced inconsistent results (van der Windt et al., 1999). The applications of high intensity

focused ultrasound (HIFU) are not as common in the treatment of musculoskeletal disorders. A limited number of studies showed that HIFU could reduce musculoskeletal pain (Brown, Farquhar-Smith, Williams, ter Haar, & deSouza, 2015; Masciocchi et al., 2014).

PHIFU has been used to disrupt the dense fibrous tissue in porcine tendons and ligaments of the ankle (Kuo, 2010). Further investigation showed that the tissue was mechanically disrupted, and the young's modulus of the tissue was reduced (Yeh, Li, Shih, Huang, & Kuo, 2013b). Both studies were performed *ex vivo.* The effectiveness of PHIFU on loosening fibrous tissue or relieving joint contracture has not been studied *in vivo*.

When pulsed laser and ultrasound are combined they cause synergistic increase in cavitation (H. Z. Cui, T. Zhang, & X. M. Yang, 2013). This phenomenon has been utilized in photo-mediated ultrasound therapy (PUT) to selectively target microvasculature (Hu et al., 2017). In a similar fashion, in this study we applied both PHIL and PHIFU at the same time to selectively cause cavitation in the scar tissue. The cavitation was intended to provide an additional method of disrupting the collagen fibers of the scar tissue. To treat the dense tissues within the knee higher intensities of both laser and ultrasound were used in this study compared to those used to target microvessels. The treatment probe was constantly scanned over the treatment area to avoid severe cavitation damage to a particular location.

We studied the effect of ultrasound on relieving joint contracture on a rabbit post-traumatic joint contracture model. Our ultrasound system utilizes high intensity focused ultrasound (HIFU), as opposed the unfocused lower intensity ultrasound that has been utilized. The peak intensity of PHIFU burst employed in the current study is more than 2000 W/cm^2. HIFU creates strong ultrasound intensity at the focal point of a HIFU transducer, while having a weaker intensity near the surface of the tissue. As a result, high dosage of ultrasound energy can be delivered to the

focal point, while damage to the surrounding tissues can be avoided. A small duty cycle of 1.5% was used to prevent excessive heating.

Focused ultrasound has been shown to be effective in the treatment of neural tissues in the brain. Higher intensities of ultrasound have been used for direct ablation of neural tissues (Hynynen et al., 2006), while lower intensities have been used for non-ablative stimulation (Lewis, Thomson, Rosenfeld, & Fitzgerald, 2016; Tufail, Yoshihiro, Pati, Li, & Tyler, 2011). Tyler (Tyler, 2011) proposed that non-ablative stimulation can effectively stimulate the conduction of neurons by increasing membrane permeability through mechanical effects. While the peak intensities of PHIL and PHIFU are comparable to ablative therapies, the short pulses are expected to prevent thermal ablation while causing mechanical effects commonly seen in non-ablative stimulation. The mechanical effects created by PHIL and PHIFU are expected to cause stimulation of the nerves in the targeted joint, leading to increased muscle activity.

The current study investigated the independent effect of PHIL and PHIFU, as well as the effect when both techniques are combined. The purpose of both techniques is to create mechanical effects from laser or ultrasound stimulation while avoiding ablation and thermal effects. The peak power levels used in the current study were much stronger than the laser and ultrasound levels traditionally used in physical therapy for musculoskeletal disorders. The short pulses and low duty cycles in the proposed therapies are intended to counteract the increased peak intensity, allowing these high intensity therapies to be used outside of surgical applications. Therefore, the current treatment scheme may open up a new avenue on how to use laser and ultrasound in relieving joint contractures.

3.3 Methods and materials

3.3.1 System

The treatment system (figure 3.1(a)) involved a 532 nm laser (Surelight SLI-30, Continuum, Santa Clara, CA)) system delivering light through an optic fiber to the treatment probe. The laser additionally triggered a function generator (33250A, Agilent Technologies, Santa Clara, CA.) The function generator was connected to a 50 dB power amplifier (350L RF Power Amplifier, ENI Technology Inc., Rochester, NY) which was then connected to a spherically focused HIFU transducer (H102, Sonic Concepts, Bothell, WA) through a 50-ohm impedance matching circuit.

The treatment probe (Figures 3.1(b) and 3.1(d)) aligned the 1-MHz transducer with the optical fiber through a central hole in the transducer. The fiber and the transducer were incased in a custom 3D printed cone to help focus the ultrasound waves and hold degassed and deionized water. Water was used for ultrasound transmission. Alignment of the laser fiber was maintained through the use of an additional 3D printed component that attached to the focusing cone. Finally a clear plastic membrane covered the distal end of the cone to prevent water leakage while allowing the laser and ultrasound to transmit effectively.

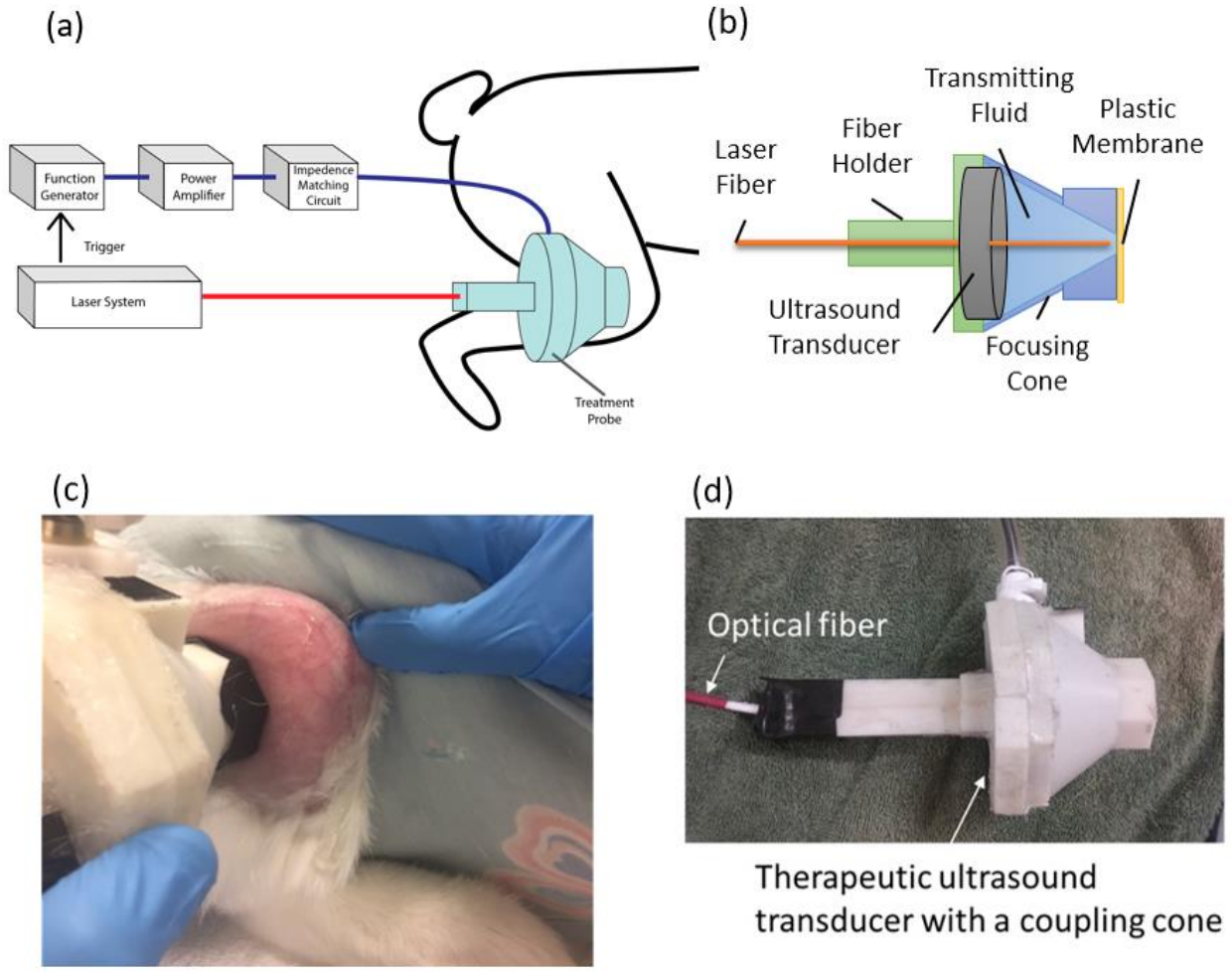

Figure 3.1. (a) A diagram of the treatment system. (b) A schematic of the treatment probe. (c) A photagraph of treatment probe during use. (d) A photograph of the actual treatment probe.

The ultrasound transducer was used to deliver 1000 cycles of 1-MHz ultrasound when triggered by the laser, creating a 1-ms burst. The 532 nm laser pulse had a 30-Hz repetition rate and a 5-ns pulse duration. The use of the optical fiber limited the maximum laser surface fluence that could be delivered to 52 mJ/cm^2 in our system. Due to the differences in travel speed, the ultrasound burst must begin before the laser pulse in order for both to arrive at the same time. When the laser triggered the function generator a 33.0-ms delay was added so that the ultrasound burst would begin just before the next laser pulse. The function generator used in this experiment was unable

to detect an incoming trigger while creating an ultrasound burst. This resulted in the PHIFU bursts occurring at a 15-Hz repetition rate, with each PHIFU burst synchronized with every other PHIL pulse. The synchronization between PHIL pulses and PHIFU bursts is shown in Figure 3.2. An oscilloscope (DPO 3034, Tektronix, Beaverton, OR) was used to confirm that the laser pulse arrived during the beginning of the ultrasound burst.

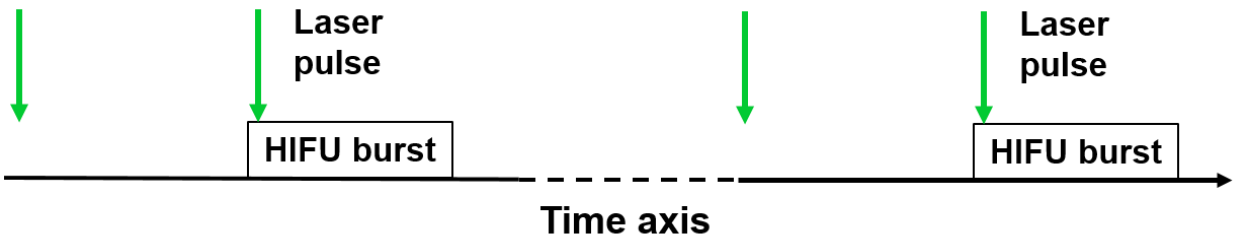

Figure 3.2: A diagram showing the synchronization of combined PHIL and PHIFU therapies. The HIFU burst is triggered by the laser pulse, however due to differences in travel time a delay is added to ensure that the next laser pulse is within the HIFU burst. The Laser pulse arrives at a frequency of 30 Hz. The HIFU burst lasts 1 ms and starts with a frequency of 15 Hz.

In order to select appropriate PHIFU treatment parameters, testing was performed on fresh *ex vivo* rabbit thighs muscles. Cavitation thresholds using PHIFU only were determined through the use of a flat transducer (V310, Olympus Scientific Solutions Technologies Inc., Waltham, MA) as a passive cavitation detector (Madanshetty, Roy, & Apfel, 1991). A ultrasound burst length of 1 ms with a peak negative pressure of 8 MPa was found to be just below the cavitation threshold. These values were selected to cause mechanical effects without causing cavitation in PHIFU alone. When both PHIL and PHIFU are combined cavitation was detected in the ex vivo thigh.

A standard calibrated needle hydrophone (0.5 mm Needle hydrophone SN 1462, Precision Acoustics, Dorchester, UK) on a 3D translational stage was used to determine the distribution of

the ultrasound emitted from the treatment probe while both were fully submerged in a tank of degassed water. The peak negative pressure of the ultrasound was measured along the central axis for the first 20 mm outside of the treatment probe, and radially at the focal point. The focal point was found to be 6 mm from the treatment probe with a width of 3.2 mm. The hydrophone was only used at pressures under 1 MPa. These results were extrapolated using a finite-difference time-domain (FDTD) simulation as described by Hallaj and Cleveland (Hallaj & Cleveland, 1999), and experimentally validated by Huang et. al. (Huang, Holt, Cleveland, & Roy, 2004a). Propagation of the ultrasound waves were simulated while accounting for nonlinear effects, acoustic absorption, and the acoustic properties of soft tissue. The simulation required the surface pressure of the transducer during a pulse. The relationship between input voltage and surface pressure of the transducer was determined by comparing hydrophone measurements with simulated results during linear conditions.

3.3.2 Animal Model

We have established a novel knee arthrofibrosis model based on New Zealand rabbit (Hazlewood, Feng, Lu, Yang, & Wang, 2018). New Zealand white rabbits were selected for the animal model due to the relatively large size of their knees. The rabbits were of mixed genders, and aged 6-8 months weighing between 2.8 and 3.6 kg at the time of surgery. Post traumatic joint contracture was created in the right knee of each rabbit through a single surgery. The rabbits were anesthetized through inhalational general anesthesia with isoflurane (to effect) after being sedated with ketamine (40 mg/kg) and xylazine (5 mg/kg). Animals were prepared and draped in the usual sterile fashion and placed in the supine position. A 15-blade scalpel was used to make a 3.5-cm longitudinal skin incision along the medial collateral ligament and the lateral collateral ligament of the right knee. The lateral 1/3 (posterior to LCL) and the medial 1/3 (posterior to MCL) of the

posterior synovium/capsule were transversely incised superficially and then completely disrupted by forceps. The middle 1/3 was partially disrupted by forceps.

In order to facilitate the scar formation in the posterior areas of the knee, a muscle flap was dissected out from the distal portion of biceps femoris, pulled towards the lateral side of upper tibia, and sutured with the superficial layer of the lateral head of gastrocnemius to hold the knee in a flexion position of approximately 60°. This procedure prevented the knee joint from extension (see Figures 3.2(c) and 3.2(d)). The flexed immobilization was further enhanced by pulling the superficial layer of the medial flexors together with absorbable sutures (4-0 Vicryl, Ethicon). The deep fascia was closed with absorbable sutures (4-0 Vicryl, Ethicon). The skin incisions were then closed with 4-0 non-absorbable sutures. E-collars were placed around the necks of the rabbits as they recovered from anesthesia. The non-operated left knee was used as a baseline control. After surgery, animals were allowed free cage activity. The operated rabbits were monitored for pain and received meloxicam (0.2 g/kg) as an analgesic as determined by the monitoring veterinarian.

3.3.3 Post-operative measurements

During the 8-week recovery period the operated knee was not immobilized, and the rabbits were allowed to use the leg as desired. This experimental design was chosen for multiple reasons. Firstly, by not immobilizing the knee it prevented knee contracture that might be due to the immobilization of the knee. Secondly, this reduced the amount of muscle atrophy in the musculature knee. Some atrophy is to be expected with arthrofibrosis of the knee, but additional atrophy would have been caused if the knee had been immobilized. Finally, allowing the rabbits to use the operated leg as desired dramatically reduced the stress in the rabbits.

A training program was also performed during the 8-week recovery period. The rabbits were wrapped in a towel and held by a researcher for increasing periods of time up to 20 minutes. At the end of this time the rabbit was rewarded with a small piece of fruit and returned to its cage. The goal of the training program was to acclimate the rabbits to being held in order to reduce stress and movement during later treatments and measurements of knee flexion contracture.

Starting eight weeks after the surgery, weekly measurements were performed to determine the severity of knee contracture. For the health of the rabbits they were not anaesthetized during these measurements. The rabbit was first wrapped in a towel and gently held in a position where it was laying on its side. The leg was exposed and the thigh was held against the body in a natural crouched position. The angle between the longitudinal axis of the femur and tibia were measured, with the center of the patella placed at the vertex of the angle. A strap was placed around the leg 10 cm from the knee. A force of 2 N was applied to extend the knee joint. The force was verified by a spring force gauge. The resulting torque of 0.2 N•m (or 20 N•cm) was the same as used in previous studies (Barlow et al., 2013; Nesterenko et al., 2009). Other studies have used a torque of 0.49 N•m (Fukui, Nakajima, Tashiro, Oda, & Nakamura, 2001; Fukui, Tashiro, Hiraoka, Oda, & Nakamura, 2000), however the lower value was selected to prevent any therapeutic effect from the additional stretching. Care was taken to ensure that the rabbit was not resisting or forcing the leg during the measurement. The extension angle from the 0.2 N•m torque between the femur and the tibia was measured. Net flexion contracture was calculated by taking the difference in maximum extension between the operated knee and contralateral control knee. Five repeated measurements throughout the course of a day were used to estimate the measurement error which was found to be 3°.

3.3.4 Treatment

Rabbits were randomly placed into one of four treatment groups. The first group received PHIL treatment. The PHIL group received 532 nm laser light with a surface fluence of 52 mJ/cm² at 30 Hz of 5-ns laser pulses (corresponding to ~10.4 MW/cm^2 peak intensity). The second group received PHIFU treatment. The PHIFU group received 1000 sine wave cycles of 1 MHz ultrasound with a peak negative pressure of 8 MPa (corresponding to ~2133 W/cm^2 peak intensity). The third group received combined PHIL and PHIFU treatment simultaneously. Finally a fourth group was used as a control without treatment. The combined group received both treatments at the same time, with every other laser pulse synchronized with the ultrasound burst (Figure 3.2).

Treatments were performed twice weekly. During each treatment, the rabbits were placed into a soft restraint cloth first. The restraint cloth covered the rabbit in soft material while providing a slit for the operated knee to be exposed. The restraint cloth also covered the eyes of the rabbits to prevent possible laser exposure. The knee was shaved with an electric razor to expose skin. A treatment area with a diameter of approximately 5 cm was selected on the lateral side of the leg slightly posterior to the tibial plateau. EMLA cream was applied to the treatment area for proactive pain relief. Ultrasound coupling gel was applied to the knee to insure acoustic transmission. Each treatment session lasted for 10 minutes. During this time the treatment probe was gently moved across the treatment area to prevent skin damage or irritation from prolonged treatment at a single location. Afterwards the ultrasound gel was wiped from the knee, and the rabbit was returned to its cage.

During the course of our treatment the rabbits very occasionally showed signs of distress, however in every case that this happened it appeared to be from the rabbit resisting the restraint as opposed

to a response to the actual treatment. If needed the treatment would be paused until the rabbit was calmed. These breaks took no longer than one minute.

Histology and Histochemistry

At the designated endpoints, rabbits were euthanized by the injection of 1 ml of commercial available euthanasia solution containing pentobarbital (Vortech Pharmaceuticals, Dearborn, MI). Upon euthanasia, both the operated and non-operated knee joints were harvested. The harvested knee joints were fixed in 10% buffered formalin (American MasterTech, Lodi, CA) for 7-10 days, then decalcified in 25% formic acid (Sigma, St. Louis, MO), and embedded in paraffin (Leica Biosystems, Richmond, IL). The samples were then sectioned at 5 μm, and stained with hematoxylin and eosin (H&E) to observe the general tissue structures. Safranin O and fast green stains were used to identify cartilage cells and matrices as described previously (Rodova et al., 2011; J. Wang, 2000; J. Wang et al., 2009; Xu et al., 2007). In order to identify the spatial relationship between the joint structure and scar tissues, the knee joint samples were sectioned in either cross or sagittal orientation.

3.3.5 Statistical Analysis

The resulting measurements of flexion contracture are presented as means ± standard deviation. The various means, were then compared using Student's t-Test (two-sample, two-tailed, unequal variance). Fisher's exact test was used to compare the recovery rates of the different groups, while Student's t-Test was used to compare the average recovery times. The null hypothesis was that there was no effect from the treatment regime compared to the control. Statistical significance for all studies was $p < 0.05$.

3.4 Results

3.4.1 Flexion Contracture Measurement

Weekly averages of net flexion contracture measurements for each group are summarized in Table 1. Once a rabbit reached a complete recovery, defined as maximal knee extension in both knees within measurement error, it was euthanized and considered to have a net flexion contracture of 0 degrees for all further weeks. Figure 3.3 shows the average time required for each group to make a complete recovery.

It can be seen that all three of the treatment groups eventually showed statistically significant improvement when compared to the control group. Additionally, all of the rabbits that received treatment made a complete recovery, while no subjects in the control group made a complete recovery within the 16 weeks of the study ($p = 0.008$). The average period of time required for complete recovery was 7.6 ± 1.5 weeks for the PHIL treated group, 9.8 ± 3.7 weeks for the PHIFU treated group, and 8.0 ± 2.2 weeks for the combined treatment group. However, the differences in average recovery time between all treatment groups were not statistically significant with the number of rabbits used in this study. One rabbit in the PHIFU treatment group was found to have additional bone growth in the treated knee, and also had the slowest recovery. However, the differences in average recovery time between all treatment groups were not statistically significant.

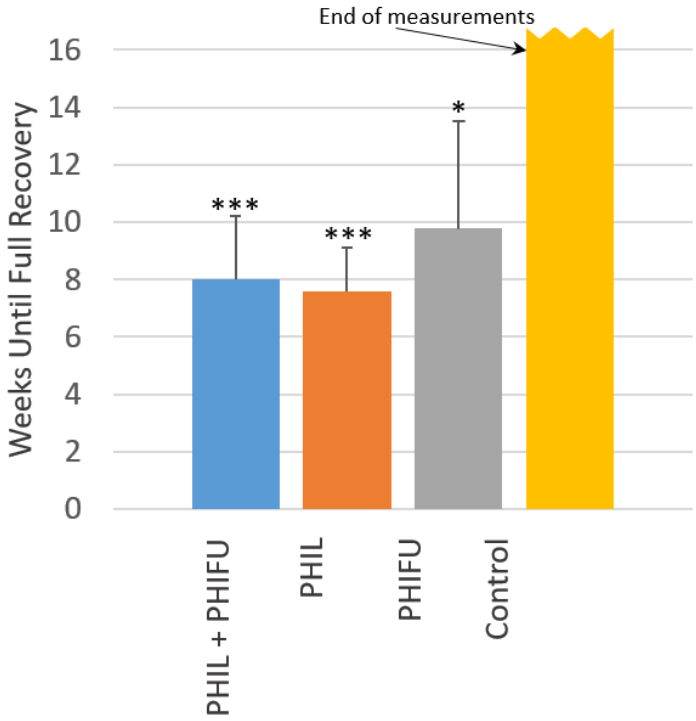

*Figure 3.3: A plot demonstrating the number of weeks required until complete recovery for each of the treated rabbits. No subjects in the control group made a complete recovery before the end of the study (16 weeks), while all of the treated rabbits regained normal range of motion. For statistical comparisons the control group was treated as recovering during week 16, however based on the relatively steady level of contracture it is most likely that the control subjects would have never regained normal range of motion. The * represents $p < 0.05$ when compared to the control group and *** represents $p < 0.001$ when compared to the control group.*

Table 3.1: Extension measurements were taken with a 0.2 Nm torque was applied to extend the knee. The net flexion results represent the difference between the maximum extension of the model knee and the contralateral control knee. Measurements were performed weekly for 16 weeks or until there was equivalent maximum extension in both knees. The p-values were determined through comparisons to the control group. The "" represents weeks when all subjects in the given group had made a full recovery.*

Weeks Post-Surgery	Control (N = 5)	PHIL (N=5)	PHIFU (N = 5)	Combined (N = 6)
8	22 ± 5.7	21.8 ± 5.4 (p = 0.956)	22.4 ± 4.9 (p = 0.908)	21.7 ± 6.8 (p = 0.932)
9	17.8 ± 2.6	20.6 ± 4.3 (p = 0.258)	22.8 ± 5.6 (p = 0.125)	16.7 ± 4.6 (p = 0.623)
10	24.4 ± 6.7	16.2 ± 5.5 (p = 0.068)	17.8 ± 6.7 (p = 0.156)	16.5 ± 5.2 (p = 0.065)
11	21.2 ± 6.2	17.8 ± 7 (p = 0.439)	18.4 ± 7.3 (p = 0.53)	13.7 ± 5.2 (p = 0.063)
12	20 ± 7.1	11.8 ± 4.6 (p = 0.067)	12.6 ± 7.2 (p = 0.139)	13.5 ± 6 (p = 0.142)
13	22.6 ± 4.3	10.6 ± 7.9 (p = 0.024)	13.2 ± 7.9 (p = 0.056)	10.2 ± 5.7 (p = 0.003)
14	17.4 ± 5.3	9.6 ± 8.4 (p = 0.122)	6.8 ± 4.4 (p = 0.009)	9.8 ± 7 (p = 0.071)
15	16.4 ± 4.2	4.6 ± 3.2 (p = 0.001)	7.4 ± 4.9 (p = 0.014)	4.5 ± 5.7 (p = 0.003)
16	19.2 ± 8.1	2.4 ± 4.8 (p = 0.006)	7 ± 4.5 (p = 0.025)	3.3 ± 5.3 (p = 0.008)
17	21.2 ± 4.8	*	4.2 ± 4.4 (p < 0.001)	3.5 ± 6.4 (p = 0.001)
18	18 ± 6.3	*	2.8 ± 2.8 (p = 0.003)	1 ± 3 (p = 0.002)
19	18.4 ± 4.7	*	2.4 ± 7.2 (p = 0.004)	*
20	14.6 ± 5.7	*	2 ± 4.5 (p = 0.005)	*
21	16.6 ± 2.3	*	1 ± 2.2 (p < 0.001)	*
22	17 ± 7.7	*	2 ± 4.5 (p = 0.008)	*
23	18.4 ± 7.8	*	*	*
24	17.8 ± 8	*	*	*

3.4.2 Histological Analysis

In the histological images of the non-operated knees, the normal joint capsules displayed intact fibrous structure with well-organized collagen orientation when viewed under polarizing lenses (Figures 3.4(A) and 3.4(B)). The untreated group demonstrated disorganized, dense scar formation in the area with capsule disruption with little evidence of scar tissue resorption (Figures 3.4(C) and 3.4(D)). The treated groups receiving PHIL, PHIFU, or PHIL plus PHIFU showed similar histopathological changes, characterized by less dense scar tissue with active capillary formation and vascular invasion, indicating the resorption of scar tissues. The representative micrographs taken from the PHIL plus PHIFU group are presented in Figures 3.4(E) and 3.4(F). No burnt nor necrotic tissues were observed in or around the joint, suggesting that the therapeutic methods used in this study are safe with no obvious tissue damage.

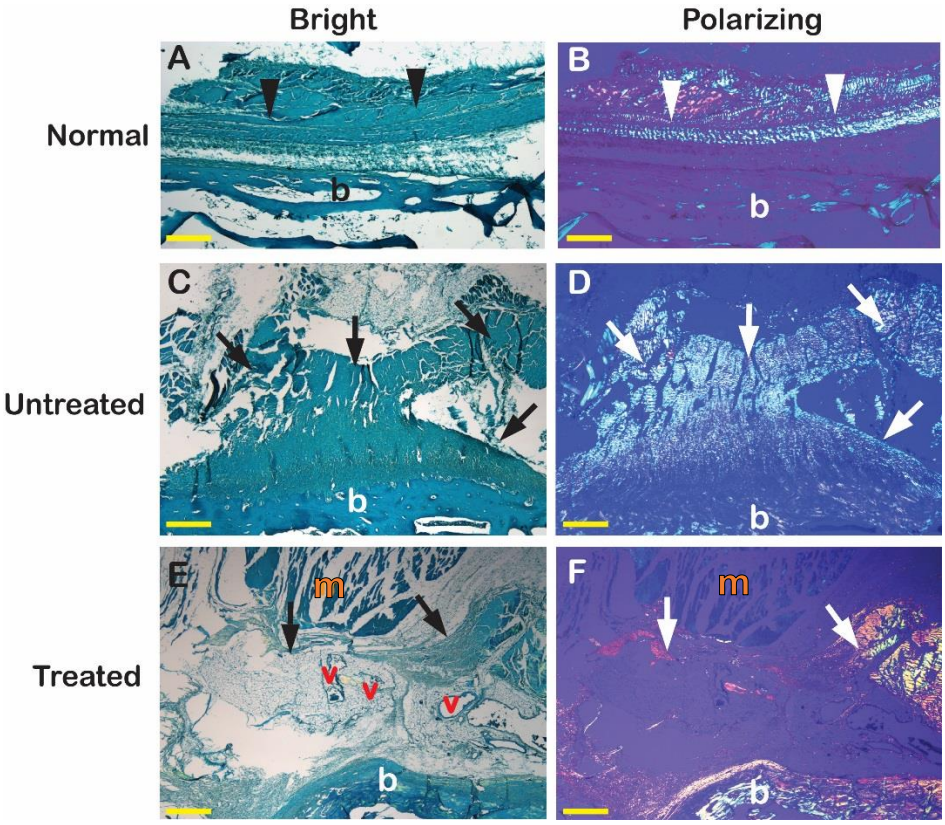

Figure 3.4: Micrographs of normal knee joint capsule (Normal), disrupted capsule without treatment (Untreated), and disrupted capsule with PHIFU plus PHIL therapy (Treated) in the posterior region of the knee at 24 weeks after posterior capsule disruption of rabbit knees. ***(A) and (B)****: Normal knee joint capsule in the posterior region of a non-operated knee.* ***(C) and (D):*** *An untreated knee with capsule damage showing dense scar formation in the posterior region of the joint.* ***(E) and (F):*** *A knee joint with capsule damage treated by a combination of PHIFU and PHIL showing less dense scar tissue with capillary formation (v). Arrowheads: normal joint capsule. b: bone tissue adjacent to the joint margin. Arrows: scar tissue formed in the disrupted capsule regions. v: newly formed capillaries or blood vessels in scar tissue. m: muscles. Safranin-O and fast green stains. Scale bar = 200 µm.*

3.5 Discussion

All three of the tested treatment groups showed a statistically significant improvement when compared to the untreated control, demonstrating that these modalities may be effective in the treatment of knee flexion contracture caused by arthrofibrosis. This conclusion was shown through weekly measurements of flexion contracture, as well as through histological analysis.

One rabbit in PHIFU group was found to have additional bone growth in the treated knee. This caused the joint to become wider than the contralateral control knee. This rabbit also had the longest recovery time of all of the treated subjects. The cause of this complication is unclear. It would be possible that prolonged PHIFU therapy caused pathological bone growth, or surgical damage to the joint capsule resulted in osteophyte formation. More investigation into this matter is warranted.

While all three treatments were effective, the differences in recovery times were not statistically significant when compared between treatment groups. We hypothesized that if both PHIL and PHIFU were successful, then the combined treatment would have even greater success, however all three treatment groups had similar results. The most likely cause is the large uncertainty in this study. The number of animals in this study was selected to determine if the treatments were effective compared to the control group. Additional studies with larger numbers of test subjects are needed to determine if there are statistically significant differences between the different treatment methods. Power analysis suggests that minimum groups of n = 25 are needed to compare the recovery times of PHIFU and PHIL groups.

The mechanism of action for PHIFU and PHIL treatment is not exactly clear. One of the possible mechanisms is the biomechanical stimulation induced by the ultrasound and laser. The high intensity used in PHIFU can produce mechanical effects such as acoustic radiation force (ARF) that may stimulate scar tissue resorption (ter Haar, 2007). These forces may cause a vibration at the pulse repetition rate similar to those used in vibrational therapy (Mano et al., 2015). PHIL utilizes high-peak-intensity laser with short pulse duration, typically less than 10 ns. As a result, PHIL can induce strong acoustic pulses through the photoacoustic (PA) effect in any tissue that has strong optical absorption at the peak intensity employed in the current study (Janggun Jo &

Xinmai Yang, 2016). The strong PA pulse may serve as a secondary source of vibratory stimuli on tissue, particularly for strongly optically absorptive tissue, such as fresh scars that contain high concentrations of hemoglobin.

The other possible mechanism is mechanical separation of the scar tissue, or cavitation. This may be achieved directly through the large rarefaction pressures to induce micro cavitation in the scar tissue. Because of the employed high intensity of laser and ultrasound, micro cavitation may be induced in fibrous tissues and cause micro lesions, resulting in the remodeling of the fibrous tissues and relief of the contracture.

Whenever high intensity laser and ultrasound are used, safety would be a concern. The laser fluence level used in the current study (52 mJ/cm^2) is greater than the laser safety limit for human skin exposure (20 mJ/cm^2) ("American National Standard for Safe Use of Lasers ANSI Z136.1-2007," 2007). However, we did not observe any burnt or necrotic tissues either on the skin nor inside the treated rabbit knees. In addition, our HIFU burst is only 1-ms, which is faster than a single nerve action potential. This is expected to lead to reduced perception of the burst in a similar fashion as seen is very short audio pulses (Everest, 2001). As a result rabbits did not show any resistance to the treatment, indicating that the treatment is safe and tolerable.

It should be noted that while it has been demonstrated that PHIL can successfully treat arthrofibrosis in rabbit knee joints, it is expected to have a reduced effect in human joints. The limited penetration depth of laser therapies is expected limit effective treatment of scars to those within one centimeter of the skin surface. Laser based therapies have an advantage over ultrasound based therapies by selectively targeting optically absorbent tissues. The limited penetration, and the selective targeting suggests that PHIL may be best suited to the treatment of smaller joints, or the parts of larger joints that are close to the surface. While PHIFU is more difficult to target, it is

able to achieve much greater penetration depths, suggesting that it holds great promise in the treatment of arthrofibrosis in shoulders, knees, and other larger joints.

Future work intends to refine the treatment parameters, such as duration and intensity, to optimize the treatment. An additional goal is to determine if these therapies can be applied during the initial recovery from an injury or surgery to prevent post traumatic joint contracture.

In conclusion, this study has shown important proof of concept success for PHIL and PHIFU therapies. Both methods as well as a combined treatment resulted in statistically significant improvement when compared to the untreated control group. This was shown through measurement of knee flexion contracture and histological analysis. All of the rabbits that received one of the treatments achieved a complete recovery, with a normal range of knee extension that was the same as that of the contralateral control knee. The rabbits in the untreated control group were unable to achieve a complete recovery and maintained a consistent level of flexion contracture.

Author Contributions Statement

J Wang, D. Hazlewood, and X. Yang: Substantial contribution to the design and conduct of animal experiment, the acquisition and interpretation of data, and manuscript preparation. Y Feng and Q Lu: Substantial contribution to the acquisition of data and manuscript preparation. All authors have read and approved the final submitted manuscript.

Acknowledgments

This work was supported by a medical research grant from the United States Department of Defense (DoD) under Award Number W81XWH-15-1-0524. The authors thank Dr. Da Zhang

(Professor of Pathology at the University of Kansas Medical Center) for his histopathological analysis of rabbit knee joints. The authors have no conflict of interest to declare.

Chapter 4 - Enhanced laser surface ablation with an integrated photoacoustic imaging and high intensity focused ultrasound system

4.1 Abstract

Background and objective: Combined laser and ultrasound treatments have been found to have synergistic effects, which may be of particular note in dermatology. We aim to investigate the potential of this technology for dermatology through *in vitro* and *ex vivo* experiments.

Methods: *In vitro* tissue phantoms made of agar and tattoo ink and tattooed *ex vivo* chicken breast tissue were used. An integrated photoacoustic imaging and high intensity focused ultrasound (HIFU) system, using a 5-ns tunable OPO laser system and a 5 MHz HIFU transducer, was used to perform photoacoustic analysis to identify the optical contrast, and perform combined laser and ultrasound ablation. On the tissue phantoms, lines of ablation were created under various operating conditions. The samples were then quantified to determine the level of ablation. The same procedures were performed on the tattooed chicken breast tissue and the tattoo was removed by using combined laser and ultrasound.

Results: Ablation in the *in vitro* tissue phantoms was observed with properly synchronized laser and ultrasound while no ablation was found with either laser or ultrasound alone. Increases to the intensity or pulse duration of ultrasound caused an increase in ablation to the samples. The tattoo was removed from the *ex vivo* chicken breast using combined laser and ultrasound with a radiant exposure of 1.2 J/cm^2 while laser and ultrasound alone were unable to remove the tattoo.

Conclusions: We determined that by supplementing nanosecond laser pulses with ultrasound, ablation and tattoo removal can be achieved at laser radiant exposures levels would otherwise be ineffective. The area of ablation can be adjusted through changes in the intensity and duration of

the ultrasound burst with a constant laser intensity. Additionally, the system can be used to perform photoacoustic analysis of the tissue to estimate the relative optical absorbance at various available wavelengths, allowing for pretreatment analysis.

4.2 Introduction

For the last half of a century lasers have served an important role in medicine. In 1983 Anderson and Parrish introduced selective photothermalysis (Anderson & Parrish, 1983), which was later expanded upon by Altshulur et al. (Altshuler, Anderson, Manstein, Zenzie, & Smirnov, 2001). During selective photothermalysis short laser pulses are used to destroy optically absorbent targets, without damaging the surrounding tissues. The ability to selectively destroy optically absorbent material has been widely used in dermatology allowing for the removal of skin discolorations (Franca et al., 2013; Klein, Baumler, Landthaler, & Babilas, 2011; Trafeli et al., 2007), hair follicles (Gan & Graber, 2013; Williams, Havoonjian, Isagholian, Menaker, & Moy, 1998), and tattoos (D. D. Ho, London, Zimmerman, & Young, 2002; Izikson, Farinelli, Sakamoto, Tannous, & Anderson, 2010; Kent & Graber, 2012; V. Ross et al., 1998; Vangipuram, Hamill, & Friedman, 2018). Alternatively, by using a laser wavelength that selectively targets the water in the dermis, widespread skin resurfacing can be achieved (Lowe et al., 1995; E. V. Ross, Domankevitz, Skrobal, & Anderson, 1996). More recent developments in laser technology have led to fractional laser resurfacing (Karabut et al., 2016; Manstein, Herron, Sink, Tanner, & Anderson, 2004) where narrow channels of deeper ablation are created with spaces of healthy skin between to promote rapid healing.

A 2006 survey found that 24% of men and women between 18 and 50 were found to have tattoos, but 16-21% of those with tattoos had considered getting at least one removed (Laumann & Derick, 2006). Generally, laser tattoo removal is expected to require 6-10 treatments, although brighter

colors especially yellows and oranges can be especially difficult to treat (Kent & Graber, 2012). Each treatment may cost $200. The most common complication following laser treatments is pigment changes (i.e. hypopigmentation or hyperpigmentation), which are generally more common in people with darker skin (Grevelink et al., 1996; W. S. Ho, Chan, Ying, & Chan, 2002). Testing of the treatment on a less visible section of skin is often performed to identify if complications are likely to occur. Lower radiant exposures can be used to prevent pigmentary changes, however the lower exposure level often leads to poorer outcomes and may require more treatments, increasing the cost to the patients. Non-laser techniques have been developed such as high intensity focused ultrasound (HIFU) (Lee et al., 2012) or radiofrequency (RF) (Bogle, Ubelhoer, Weiss, Mayoral, & Kaminer, 2007). However, lasers have remained the gold standard. This is in large part because HIFU and RF therapies have been found to be inconsistent and have not demonstrated a clear improvement over laser therapies (Stewart, Lim, Lowe, & Goodman, 2013).

In this study we are investigating the potential of using high intensity focused ultrasound to supplement existing laser treatments. Concurrent laser and ultrasound has been shown to cause multiple synergistic effects. Whiteside et al. demonstrated that ultrasound bursts can be used to increase laser penetration, by changing the optical properties of skin (Whiteside, Qian, Golda, & Hunt, 2017). Vangiparum et al. successfully used acoustic shock wave therapy after laser tattoo removal to improve clearance of the tattoo by increasing fluid transfer and lymphatic activity(Vangipuram et al., 2018). Jo and Yang found that combined laser and ultrasound treatment causes a dramatic increase in heating (J. Jo & X. Yang). Hu et al. demonstrated that combined laser and ultrasound can be used to selectively target micro-vessels without damaging the surrounding tissue (Hu et al., 2017). Similar studies have described how combined laser and

ultrasound resulted in increased cavitation (H. Cui, T. Zhang, & X. Yang, 2013), which has been used with optically absorbent nanoparticles for targeted cavitation (Farny, Wu, Holt, Murray, & Roy, 2005; McLaughlan, Cowell, & Freear, 2017). These previous ablation studies have looked at internal applications, while this study intends to explore dermatological applications.

The ability of combined laser and ultrasound to increase heating and micro-cavitation in tissue could be beneficial when applied to dermatological uses. This would allow for significantly lower radiant exposure levels to be used while still achieving thermolysis or ablation. By using ultrasound intensities that do not directly cause damage, collateral damage outside of the laser illumination can be avoided. Changes to the ultrasound parameters allow for changes in the size or intensity of the ablation while maintaining constant laser settings. Additionally, since ultrasound has excellent penetration through soft tissue and can be focused with HIFU transducers, ultrasound could be focused into the dermal layer to spare the epidermis. This could lead to applications that keep the surface of the skin intact while still targeting the underlying tissue.

The presence of ultrasound transducers could also be used to perform photoacoustic analysis of the targeted tissues to predict the effectiveness and likelihood of adverse reactions. The photoacoustic effect occurs when short laser irradiations cause brief thermal expansions in optically absorbent material. The thermal expansion then mechanically creates an ultrasound wave which can be detected by an ultrasound transducer. The strength of the ultrasound wave is related to the optical absorption of the sample. Detection of these waves is performed through photoacoustic imaging or photoacoustic tomography. The resulting data can be used to create an image based on the optical absorption of the sample, and can be used to identify biological structures with differing optical absorption in any available laser wavelength (L. V. Wang & Hu, 2012; H. F. Zhang et al., 2006). This technique has been applied *in vivo* to identify various

dermatological pathologies (Zabihian et al., 2015), and has been used to identify dyes used in fabrics (Golob, Jeler, & Gomilšek, 1996).

When performing selective photothermalysis, optimal treatment is achieved at a wavelength that separates the absorption coefficient of the targeted pigment from that found naturally in the skin (Altshuler et al., 2001). The absorption coefficient naturally found in patient's skin varies depending on natural skin tone. In the case of tattoo removal, the optical properties of the pigment are likely only generally known (Beute, Miller, Timko, & Ross, 2008). Using ultrasound transducers to perform photoacoustic testing with all available laser wavelengths will reveal which will provide the optimal treatment.

The generation and propagation of the photoacoustic signal can be modeled as in Eqn (1) as described by Wang and Wu (L. V. Wang & H.-i. Wu, 2007). The generation of the pressure wave can be seen on the left side of the equation, and the propagation of the wave can be seen on the right side.

$$\frac{-\beta}{C_p}\frac{\partial H(r,t)}{\partial t} = \left(\nabla^2 - \frac{1}{v^2}\frac{\partial^2}{\partial t^2}\right)p(r,t) \qquad (1)$$

β is thermal coefficient for volume expansion, C_p is the specific heat of the tissue at constant pressure, v is the speed of sound, $p(r,t)$ is the pressure at a particular location and time, and $H(r,t)$ is the heating function at a particular location and time. The heating function is further described in Eqn (2),

$$H = \eta\mu_a\Phi \qquad (2)$$

where η is the percentage of absorbed energy that is converted to heat, μ_a is the coefficient of optical absorption, and Φ is the optical fluence rate. When different laser treatments are used on

the same sample the only factors expected to change will be in the heating function. The optical fluence rate is primarily determined by the geometry and intensity of the laser irradiation, while η and μ_a are wavelength dependent. By performing preliminary testing at low radiant exposure levels it is possible to compare the changes in η and μ_a while causing negligible physical effects. The ability to predict the heating function in individual patients may lead to laser wavelength optimizations. The optical properties that determine the strength of photoacoustic signal are the same properties used in selective photothermalysis to preferentially target optically absorbent tissues. This information could be used for both thermal based treatments such as skin resurfacing and in treatments relying on mechanical effects from the thermal expansion such as scar or tattoo removal.

If ultrasound transducers are used to reduce the required laser intensity, a variety of laser systems may be available, including tunable OPO systems, despite their lower power outputs. The combination of an increased variety of laser wavelengths and photoacoustic testing could be especially valuable for tattoo removal. An OPO laser system would be able to test the spectra of various pigments in a similar fashion as has been used to identify fabric dyes (Golob et al., 1996). The spectra of the tattoo could then be compared to the spectra of the patient to find the optimal treatment wavelength.

In this study we will use a nanosecond laser and ultrasound system to demonstrate combined irradiation to create ablation in agar tissue phantoms. The effects of changing various parameters will be tested to explore the underlying mechanics of the ablation. By performing ablation on the surface of tissue phantom under a variety of treatment parameters, consistent images can be taken and processed for quantitative analysis over a variety of treatment parameters. The techniques

explored through the *in vitro* experiments will be applied to a tattooed *ex vivo* chicken breast to attempt tattoo removal.

4.3 Materials and Methods

4.3.1 System

The experimental setup involved the use of a 10-Hz, 532 nm pump laser (Surelight SLI-30, Continuum, Santa Clara, CA) and an OPO system (SLOPO Plus, Continuum, Santa Clara, CA) which was used to provide 5-ns laser pulses with wavelengths between 680-800 nm. The laser system additionally triggered a function generator (33250A, Agilent Technologies, Santa Clara, CA) that was connected to a power amplifier (350L RF Power Amplifier, ENI Technology Inc., Rochester, NY), and then to a 5 MHz spherically focused HIFU transducer (SU-108-013, Sonic Concepts, Bothell, WA). A photoacoustic imaging system, as described in Jo and Yang(J. Jo & X. Yang, 2016), held the transducer and laser light in alignment. A diagram of the system can be seen in Figure 4.1. The coaligned laser and transducer spots were focused on the surface of the sample. Both the laser and ultrasound spots had a gaussian distribution and matching full width half maximum (FWHM) of 0.6 mm at the surface of the sample. A 3D scanning stage (Thorlabs, Newton, NJ) was used to move the system across the sample. The movement of the system was at a speed of 0.5 mm/s. Repeated treatments of any locations on the sample were avoided. A pulse/receiver system (Panametrics NDT, Olympus, Center Valley, PA) was used to ensure correct alignment of the laser and ultrasound.

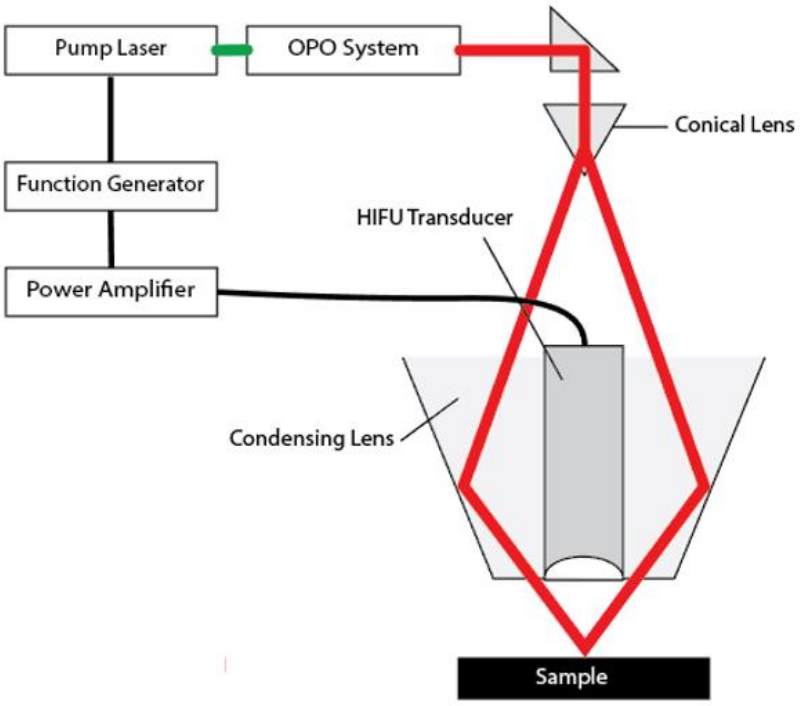

Figure 4.1: A diagram of the photoacoustic imaging/ablation system. The pump laser is used to supply 532 nm light at 10 Hz to the OPO system where it is converted to the selected wavelength, such as 680 nm. The resulting light is directed into a conical lens and into a condensing lens to bend the light around the transducer to the transducer. The function generator is triggered by the pump laser. The signal is then amplified and delivered to the HIFU transducer.

A delay was added in the function generator to synchronize the arrival of the laser and ultrasound at the surface of the sample. The precise time between laser pulses was 100.1978 ms, and the travel time of the ultrasound wave from the transducer to the sample was 0.0233 ms. A delay of 100.1700 ms was added at the function generator to ensure that the ultrasound burst was in effect at the surface of the sample 4.5 μs before the laser pulse arrived.

During synchronized laser and ultrasound radiation, the trigger from the first laser pulse was used to generate an ultrasound burst which would travel to the sample and synchronize with the second laser pulse. The duration of ultrasound burst was greater than the travel time of the ultrasound

wave, meaning the function generator was still generating the signal while the second laser pulse was fired. Our function generator was unable to detect a trigger while generating a signal. As a result, the function generator could only be triggered again by the third laser pulse and the resulted ultrasound burst would synchronized with the fourth laser pulse. Therefore, ultrasound was only applied to every other laser pulse.

The acoustic pressure produced by the HIFU transducer at the focal spot was measured with a standard needle hydrophone (0.5 mm Needle hydrophone SN 1462, Precision Acoustics, Dorchester, UK), and then further simulated through FDTD code developed by Hallaj and Cleveland (Hallaj & Cleveland, 1999), which was verified by Huang et al. (Huang, Holt, Cleveland, & Roy, 2004b). This calibration allowed for an estimation of the peak pressure from the ultrasound burst at various input voltage levels from the function generator.

Testing was performed in a tank of degassed and deionized water. The position and speed of the stage were controlled by a connected computer. The OPO laser system was primarily used to provide 5 ns pulses of 680 nm light at 10 Hz, which were the optimal operating conditions of the system. The laser and focusing system had a minimum radiant exposure of 1.2 J/cm² during normal operation, which was used as a baseline for most experiments. The baseline ultrasound parameters were 200 μs bursts of 5 MHz ultrasound with a peak negative pressure of 3.6 MPa. The resulting ultrasound duty cycle was 0.01%, preventing an overall temperature increase from ultrasound irradiation. The negative pressure in this study is lower than was used by Zhou and Gau which was up to 15.7 MPa (Zhou & Gao, 2013). The radiant exposure levels of the laser are also less than those normally seen in treatments. Izikson et al. compared an alexandrite 755 nm 30-50 ns laser with a 758 nm 500 picosecond laser with minimum radiant exposures of 8 J/cm² and 2.6 J/cm² respectively (Izikson et al., 2010), both of which used greater radiant exposure than

1.2 J/cm² as used in this study. Ross et al. used an Nd:Yag laser with 10 ns pulses that was also operated with a 8 J/cm² radiant exposure (V. Ross et al., 1998).

4.3.2 Image Processing

All the experiments involved scanning the system across the sample using the motorized stage during treatment. The lines were 10 mm long and 2 mm apart from each other. Once the treatment was complete the samples were taken for microscopic imaging. The resulting images were then analyzed and quantified through MatLab (MathWorks, Natick, MA). Quantification was performed by thresholding the images and then calculating the average width of the line of removed material. The threshold for the images was set at the highest level possible that did not include the untreated surfaces between the lines of ablation. An example of this process is seen in Figure 4.2. All trials of any particular test were performed at one time on the same tissue phantom. Multiple images were taken as needed to image all trials. Identical lighting conditions and image processing (including the same threshold values) were used for all images of the same data set.

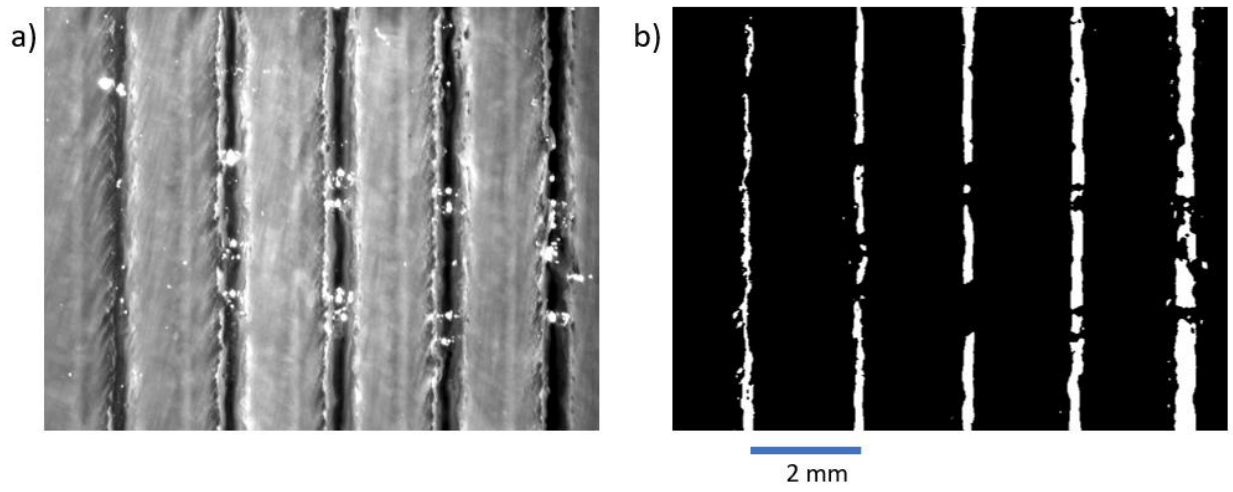

Figure 4.2: An example of the image processing and quantification of results. a) The base image of the sample. b) The image after thresholding. The average width of each line after thresholding was used to quantify the ablation.

4.3.3 Tissue phantoms

The *in vitro* tissue phantoms were created using a 2% agar (Agar pure powder, ThermoFisher Scientific, Waltham, MA) solution as described by Zell et al. (Zell, Sperl, Vogel, Niessner, & Haisch, 2007). Black tattoo ink (True Black, BZ Ink, Dragon tattoo supply, Dayton, OH) was added to the solution to provide optical absorption. The solution was poured into a cylindrical mold, which was slightly over filled so that the sample was slightly domed. The excess material was removed from the top of the sample to create a level surface. The sample was then removed from the mold and flipped over so that the smooth bottom was used as the testing surface.

4.3.4 Experimental Procedure

A series of five experiments were performed in this study. The goal of the experiment 1 was to demonstrate that the photoacoustic system was capable of photoacoustic spectroscopy through the same laser system and ultrasound transducer that would later be used for ablation. Experiments 2-4 examined changes to the level of ablation in tissue phantoms when the synchronization, intensity, and pulse duration were changed independently. The results were imaged and quantified for comparison. In experiment 5 the synergistic effects of combined laser and ultrasound seen in the previous experiments are demonstrated *ex vivo* by removing a tattoo from chicken breast tissue.

Experiment 1: Photoacoustic spectrometry - To demonstrate the ability of the photoacoustic system to perform photoacoustic spectroscopy, 5 tissue phantoms were created with 5 different commercially available tattoo inks: true black, cherry bomb (red), teal, dragon green, and lemon yellow (BZ ink, Dragon tattoo supply, Dayton, OH). To create the colored samples 0.06% concentrations of the tattoo dyes were used. The spectra of each of these dyes was determined with a spectrophotometer (Evolution 600, Thermo scientific, Waltham, MA) over the visible and

near infrared portions of the spectrum from 400-800 nm. The OPO system was then used to measure the photoacoustic signal generated by each of these sample from a range of 680-800, and the results were compared. Thirty-two photoacoustic measurements were averaged for each wavelength on each sample.

Experiment 2: Laser-ultrasound synchronization - The optimal delay time between the start of the ultrasound and laser was examined by varying the delay used in the function generator. For this experiment the laser was operated at 680 nm with a radiant exposure of 1.2 J/cm². The ultrasound burst duration was 200 µs with a peak negative pressure of 3.6 MPa. A variety of synchronizations were tested with the laser pulse arriving before, during, or after the 200 µs ultrasound burst. The goal of this experiment was to examine if direct interaction of the laser pulse and ultrasound burst were required to create a synergistic effect, and to determine what the optimal synchronization between the two should be. For consistency the ultrasound was always triggered by every other laser pulse even when it was possible to trigger on every pulse.

Experiment 3: Intensity testing - Ablation was also tested using different laser and ultrasound intensities. For this experiment the laser was operated at 680 nm with radiant exposures of 1.2 J/cm² and 1.8 J/cm², which were the lower and upper limits of the our system for radiant exposures. These radiant exposure levels were both well below the 8 J/cm² generally used to represent clinical treatments (Izikson et al., 2010; V. Ross et al., 1998) and had no visible effect without supplemental ultrasound. Both radiant exposure levels were tested with a variety of supplemental ultrasound intensities with peak negative pressures ranging up to 4.3 MPa. The goal of this experiment was to identify the threshold of ultrasound intensity to create ablation for each of the laser radiant exposures, and to compare the different levels of ablation at various laser and ultrasound intensities. A constant ultrasound burst duration of 200 µs was used in this experiment.

Experiment 4: Ultrasound burst duration - Changes in ablation as the ultrasound burst duration was varied were explored. The burst duration was varied from 40-2000 μs by changing the number of cycles in the 5 MHz ultrasound burst. The laser was operated at a 680 nm with a radiant exposure of 1.2 J/cm². The peak negative pressure of the ultrasound burst was 3.6 MPa. Timing was set so that the laser would consistently arrive 4.5 μs into the ultrasound burst at the surface of the sample. This test was used to determine if all portions of the ultrasound burst were responsible for the synergistic surface ablation or if only the portion that overlapped with the laser pulse contributed.

Experiment 5: Ex vivo tattoo removal - To confirm that tattoo removal could be achieved with the photoacoustic system a black line was tattooed onto chicken breast tissue with a commercial tattoo gun (Dragon tattoo supply, Dayton, OH). A photoacoustic image of the tattoo was taken, and tattoo removal was performed. The laser radiant exposure used for both the imaging and removal was 1.2 J/cm² with 680 nm light. The peak negative pressure of the ultrasound burst was 4.3 MPa and the ultrasound burst length was increased to 4 ms where tattoo removal was observed. The effects of laser alone and ultrasound alone were compared with the combined treatment. The goal of this experiment was to demonstrate that tattoo removal was possible with the lowest radiant exposure of our system when supplemented with ultrasound.

4.3.5 Statistical analysis

The width of each line was calculated by counting pixels in each row of the thresholded images and converting to physical units. The widths of each row in the image were then averaged and presented as mean ± standard deviation. If there was a problem in any region of the image (i.e a crack in the tissue phantom) the same portion was removed from each of the lines for calculations.

Differences between two groups was determined using Student's t-Test. Statistical significance was set at $p < 0.05$.

4.4 Results

Experiment 1: The spectra from spectrophotometry for the 5 different colored samples (black, teal, green, yellow, and red) are shown in Figure 4.3a. The absorbance peaks of the teal, green, yellow, and red samples were 608, 429, 555, and 434 nm respectively. The black dye did not have a peak over the tested wavelengths, but absorbance was highest at 400 nm and gradually dropped off as the wavelength was increased. The wavelengths that were used for the photoacoustic measurements covered the red and near infrared portions of the spectrum from 680 to 800 nm. Figure 4.3b-f show the normalized results from photoacoustic spectroscopy and its comparison with spectrophotometry over the range used for photoacoustic spectroscopy. As expected the teal and green samples had a stronger photoacoustic signal near the peaks identified by spectrophotometry. The red and yellow samples had very little change in the 680-800 nm range due to the low absorption predicted by spectrophotometry. These results demonstrate that photoacoustic spectroscopy can be performed using the same laser and ultrasound transducer that will be used for ablation. There are some differences in the comparisons between the photoacoustic measurements and the spectrophotometry results. This is likely because spectrophotometry is effected by both light scattering and absorptions in the medium, while the photoacoustic signal is largly determined by absorptions as well as the Grüneisen constant. Photoacoustic testing may be used when the absorption peaks of the dyes are unknown, or it may be used to compare the relative absorption bewteen the targeted tissue and the surrounding tissue at various wavelengths. During the course of photoacoustic measurements no ablation was seen

in the samples, this suggests that every other laser pulse that is out of sync with the ultrasound burst would be ineffective.

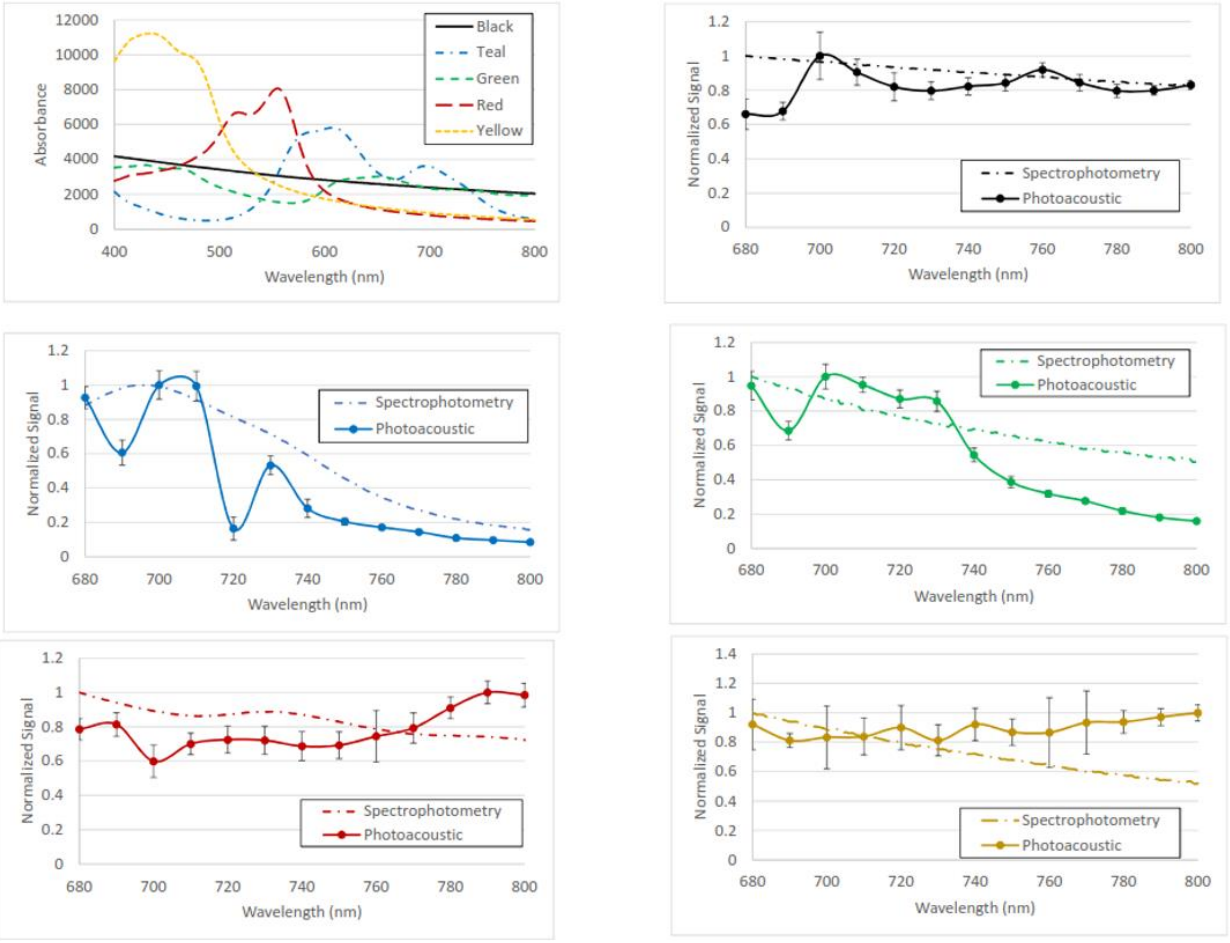

Figure 4.3: Experiment 1 - a) The absorbance spectra, using spectrophotometry from 400-800 nm, of five tissue phantoms colored with different dyes black, teal, green, red, and yellow. The peak wavelength for each of the samples: black - 400 nm, teal – 608 nm, green – 429, red – 555, yellow – 434. b-f) The normalized results of the photoacoustic spectra are compared to the spectrophotometry results in the 680-800 nm range for each of the dyes. b) black, c) teal, d) green, e) red, and f) yellow. Error bars represent standard deviations of 32 measurements.

Experiment 2: Synchronization testing was performed to determine the optimal arrival time of the laser pulse relative to the ultrasound burst. The results can be seen in Figure 4.4. All times in the plot are based on the surface of the sample accounting for travel time of the ultrasound burst, and

were verified with an oscilloscope. When the laser arrived at the surface of the sample 34.5 µs or more before the arrival of the ultrasound burst, only a small amount of ablation was seen. When the laser arrived within 24.5 µs of the ultrasound burst the width of ablation was similar to when the laser arrived during the beginning of the ultrasound. The width of ablation dropped as the laser arrived further into the ultrasound burst until no ablation was seen. When the laser arrived after the ultrasound no ablation was seen.

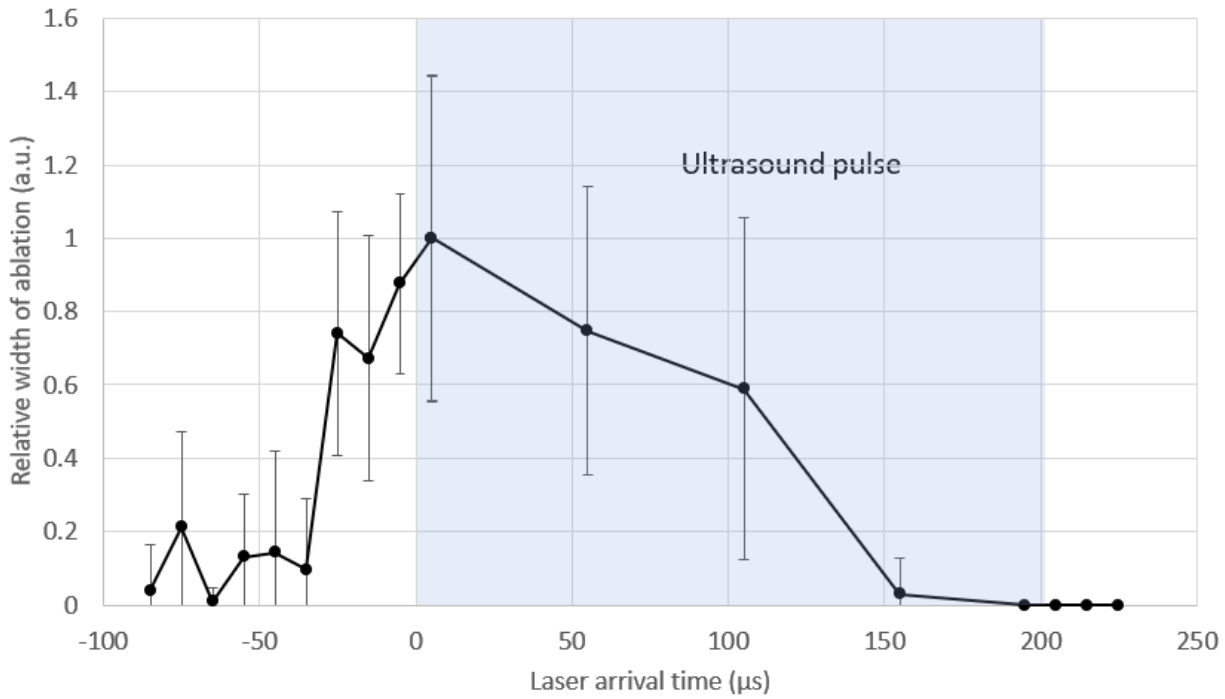

Figure 4.4: Experiment 2 - The results of changing the synchronization between the arrival of the laser pulse and ultrasound burst at the surface of the tissue phantom. Negative times represent the laser pulse arriving before the ultrasound burst. The shaded region indicates the time where the 200 µs ultrasound burst was in effect. Error bars represent standard deviations of 150 width measurements of each line of ablation.

The similarities in ablation between trials where the laser arrived during the beginning of the pulse and just before the pulse suggests that the laser pulse is causing an effect on the sample that lasts longer than would be expected for the pressure wave in a photoacoustic signal. The creation of

nano- or micro-bubbles through cavitation from the laser pulse is one possible reason that the laser arriving before the ultrasound burst can still enhance ablation, because the residual cavitatioign may be caught up by the subsequent ultrasound burst. The lifetime of the laser induced bubbles would then determine the length of time that the laser could arrive before the ultrasound burst to enhance ablation, which may explain the reduction in ablation as the laser pulse arrives further ahead of the ultrasound burst, as fewer bubbles survived until the arrival of the ultrasound burst. These results provide further evidence that every other laser pulse that was not supplemented with ultrasound should provide negligible effect compared to the properly synchronized pulses.

Experiment 3: Figure 4.5 demonstrates the changes in ablation for two different radiant exposure levels (1.2 J/cm² and 1.8 J/cm²) as the intensity of the ultrasound was increased. A minimum ultrasound threshold to cause ablation was noted in each case. Any trials with an ultrasound pressure below that threshold did not result in ablation. When the laser radiant exposure was 1.2 J/cm², ablation was seen when the ultrasound had a peak negative pressure equal or greater than 2.8 MPa. When the radiant exposure was raised to 1.8 J/cm², ablation was seen starting at 1.9 MPa. Overall the width of ablation was greater when either the radiant exposure of the laser or the magnitude of the ultrasound pressure was increased. Greater ablation was seen in all trials with 1.8 J/cm² radiant exposure compared to trials with 1.2 J/cm² radiant exposure with the same ultrasound intensity.

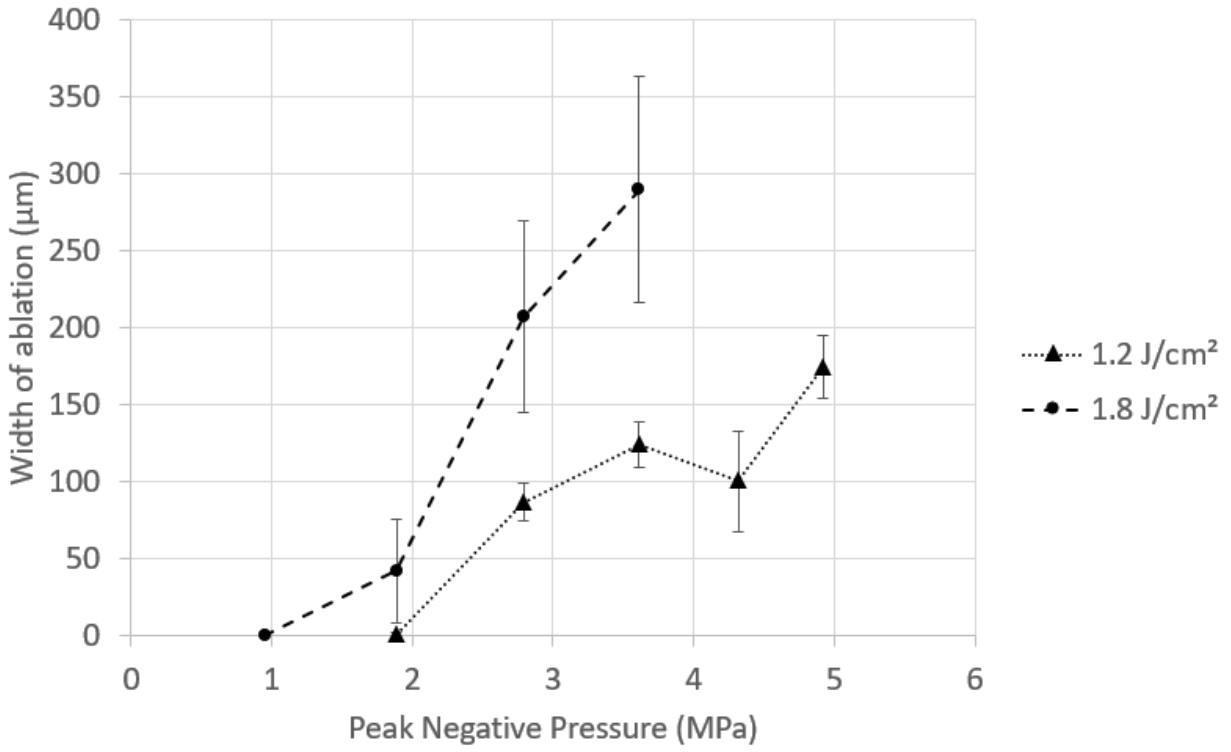

Figure 4.5: Experiment 3 - The results of various ultrasound intensities with two different radiant exposures. Both radiant exposures displayed a threshold pressure that was required to cause ablation. The higher laser radiant exposure decreased the required pressure threshold. It is additionally seen that increasing the intensity of the ultrasound pressure, the level of ablation is increased. Error bars represent standard deviations of 400 width measurements of each line of ablation.

Experiment 4: The effect of the ultrasound burst duration is presented in Figure 4.6. It is clearly seen that the ultrasound burst duration had a direct impact on the area of ablation. The increase in ablation was much more noticeable at the shorter durations than the longer durations, indicating that there may be an upper limit to the increase in ablation that can be caused by increasing the ultrasound burst duration. These results support the findings in the synchronization testing, where the width of ablation gradually decreased as the laser pulse arrived later in the ultrasound burst.

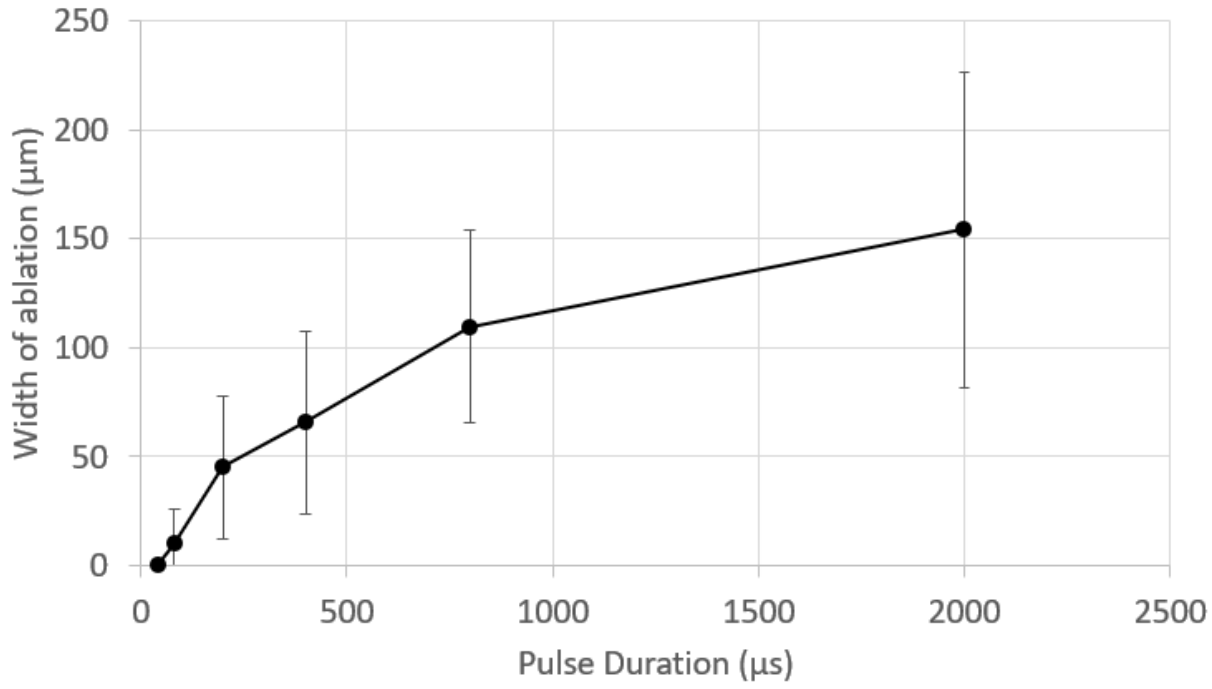

Figure 4.6: Experiment 4 - The results of various ultrasound burst lengths. As the pulse lengthened the width of ablation increased, indicating that ablation occurred throughout the whole ultrasound burst not just at the portion that overlapped with the laser. Error bars represent standard deviations of 400 width measurements of each line of ablation.

Experiment 5: The synergistic effects from combined laser and ultrasound seen in the *in vitro* results were used to remove tattoo ink from an *ex vivo* chicken breast. Photoacoustic imaging was performed on the tattoo and is presented in Figure 4.7a. The average photoacoustic signal of each pass across the tattoo is presented in Figure 4.7b where a significant increase in photoacoustic signal is seen in the tattoo compared to the surrounding tissue. The tattoo was treated with ultrasound alone, laser alone and a combined treatment in Figure 4.7c. The ultrasound alone did clear the tattoo ink that had stained the surface but was ineffective at removing the deeper ink. The

laser treatment alone had no effect on the tattoo. The combined treatment was able to remove the tattoo completely.

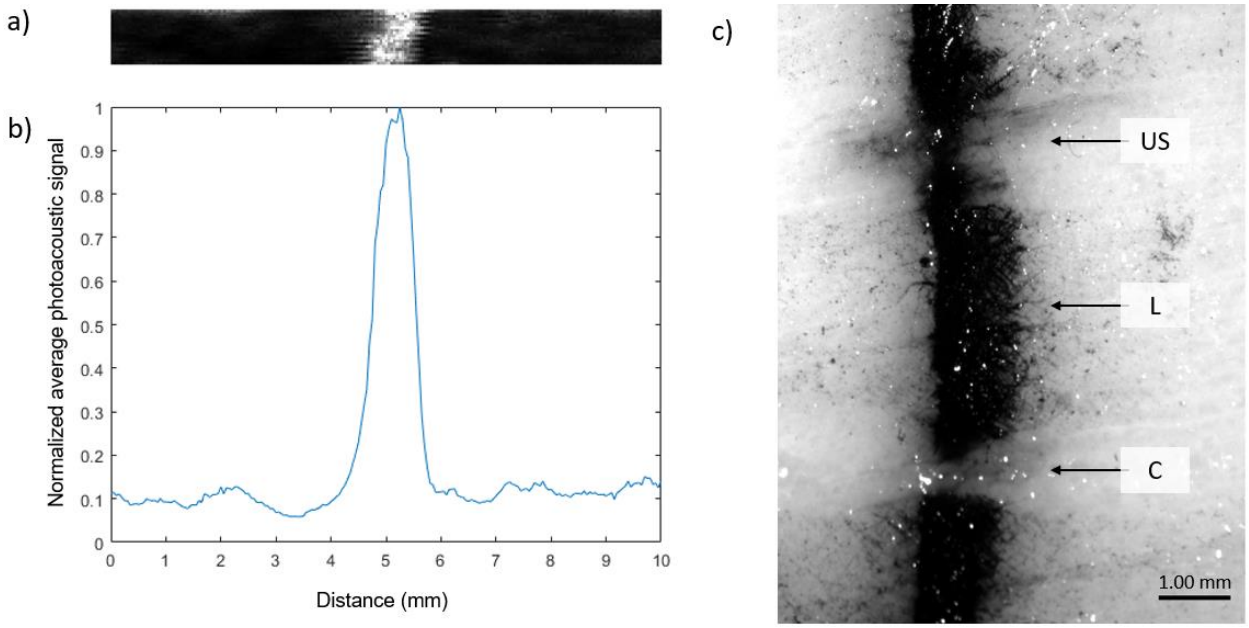

Figure 4.7: Experiment 5 - a) Maximum amplitude projection (MAP) of a photoacoustic image taken of a tattooed ex vivo chicken breast. b) Average photoacoustic signal from each of the passes across a sample in the photoacoustic image. c) An image of the sample after applied treatments from the ultrasound alone (US), the laser alone (L), and the combined laser ultrasound treatment (C).

4.5 Discussion

The results of this study show that our integrated photoacoustic imaging and HIFU system can be used to supplement laser surface ablation and allows for photoacoustic analysis of the targeted tissues. It is possible to use laser and ultrasound intensity that independently are unable to cause damage, but in conjunction the surface of the tissue phantom can be removed. The radiant exposure of 1.2-1.8 J/cm² used in this study with supplemental ultrasound was able to cause ablation and perform tattoo removal on an *ex vivo* sample, compared to other studies where 8 J/cm² was used to represent clinical treatments (Izikson et al., 2010; V. Ross et al., 1998). It is expected that as the exposure level of the laser is reduced, higher ultrasound intensities and pulse durations

could be used to compensate. However, the selectivity of the laser treatment would be expected to be reduced.

Our study also shows that combined ultrasound and laser ablation is not simply the result of the combined pressure waves. If the combined pressure wave from the laser and ultrasound were solely responsible for the ablation, then changes to the length of the ultrasound burst would not be expected to enhance the level of ablation. Cavitation as described by Cui et al. (H. Cui et al., 2013), is most likely the cause of the tissue phantom surface removal that was observed in this study, although this study demonstrated that the a synergistic effect is seen even when the laser and ultrasound are slightly out of synchronization. If cavitation was initiated by the laser, then the ultrasound would be able to drive the bubbles to cause further damage to the sample. Using ultrasound driven bubbles to cause ablation has been used in treatments where micro bubbles are injected into the blood stream and driven externally by ultrasound (Chung, Cho, Lee, & Hahn, 2012). The demonstration that changes in ultrasound pulse duration and intensity can dramatically impact the level of ablation, may have impact outside of tattoo removal and dermatology. The phenomenon seen in this study may apply to the other treatments using combined laser and ultrasound.

It should be noted that only one laser configuration was used in this study which uses and tunable OPO system which is not representative of clinically available systems. However, it is expected that ultrasound will provide similar synergistic benefits to most other laser sources, including continuous lasers, picosecond lasers, fractional lasers or future laser developments. Future work will need to be performed to replicate these results *in vivo*, and to examine the biological response to combined laser and ultrasound ablation. Additional studies are needed to directly compare the effectiveness of combined laser and ultrasound treatments with more traditional laser therapies.

4.6 Conclusion

This study demonstrates that when both laser and ultrasound are used simultaneously, ablation can be enhanced when compared to laser-alone or ultrasound-alone. Changes to the parameters of the ultrasound burst can be used to easily adjust the level of ablation while maintaining constant laser parameters. Additionally, the introduction of ultrasound transducers allows for photoacoustic analysis which can be used for pretreatment estimates of the response in the targeted tissue from laser treatments. The benefits from supplemental ultrasound to existing laser-based therapies may be beneficial in dermatology and other medical fields.

Acknowledgements

This work was supported in part through a National Institute of Health (NIH) grant R01EY029489. The authors have no conflict of interest to declare.

Chapter 5 - Enhanced cavitation activity in a slab-shaped optical absorber during photo-mediated ultrasound therapy

5.1 Abstract

Recently, new studies have shown that combined laser and ultrasound, or photo-mediated ultrasound therapy (PUT), can enhance cavitation in optically absorptive targets to disrupt tissues through photoacoustic (PA) effect. These studies, including both experimental and theoretical investigations, have largely focused on blood vessels, which are modeled as cylindrically-shaped optical absorbers for PA wave generation and propagation. However, in many clinical situations, target tissues may not be cylindrically-shaped. In this paper we investigated the effect of PUT on a slab-shaped optical absorber, much larger than the size of the laser beam or the ultrasound focal point. Our results demonstrated that laser light could generate a PA wave that could enhance cavitation not only at the surface of a slab, but also at depths beyond the reach of the laser light itself when combined with ultrasound, suggesting that PUT may be effective in enhancing cavitation in a large range of soft tissues. Our results also demonstrated that the cavitation enhancement was based on the optical absorption coefficient of the targeted tissue, allowing for self-targeting treatments when optical contrast is present. Additionally, we demonstrated that for the greatest cavitation enhancement in deeper layers a focused laser beam geometry would be most effective.

5.2 Introduction

Cavitation is a potentially destructive process where a void or vapor bubble is created in a liquid phase, generally due to a strong rarefaction pressure located at some bubble nucleation sites (Leighton, 1994). When these bubbles collapse, through a process known as inertial cavitation, strong shock waves are emitted. The shock waves can cause significant damage, but their range is limited to approximately the size of the bubble prior to collapse. Traditionally research has been performed to predict and prevent cavitation due to diagnostic ultrasound for the safety of the patient (Apfel & Holland, 1991). On the other hand new applications using high intensity focused ultrasound (HIFU) are being developed that utilized the destructive nature of cavitation for therapeutic effects such as disrupting dense fibrous tissues (Yeh, Li, Shih, Huang, & Kuo, 2013a), opening the blood brain barrier (Burgess, Apostolakis, & Konofagou, 2018; Tung, Vlachos, Feshitan, Borden, & Konofagou, 2011), and occluding veins (Hwang, Zhou, Warren, Brayman, & Crum, 2010).

Photoacoustic (PA) cavitation has been studied (Paltauf & Schmidt-Kloiber, 1999), where a laser pulse with a very short duration causes concentrated thermal expansion in an optical absorber in what is known as the PA effect (McDonald & Wetsel, 1978). This thermal expansion can cause strong stresses waves in and around the optical absorber. The shape of the emitted stress wave is determined by the geometry of the optical absorber, with spherical and cylindrical geometries generating the strongest rarefaction pressures (Paltauf & Schmidt-Kloiber, 1999). The resulting pressure wave can cause cavitation in and around the optical absorber. Cavitation induced by this mechanism is through photomechanical effect at a temperature that is much less than vaporization.

Based on the abilities of ultrasound and lasers in creating cavitation, a growing body of research develops new treatments based on the synergistic effects of combined HIFU and laser therapies in

a process sometimes called photo-mediated ultrasound therapy (PUT) (Huizhong Cui & Yang, 2011; H. Cui & Yang, 2013; Hazlewood, Feng, Lu, Wang, & Yang, 2018; Hazlewood & Yang, 2019; Hu et al., 2017; J. Jo & X. Yang, 2016; H. Zhang et al., 2018). PUT delivers synchronized laser pulses and HIFU bursts. Ideally the intensity of the treatments would be adjusted such that the ultrasound and PA pressures alone are not enough to cause inertial cavitation, but when the pressure waves are combined inertial cavitation occurs. Optical contrast can be used to selectively target tissues with high optical absorption, while leaving the surrounding tissue with lower optical absorption undamaged.

PUT has shown promise in targeting blood vessels (H. Cui & Yang, 2013; Hu et al., 2017; H. Zhang et al., 2018), and a computer model of the process has been created to explore cavitation from PUT in blood vessels (S. Li, Qin, Wang, & Yang, 2018). Li et al. found that when targeting blood vessels with PUT, the cylindrical geometry of the blood vessel created a very high amplitude pressure wave along the central axis, which greatly enhanced cavitation.

In the current study, we are modeling the effects of PUT on a flat slab-shaped optical absorber, mimicking the surface of the skin, and just below the surface. The model will consist of slabs of homogenous tissue without small optical absorbers such as blood vessels, and the illumination geometry of the laser beam will be cylindrical geometry. We have previously demonstrated that enhanced ablation occurs on tissue surfaces during PUT (Hazlewood & Yang, 2019). The current investigation will provide a theoretic explanation for these results by modeling the enhanced cavitation activity while simultaneous PA and ultrasound pressure waves are applied.

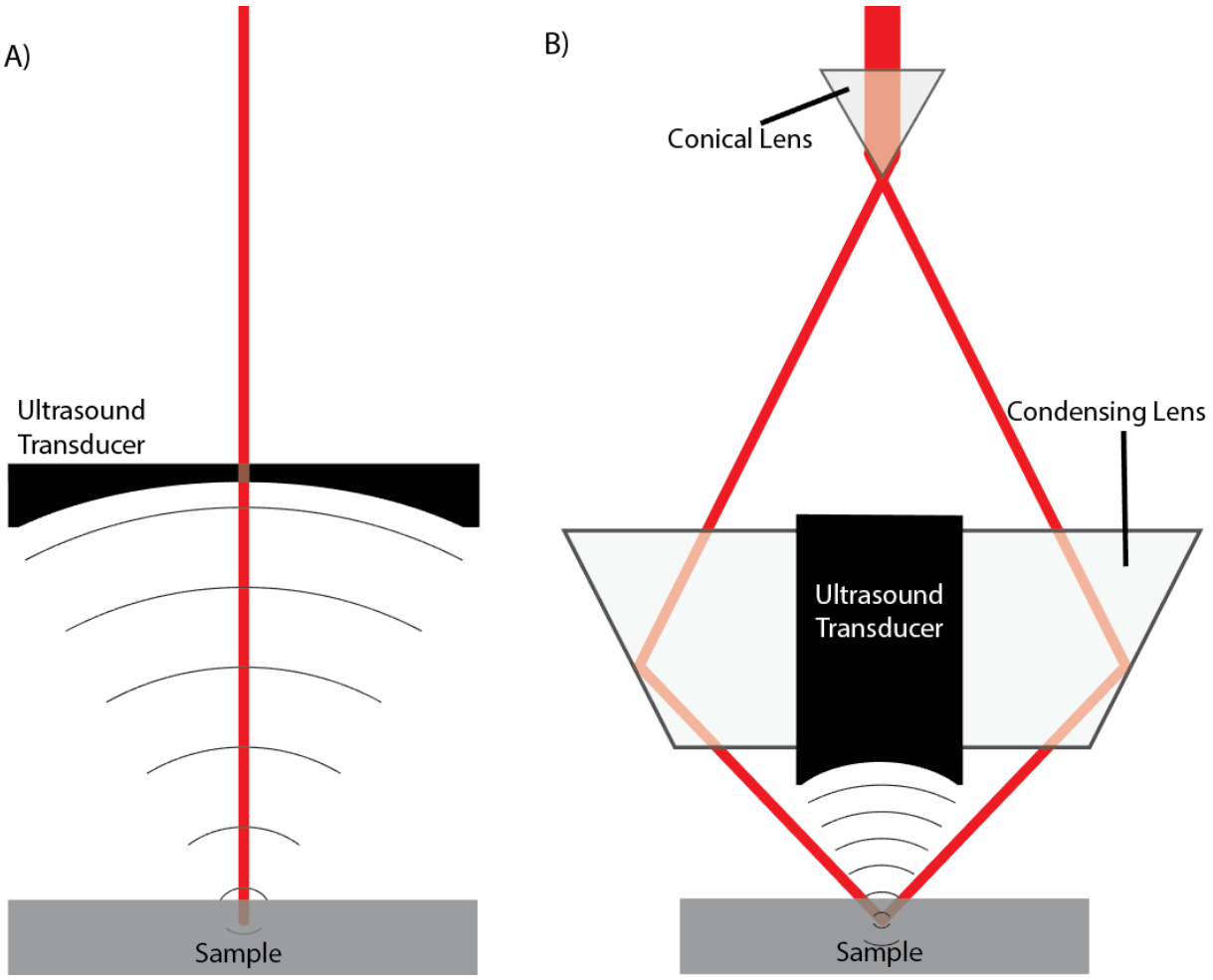

Figure 5.1: Cross sectional diagrams of two PUT treatment systems. (a) The laser beam is directed through a hole in the center of an ultrasound transducer. (b) The laser beam is shaped into a ring by a conical lens and then refocused using a condensing lens, directing the laser around an ultrasound transducer. In both configurations the laser and ultrasound are aligned and an optically transparent ultrasound coupling medium is used between the ultrasound transducer and the sample.

5.3 Methods

5.3.1 PA model

The PA pressure generated by a very short laser pulse (under stress and thermal confinement) can be simulated through the general PA equation (1) as described by Wang and Wu (L. V. Wang & H. Wu, 2007),

$$p(\vec{r},t) = \frac{1}{4\pi c^2}\frac{\partial}{\partial t}\left(\frac{1}{ct}\int p_0(\vec{r}')\delta\left(t - \frac{|\vec{r} - \vec{r}'|}{c}\right)d\vec{r}'\right) \quad (1)$$

where c is the speed of sound (1500 m/s), t is time, δ is Dirac delta function, and $\vec{r}$ is a location vector. The Dirac delta function in (1) is due to the travel time of pressure waves. The pressure that effects a given point over time is related to the generated pressure in an expanding spherical shell around that point. The integral in (1) is the summation of all the initial pressures along the shell.

The shell expands at the speed of sound allowing us to substitute ct for the radius of the shell. By using an axisymmetric geometry, and applying the Dirac delta function, the volume integral is simplified to a one-dimensional integral resulting in (2),

$$p(d,t) = \frac{1}{2}\frac{\partial}{\partial t}\left(t\int \mathrm{p}_0(t,\theta)\sin\theta\, d\theta\right) \quad (2)$$

where d is the depth into the sample along the axis, and θ is the polar angle from the central axis.

To use Equation (2) it is important to have an accurate model of initial pressure p_o, which is defined as

$$p_0(\vec{r}) = \Gamma A(\vec{r}) = \Gamma\mu_a F(\vec{r}) \quad (3)$$

where Γ is the Gruneisen parameter which was 0.81 in this study (Yao, Zhang, Maslov, & Wang, 2014), A is the local absorbance, μ_a is the optical absorption coefficient, and F is the local fluence. The relationship between the temperature increase and the local absorbance is defined by Wang and Wu in (4) (L. V. Wang & H. Wu, 2007),

$$\Delta T = \frac{A}{\rho C_v} \quad (4)$$

Where ΔT is the temperature increase, ρ is the density of the medium (1000 kg/m^3) and C_v is the specific heat at a constant volume (4000 J/(kg K)). By relating Equation (3) and Equation (4) an initial pressure of 1 MPa results in a temperature increase of 0.31 K.

The distribution of absorbance/fluence were determined by performing Monte Carlo photon transport simulation through MCML (L. Wang, Jacques, & Zheng, 1995). The pencil beam results of MCML were then convolved to describe the actual beam geometry. Equation (2) was solved to generate the PA pressure at various points along the central axis of the laser beam. In this study some of the simulations examined a normal incident beam, while others examined a focused laser beam as seen in some PA imaging systems (J. Jo & X. Yang, 2016) where the laser beam was spread into a ring and then refocused. Modeling of the focused beam geometry were performed by changing the launch conditions of the photon in the MCML simulation.

5.3.2 Bubble model

To model the dynamics of bubble expansion and collapse, the following equation (5) from Keller and Miksis was solved (Keller & Miksis, 1980):

$$\left(1-\frac{\dot{R}}{c}\right)R\ddot{R}+\frac{3}{2}\left(1-\frac{R}{3c}\right)\dot{R}^2=\frac{R}{\rho c}\frac{d}{dt}[p_B]+\frac{1}{\rho}\left(1+\frac{\dot{R}}{c}\right)\left(p_B-p_\infty-p\left(t+\frac{R}{c}\right)\right) \qquad (5)$$

Where R is the radius of the bubble, c is the speed of sound (1500 m/s), p_∞ is the pressure at infinity (101 kPa), $p(t + R/c)$ is the driving pressure, and p_B is the pressure in the medium at the boundary defined by:

$$p_B=\left(p_\infty+\frac{2\sigma}{R_0}\right)\left(\frac{R_0}{R}\right)^{3\eta}-\frac{2\sigma}{R}-\frac{4\mu}{R}\dot{R} \qquad (6)$$

Where σ is the surface tension (0.0725 N/m), R_o is the initial bubble radius, η is the polytropic exponent of the gas (1.4), and μ is the fluid viscosity (0.005 Pa·s).

The driving pressure was applied as a sinusoidal wave, representing the HIFU contribution, superimposed with the pressure wave derived by the PA model. The timing of the PA wave and the HIFU wave were synchronized so that the negative peak of the PA wave was aligned with the negative peak of the second ultrasound cycle. An initial bubble can be assumed to be present in the soft tissue as an initial nucleation site as described by Hynynen (Hynynen, 1991), therefore an initial bubble radius was supplied to the equation.

5.3.3 Simulations

Various samples were simulated through MCML and then Equation (2) was solved resulting in the PA wave over time at various depths. These results were then used as the driving pressure in Equation (5) to model the bubble dynamics. When solving Equation (5), two additional parameters, the amplitude of the ultrasound wave and the initial bubble radius, were supplied in two series of simulations. The first was using an initial bubble radius of 100 nm, while varying the amplitude of the ultrasound. The second used a constant amplitude for the ultrasound wave and varied the initial bubble size. The change in bubble radius would be modeled and then the maximum bubble size relative to the initial bubble size would be recorded. A simulation using the ultrasound wave without the addition of the PA waves, i.e., ultrasound-alone, was used as the reference. An example of these simulations is shown in Figure 5.2 with the results from ultrasound-alone and the changes caused by the addition of a PA wave. From these results three main values were extracted to represent the changes in cavitation. First was the cavitation threshold pressure for a 100 nm bubble, which represents the ultrasound pressure needed to cause an increase in bubble radius by a factor of 2. If the cavitation threshold pressure is lowered by the

addition of a PA wave, then a weaker ultrasound intensity could to initiate cavitation. Second was the cavitation threshold when using a constant ultrasound pressure wave and the initial bubble radius was varied. A decrease in this second cavitation threshold would indicate that smaller initial nucleation sites could be used to initiate cavitation. Finally, the maximum relative increase in bubble radius with a constant ultrasound wave represents the intensity of the resulting cavitation, where a larger maximum bubble radius causes stronger shockwaves upon bubble collapse. These three values were determined when ultrasound-alone was applied and compared to the results of the combined PA + ultrasound treatment. Simulations were performed using two main ultrasound parameters. The first was a 1 MHz wave with a 1 MPa amplitude, while the second was a 5 MHz wave with a 1.2 MHz amplitude. The amplitude of the wave was increased for the simulations using 5 MHz ultrasound wave so that the cavitation thresholds when using ultrasound-alone were similar.

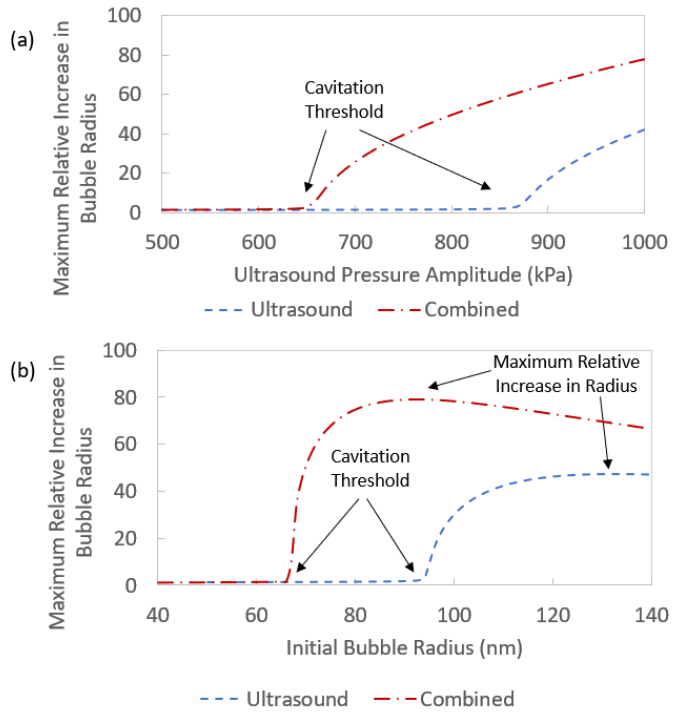

Figure 5.2: Example simulations of the relative maximum bubble size. Simulations using 1 MHz ultrasound alone and combined PUT are shown. (a) The results of the bubble simulation using a range of ultrasound amplitudes with a constant initial bubble size of 100 nm. The cavitation threshold is defined as the lowest pressure in which the maximum bubble size is twice the initial bubble size. (b) The results of the bubble simulations using a range of initial bubble sizes with a constant ultrasound pressure of 1 MPa at 1 MHz. The peak nucleation size is the bubbles size which has the largest relative maximum increase. The three identified values (cavitation threshold at constant initial bubble and constant ultrasound pressure, and the maximum relative increase in radius are used for comparisons further in the study to compare the level cavitation enhancement compared to ultrasound alone. The following parameters were used: Radiant exposure- 20 mJ/cm^2, Beam 1/e radius – 1 mm, μ_a – 100 cm^{-1}, μ_s – 100 cm^{-1}, g – 0.9, ultrasound wave 1 MHz with a 1 MPa amplitude.

Three main sets of simulation were used in this study. Group 1 involves the modeling of a single semi-infinite layer of tissue with changes to the optical absorption coefficient. Group 2 modeled multi-layer tissue, in this case, two layers of tissue, to examine the penetration ability of the treatments. The optical absorption coefficient was changed in the second layer, and all other

variable were held constant. Group 3 replicates the results in group 2, but the geometry of the laser beam was changed to a focused laser beam instead of a direct laser beam.

5.3.4 In vitro verification:

Enhanced surface ablation in a slab-shaped tissue phantom during PUT was demonstrated. Agar based slab-shaped tissue phantoms were created using a 2% solution of powdered agar (Agar pure powder, ThermoFisher Scientific, Waltham, MA) in the method described by Zell et al. (Zell et al., 2007). In order to create increased optical absorption a 0.06% concentration of cyan tattoo ink (Cyan, BZ Ink, Dragon tattoo supply, Dayton, OH) was added to create darker samples. The samples were made so that only one half contained the tattoo ink. The tissue phantoms were then placed in our PA imaging system as described in (Hazlewood & Yang, 2019). An electric motor was used to move the system across the surface of the sample for both imaging and treatment. A spherically focused HIFU transducer (SU-108-013, Sonic Concepts, Bothell, WA) was used to either detect the photoacoustic signal during imaging or to apply ultrasound waves at 5 MHz with a peak negative pressure of 3.6 MPa during treatment. A 532 nm pump laser (Surelight SLI-30, Continuum, Santa Clara, CA) and an OPO system (SLOPO Plus, Continuum, Santa Clara, CA) was used to deliver 5 ns pulses of 680 nm light 1.2 J/cm^2.

The samples were first imaged using the system for photoacoustic imaging. The system would move in a raster scan pattern across the surface of the sample. The pulse repetition frequency of 10 Hz determined the data acquisition rate. The maximum amplitude from each PA signal was used to create a 2D maximum amplitude projection of the sample. After photoacoustic imaging, the treatment would be applied as the system moved across the sample at a steady rate. After treating the samples, they were imaged under microscope to identify possible surface damage due

to enhanced cavitation. The treatments were repeated with HIFU alone, laser alone, and combined HIFU and laser, i.e., PUT.

5.4 Results

5.4.1 Group 1: Single semi-infinite slab

When the optical absorption for the tissue samples was modeled, the region of high absorption was a half spheroid (as seen in Figure 5.3), where the width of the half spheroid was based on the radius of the laser beam, and the depth was related to the optical properties of the sample. The resulting PA pressure wave had a positive and a negative portion. In PA waves near the surface (shown in Figure 5.4a) the positive portion had a much larger amplitude than the negative portion. However, the negative portion of the wave had a much longer duration. The PA waves deeper in the slab (shown in Figure 5.4c) had a more symmetric shape where the positive and negative portions of the wave were more similar in amplitude and duration. Additionally, the duration of the PA waves was shorter deeper in the slab. When the PA waves were superimposed and synchronized with the 1 MHz ultrasound waves (shown in Figure 5.4b and 5.4d) it can be seen that the negative portion of the surface PA wave completely encompassed the negative portion of the ultrasound wave. The deeper PA wave on the other hand, had a shorter duration therefore the positive phase of the PA wave canceled out a portion of the negative phase of the ultrasound. However, deeper PA wave had a stronger a peak negative pressure than the surface PA wave. When the 5 MHz ultrasound wave was superimposed over the deeper PA waves the duration of the negative phases were more similar, resulting in changes to the amplitude without dramatically changing the shape of the negative phase.

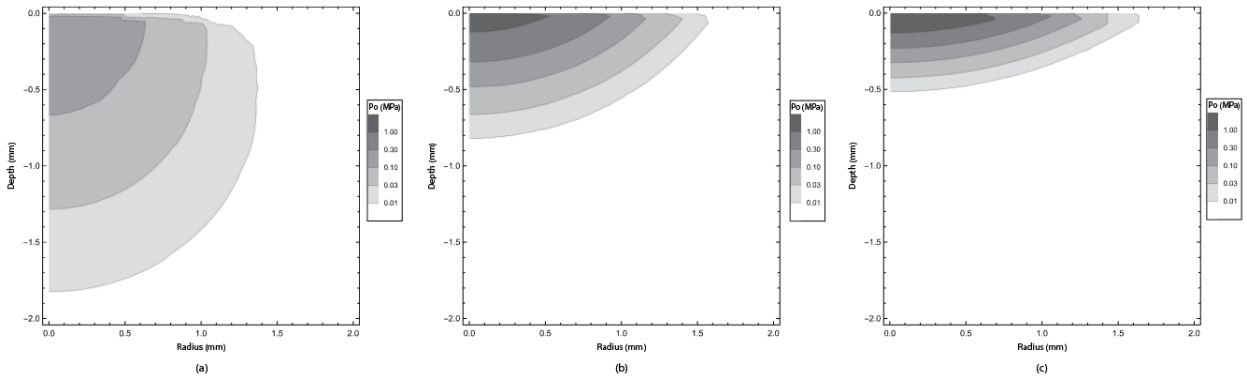

Figure 5.3: Contour plots of the initial pressure p_o found in group 1, which were 3 single slabs with different optical absorption coefficients. All three simulations were performed with constant laser parameters with a gaussian beam width of 1 mm, and a radiant exposure of 20 mJ/cm^2. The simulations used constant values for optical scattering coefficients (μ_s = 100 cm^{-1}) and anisotropy (g = 0.9), while the optical absorption coefficient was varied with (μ_a)= 5 cm^{-1}, 50 cm^{-1}, and 100 cm^{-1} for (a), (b), and (c) respectively. It can be seen that increased optical absorption increases the maximum initial pressure while decreasing the effective depth.

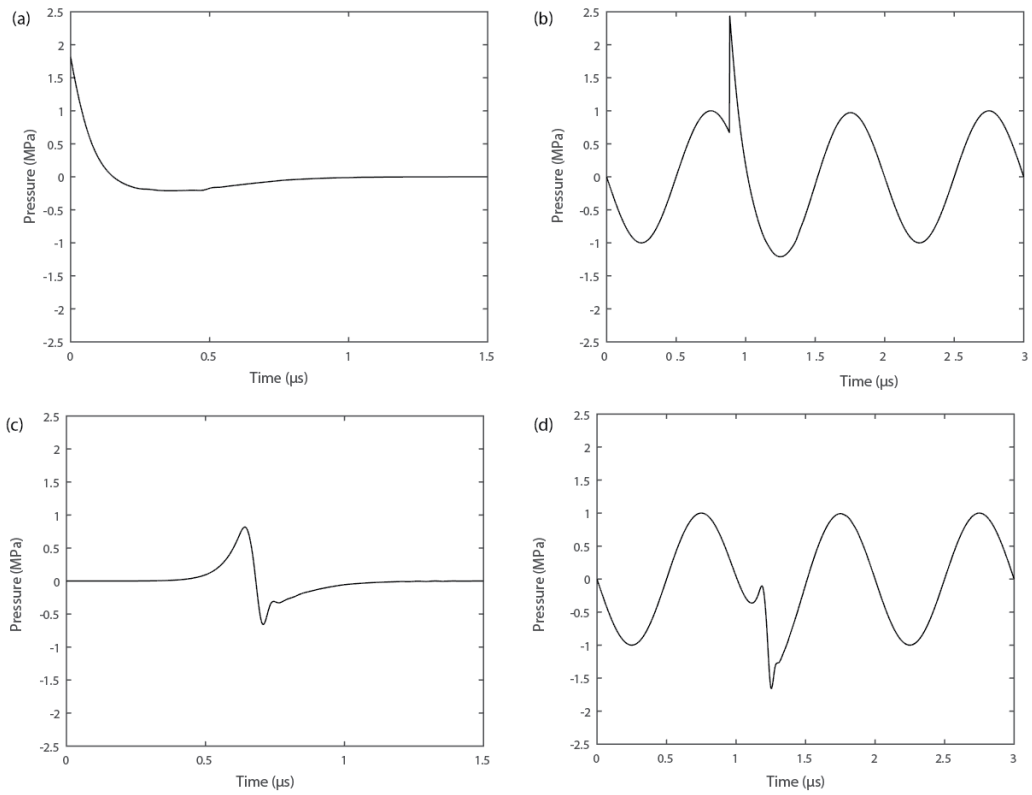

Figure 5.4: (a) The photoacoustic (PA) pressure wave generated at the surface of an optically absorbent slab. (b) The total pressure wave generated at the surface by PUT accounting for both the 1 MHz ultrasound and the PA wave. The most negative portion of the PA wave was synchronized with the bottom of the ultrasound wave. (c) The PA wave generated 1.5 mm inside an optically absorbent slab. (d) The total pressure 1.5 mm in the slab with both the PA wave and the 1 MHz ultrasound wave. The synchronization of the most negative portion of both waves was maintained. Simulations were performed with the following parameters: Radiant exposure- 20 mJ/cm^2, Beam 1/e radius – 1 mm, μ_a – 100 cm^{-1}, μ_s – 100 cm^{-1}, g – 0.9.

Figure 5.5 presents the results of the bubble dynamic simulations of three different semi-infinite slabs with the following optical properties: μ_a = 5, 50, and 100 cm^{-1}, μ_s = 200 cm^{-1}, and g = 0.9. These optical properties are similar to those seen in soft tissue using green laser light (Tuchin, 2007). The cavitation pressure threshold with constant initial bubble radius, the cavitation initial radius threshold with constant ultrasound pressure, and the maximum relative bubble radius under constant ultrasound pressure are all presented for each of the three slabs at a range of depths from the surface to 5 mm into the slab.

Increased optical absorption in the slab increases cavitation by reducing the threshold values or enhancing the maximum bubble radius through all three of the evaluated parameters. The greatest reduction in the cavitation thresholds is seen deeper in the samples with higher optical absorption, despite the results in Figure 5.3 showing that increased optical absorption decreases the penetration of the laser energy. The PA wave generated at the surface traveled into the slab to enhance cavitation. The change in the shape of the PA wave seen in Figure 5.4 affect the changes in cavitation. The wave generated at the surface which has a wide but shallow negative phase is less effective at lowering the cavitation thresholds. On the other had the PA waves seen deeper in the slab are more effective at lowering the cavitation thresholds. There is a small range, in the simulations using the 1 MHz ultrasound wave, where there is a transition between the surface PA wave and the deeper PA wave which did not enhance cavitation. During the transition the negative phase had a duration shorter than the ultrasound negative phase and had not developed the stronger peak negative pressures found in the deeper waves. These transitionary waves were less effective at enhancing cavitation. The simulations using the 5 MHz ultrasound wave did not have this effect, and demonstrated greater relative increase in maximum bubble radius with the deeper waves than the more surface waves. However the relative changes in cavitation thresholds were very similar when either 1 MHz of 5 MHz ultrasound was used.

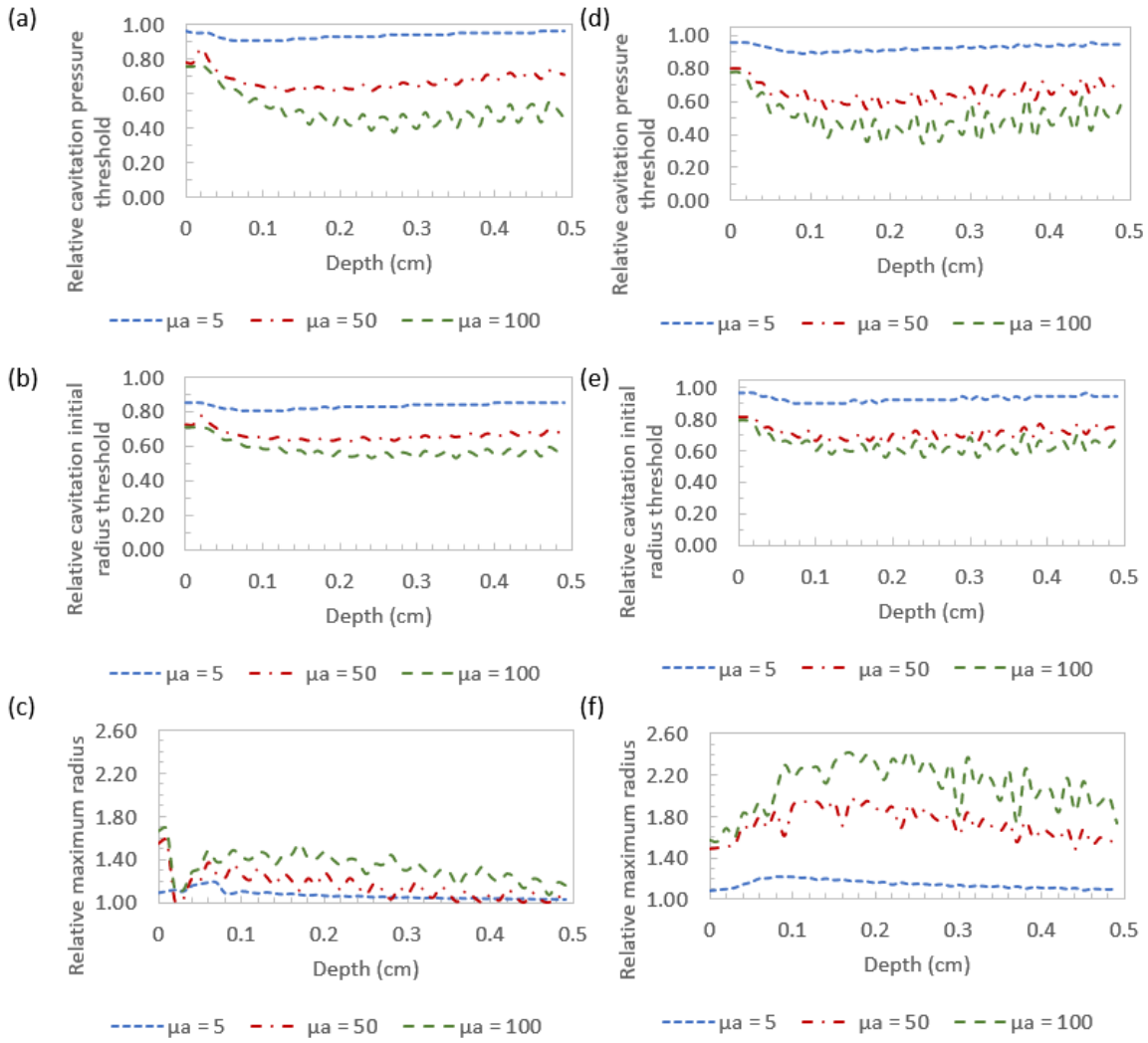

Figure 5.5: The overall results of group 1. A single layer was modeled with the following optical properties: μ_a = 5, 50, and 100 cm^{-1}, μ_s = 200 cm^{-1}, and g = 0.9. The laser beam had a 1/e radius of 1 mm and a radiant energy of 20 mJ/cm^2. All results are compared to an ultrasound-only control. (a-c) Simulations were performed with a 1 MHz ultrasound wave. (d-f) Simulations were performed with a 5 MHz ultrasound wave. (a,d) The change the inertial cavitation pressure threshold when a constant initial bubble radius of 100 nm was used, and the amplitude of the ultrasound pressure wave was changed. Lower values represent that cavitation can be initiated with a lower ultrasound intensity. (b,f) The change in inertial cavitation radius threshold when a constant ultrasound wave was used, and the initial bubble radius was changed. Lower values represent that smaller nucleation sites can be used to initiate cavitation. (c,d) The change in maximum relative bubble radius increase when the constant ultrasound wave. Increased maximum bubble size is associated with stronger shockwaves upon bubble collapse.

5.4.2 Group 2: Two slab model

It was found in preliminary simulations that when there was higher absorption in the top layer, there was not enough light absorbed by the deeper layer regardless of how high the optical absorption was. Instead the results were largely driven by the PA signal seen at the surface of the sample, leading to results nearly identical to those seen in group 1. This effect could result in enhanced cavitation in the deeper layer, but since the results were not related to the optical properties of the deeper layer the optical selectivity of the treatment was based on surface optical absorption, not the underlying tissues.

To better target the deeper layer, a new set of simulations with the following optical properties were performed: Top layer - $\mu_a = 0.2\ cm^{-1}$, $\mu_s = 10\ cm^{-1}$, $g = 0.8$, and thickness of 1.0 mm. Bottom layer - $\mu_a = 0.2, 10, 20\ cm^{-1}$, $\mu_s = 10\ cm^{-1}$, $g = 0.8$. These optical properties are similar to skin in the near infrared (NIR) range (Tuchin, 2007). The results are shown in Figure 5.6.

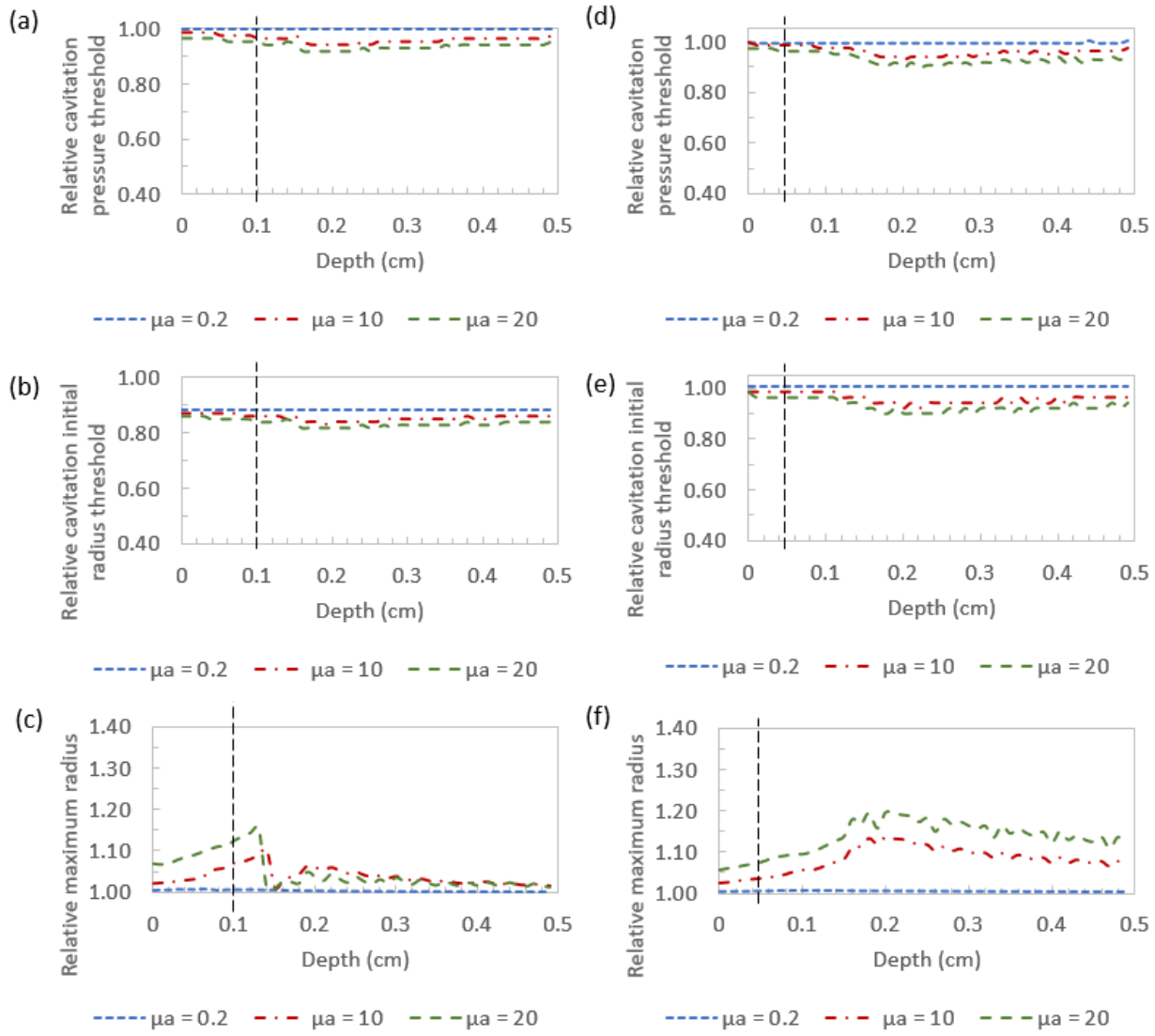

Figure 5.6: The overall results of group 2. A double layer model was used in three simulations with a constant top layer (μ_a = 0.2 cm^{-1}, μ_s = 10 cm^{-1}, g = 0.8, and thickness of 1.0 mm), and a second layer with various optical absorption coefficient values (μ_a = 0.2, 10, 20 cm^{-1}.) Vertical dashed line represents the interface between the two slabs. The laser beam had a 1/e radius of 1mm and a radiant energy of 20 mJ/cm^2. All results are relative to an ultrasound-only control. (a-c) A 1 MHz ultrasound wave was used. (d-f) A 5 MHz ultrasound wave was used. (a,d) Shows the changes in the inertial cavitation threshold when a constant initial bubble is used. (b,e) The change in inertial cavitation threshold when a constant ultrasound wave was used. (c,f) The change in peak nucleation. The simulation with the highest optical absorption caused the greatest enhancement in cavitation across all three metrics.

A slight enhancement in the second layer, indicated by reduced cavitation threshold due to the addition of the PA wave was observed in Figure 5.6. However, it was generally less enhancement than was seen previously in Group 1. This is largely due to the increased spreading of the light as it propagated through the first layer. The absorption of the light in the second layer was more diffuse, leading to a weaker PA signal that had a much smaller rarefaction pressure. Additionally, there was cavitation enhancement in the top layer due to a propagation of the PA wave from the deeper sample. The PA wave was largely generated in the second layer near the boundary, but it propagated both with and against the travel direction of the ultrasound wave. In these simulations the peak negative portions of the PA and ultrasound waves were synchronized at every point to determine maximum cavitation enhancement. In practice the cavitation enhancement in the first layer would be partially alleviated through the fact the negative peaks of the ultrasound and PA waves would drift out of and back into synchronization across the wavelength of the ultrasound.

5.4.3 Group 3: Two slab model with a focused laser illumination.

The focused laser beam geometry (Figure 5.1b) was applied to the NIR simulations performed in group 2 to increase the light fluence in the deep tissue. By selecting the laser ring radius to match the depth of the second layer, we focused the light on the surface of the second layer. A comparison between the initial pressure generated by the illumination seen using the direct geometry and the focused geometry is seen in Figure 5.7. A constant surface radiant exposure of 20 mJ/cm^2 was used for both illuminations, however it should be noted that this allowed for a greater total beam energy to be used with the focused laser geometry which had a larger surface area of illumination. The increased beam energy with a constant radiant exposure is one of the advantages of the focused geometry. Despite the higher total laser energy was used, the penetration into the second layer was shallower in the focused geometry than in the direct laser geometry.

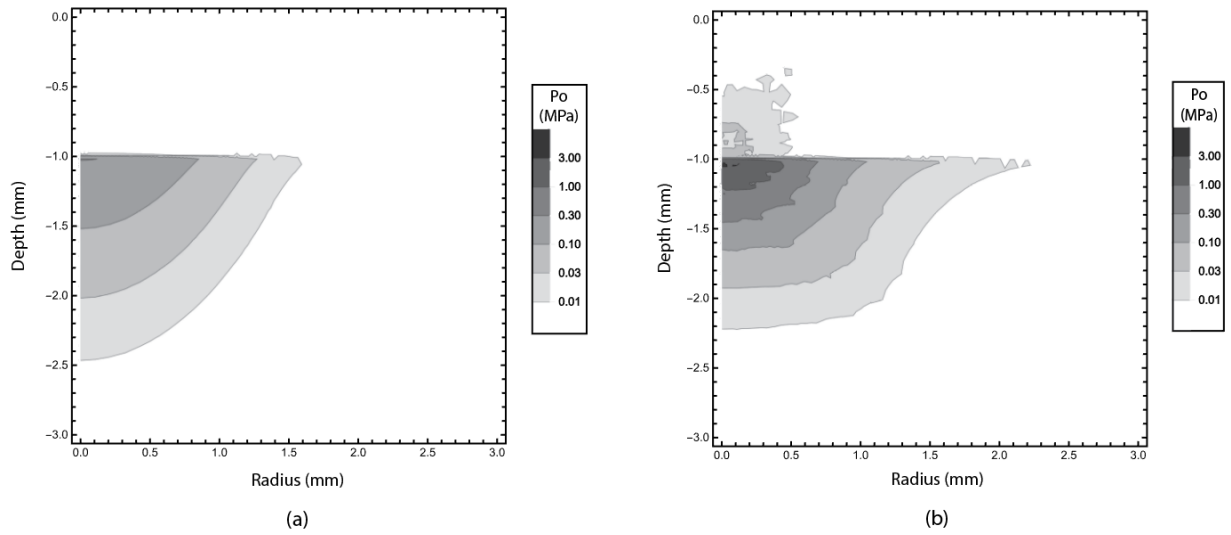

Figure 5.7: A comparison between two different illumination geometries (as seen in Figure 5.1) using the dual slab model in group 2 (bottom layer μ_a = 20 cm^{-1}). (a) Using the direct illumination as performed in group 2 with a 1/e radius of 1 mm. In this geometry the beam is normal to the surface of the sample. (b) Using a focused ring illumination, the entry angle of the laser was 45 degrees and internal and external 1/e radii of the ring were 0.5 and 1.5 mm respectively. A constant radiant exposure of 20 mJ/cm^2 was used for both illuminations. The focused illumination not only has a higher peak initial pressure, but it also results in a more rapid drop off in pressure moving away from the focal point, which increases the negative pressure in the resulting PA wave.

After simulating bubble dynamics for group 3 (shown in Figure 5.8), stronger cavitation enhancement was found at all depths when using the focused laser geometry compared the direct laser geometry. Additionally, cavitation enhancement was found in the second layer that was greater compared than the first layer, as demonstrated by the reduced cavitation thresholds and increased maximum bubble size. The increased contrast in cavitation enhancement seen in the two layers results in superior targeting of the targeted tissue.

When the focused geometry was used there were two main sources of PA waves. The first was from the path of the laser through the top layer, and the second was from the illuminated area in the bottom layer. There was a point just outside of the second layer where these two PA waves

interacted to create a second negative pressure peak with a very short duration when 1 MHz ultrasound wave was used. This second negative peak changed the synchronization for a small number of points which dramatically reduced the cavitation enhancement. When 5 MHz ultrasound wave was used the amplitude of this second negative peak was less significant and did not change the synchronization of the laser and ultrasound waves.

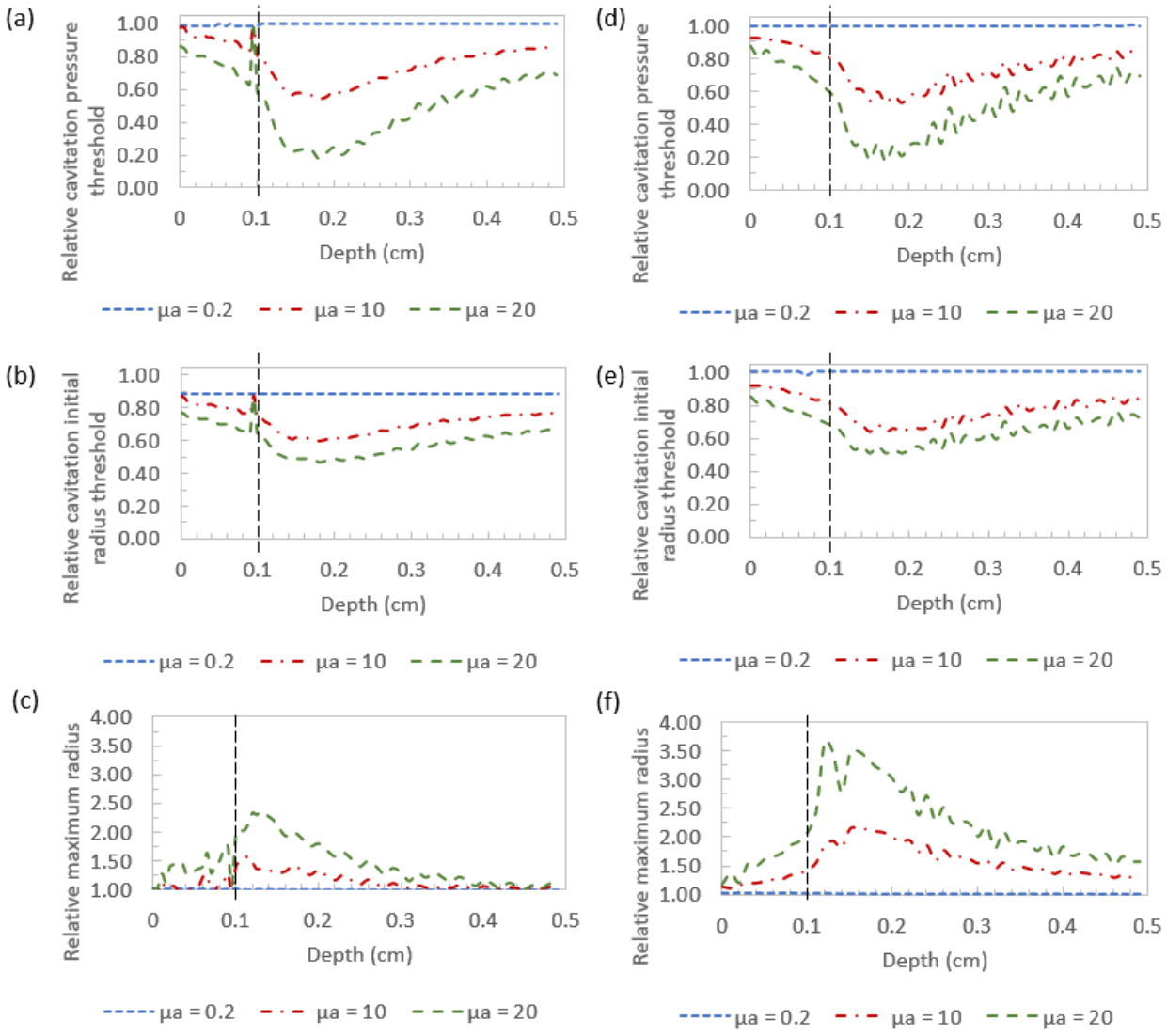

Figure 5.8: The results of the group 3 simulation using two slabs and a focused laser ring illumination. The optical properties of the slabs were identical to those used in group 2, but only the illumination geometry changed. The vertical dashed line identifies the interface between the two slabs. (a-c) A 1 MHz,

ultrasound wave was used. (d-f) A 5 MHz ultrasound wave was used. (a,d) Shows the changes in the inertial cavitation threshold when a constant initial bubble is used. (b,e) The change in inertial cavitation threshold when a constant ultrasound pressure amplitude is used. (c,f) The change in peak nucleation. The change in bubble behavior just before the interface between the two slabs is due to a brief change in synchronization from PA waves arriving from multiple directions.

5.4.4 Tissue phantom experiment

Enhanced cavitation activity during PUT can cause therapeutic effect which otherwise cannot be induced if cavitation activity is not enhanced. We designed a slab-shaped agar tissue phantom to experimentally confirm the potential therapeutic outcomes predicted by the simulations. The goal of the experiments is to demonstrate that PUT was able to selectively remove tissue phantoms based on optical absorption in a slab, with laser radiant exposures which are incapable of causing cavitation alone.

A tissue phantom made of two parts was made. The left side was dyed with black tattoo ink to increase the optical absorption, while the right was left undyed. The selectivity of combined laser and ultrasound ablation is shown in Figure 5.9. A portion of the half dyed, and half undyed sample was first imaged using photoacoustic imaging (Figure 5.9a) and the average PA signal was created from that image (Figure 5.9b). After imaging was performed, ultrasound-only, laser-only, and PUT treatments were performed across both sides of the sample. The ultrasound-only and PUT treatments used 0.2-ms bursts of 5 MHz waves with a peak negative pressure of 3.8 MPa. The laser-only and PUT treatments used a 5 ns pulse of 680 nm light with a radiant exposure of 1.2 J/cm^2 with a pulse repetition frequency (PRF) of 10 Hz. The peak negative pressure and radiant exposure of these treatments were lower than the 15.7 MPa (Zhou & Gao, 2013) and 8 J/cm^2 (V. Ross et al., 1998) used in other studies for ablations with ultrasound-only and laser-only

Removal of the tissue phantom material was clearly seen in the dyed region but was not seen in the undyed region when PUT was applied. When ultrasound or laser were used alone no ablation was seen. These results demonstrated the connection between increased PA signal and increased ablation during combined laser and ultrasound ablation.

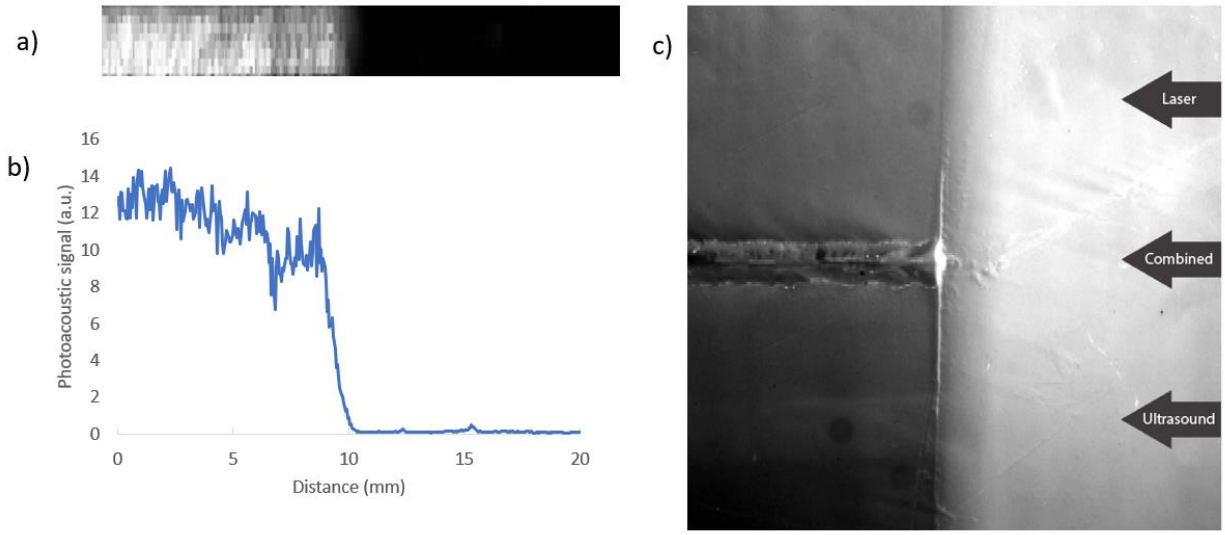

Figure 5.9: The experimental results using agar tissue phantoms. A) A maximum amplitude projection of the photoacoustic image taken before and after the PUT treatment. B) The mean PA signal from the photoacoustic image. C) A photograph of the sample after PUT treatment. Evidence of cavitation is seen in the more optically absorbent left side, while the right side which is less optically absorbent is undamaged. Treatments using laser alone had no effect on the sample, while ultrasound alone caused some minor changes to the surface of the sample.

5.5 Discussion

These results showed that PA pressure waves can be used to supplement HIFU on a wide slab-shaped tissue without spherical or cylindrical optical absorbers such as blood vessels or particles. Instead, the width of the laser beam provides a region of illumination that has an axisymmetric geometry. The axisymmetric geometry allows for the generation of a PA pressure wave with a rarefaction portion. Compared to more ideal optical absorbers such as spherical tattoo particles or

cylindrical blood vessels the PA pressure wave may not be as strong, however when it is used to supplement HIFU, it can increase cavitation activity in several ways. First the maximum relative bubble radius is increased, resulting in stronger shock waves when the bubbles collapse. Secondly the nucleation threshold is reduced allowing for smaller initial nucleation sites to initiate cavitation. And finally, the cavitation pressure threshold for a given bubble size is reduced allowing for cavitation to be triggered with a weaker ultrasound pulse.

Our simulations have also revealed that the PA wave that is generated at the surface of the soft tissue can propagate much deeper into the tissue than the penetration of the light directly. This may be beneficial towards treating tissues that are normally beyond the reach of laser therapies, such as tumors or thick scars. In fact, increased optical absorption reduces the effective depth of traditional laser treatments, however, using PA waves, the treatment on deeper tissues is more effective with increased optical absorption. It should be noted that under these conditions the optical selectivity of the laser treatment will be based on the optical absorption at the surface instead of the deeper tissues.

Alternatively, if the optical selectivity of the underlying tissue is needed, our simulations have shown that a focused laser beam geometry is more effective than a direct beam that is normal to the tissue surface. To properly target the underlying tissue, it is important that an appropriate wavelength is selected that has good penetration depth through the surface tissues to prevent a strong PA signal from the surface. Near infrared light is likely to be the preferred wavelength for such treatments as it can penetrate through skin easily. A potential target for those treatments would be collagen due to its relatively high optical absorption in the IR range. Additionally, it may be possible to artificially alter the optical properties of the tissue through dyes (Weber, Beard,

& Bohndiek, 2016) and/or optical clearing (Yu, Qi, Gong, Luo, & Zhu, 2018), in order to properly target the desired tissues.

When comparing the results of simulations using 1 MHz and 5 MHz ultrasound waves, a similar effect on the cavitation thresholds was seen with the addition PA waves. The 5 MHz ultrasound simulations had a larger relative increase in maximum bubble radius when comparing the combined treatments to the ultrasound-alone, however this is largely due to the fact that 5 MHz ultrasound alone is less effective at causing cavitation than 1 MHz ultrasound alone.

There are some notable limitations to this study, however the overall conclusions drawn from these simulations are expected to hold. First among them is the lack or accurate and consistent data on the optical properties of soft tissue over a wide range, and the nonhomogeneous nature of biological tissue. As such the optical properties used in this study are approximations only. Another limitation to this study is the heterogeneity of biological tissues, including the presence of reflections amongst different tissues. Due to the similarities in acoustic impedance in soft tissues (Duck, 1990), these reflections are expected to have approximately 1% of the amplitude of the incoming wave. Reflections of the acoustic waves at the surface can be minimized through the use of appropriate ultrasound coupling medium, which will be used to apply HIFU.

5.6 Conclusion

We have presented the results of simulations of slabs of tissue under PUT. The bubble dynamics under combined ultrasound and PA pressure waves were simulated, and changes in cavitation thresholds and maximum relative increase in bubble radius were used to quantify the enhancement in cavitation. It was found that the PA wave generated by the laser would enhance cavitation when compared to focused ultrasound treatments alone when optically absorbent semi-infinite slabs were targeted. The PA wave can travel deeper into the tissue than the laser light itself, allowing

for treatment beyond the range of typical laser therapies. We have also presented results showing that when targeting internal tissue, it is more effective to use a focused laser geometry, which counteracts the spreading of the laser light though the surface layers. These results show that PUT is effective in slabs of optically absorbent tissue even when cylindrical or spherical optical absorbers are not present, which allows PUT to be used in a wider range of applications.

Acknowledgments

This work was supported in part through a Department of Defense grant W81XWH-15-1-0524 and a National Institute of Health (NIH) grant R01EY029489. The authors have no conflict of interest to declare.

Chapter 6 - Conclusion

6.1 Summary

The results of this research have shown that mechanical ablation is possible using high intensity pulses of laser and/or ultrasound. In chapter 2 we developed and validated a new animal model for testing arthrofibrosis and joint contracture of the knee. In chapter 3 we developed a device capable of delivering pulsed high intensity laser (PHIL) and pulsed high intensity focused ultrasound (PHIFU), either separately or together. All three treatments were successful in completely restoring normal range of motion in the animal model. In chapter 4 we explored the effects of photo-mediated ultrasound therapy (PUT) on the surface of tissue phantoms. We were able to show that combined laser and ultrasound treatments were able to cause ablation to the surface with lower intensities than would be required for each alone. Finally, in chapter 5 we numerically simulated the changes in bubble behavior when PUT was applied to determine the changes to cavitation threshold, and to improve the effectiveness of PUT for future studies.

6.2 Findings

6.2.1 Chapter 2

The primary result from chapter 2 is that the new animal model for joint contracture through arthrofibrosis was successful. The model was found to be statistically significant through t-Test comparisons of the maximum extension of the knee. The stability of the model was determined using ANOVA, showing that the weekly changes were not statistically significant. To demonstrate that the contracture of the joint was indeed caused by arthrofibrosis, independent histological evaluation of the joints confirmed the presence of intra-articular scarring and peri-articular scarring.

The new animal model demonstrated several advantages over previous methods. The model was established using only a single surgery, without the use in implanted hardware. The single surgery is not only less invasive for the animals, but it also reduces the complications that may be introduced into the knee following a second surgery. The single surgery also allows for treatments to begin sooner, since there is a shorter overall recovery time. An additional advantage was that the damage to the posterior capsule was performed under direct visualization. This allowed for the surgeon to create consistent scarring.

Finally, it was also demonstrated repeated weekly measurements of knee ROM is possible without anesthetizing or sedating the animals. This was accomplished by training the rabbits to relax during measurements. This is an improvement over previous studies which required the animals the be euthanized, resulting in only a single data point per rabbit.

6.2.2 Chapter 3

The handheld device that could administer PHIFU, PHIL, or PUT was developed. The device consisted of a spherically focused HIFU transducer with a central hole, and a fiber optic cable to deliver the laser energy through the hole. A custom 3D printed casing was made to hold the laser fiber and transducer in proper alignment at all time, while also housing water for ultrasound transmission. The end result was a device which was able to be easily manipulated and applied to the animal during treatment.

The most important results in this chapter was that all of the rabbits that received PHIL, PHIFU, or PUT made a complete recovery, which was determined when model knee and the contralateral control knee had the same maximum extension. None of the control rabbits made a complete recovery, and the maximum extension over the study remained similar. Although we were able to

demonstrate that the improvements were statistically significant compared to the control, there were no statistically significant differences between each of the treatment groups in the current study.

All three of the treatment methods were very well tolerated by the animals which were left fully awake without sedation during the treatments. No pain or complications of any kind were seen due to the treatments, suggesting that the treatments are truly minimally invasive. This is thought to be impart due to the very short duration of the treatment pulses, which are shorter than a single action potential generated by pain receptors.

The independent histology evaluations of the rabbit knees showed that all three treatments had similar results. The scar tissue in and around the knee was still present, however it has a reduced density, and new vascularization had begun to occur. These results suggest that the ECM of the scar tissue had been disrupted and the joint had begun to return to normal.

6.2.3 Chapter 4

The principal results of chapter 4 were that PUT can cause ablation of the surface of tissue phantoms at intensity levels below those needed when only laser or ultrasound is applied. It was also demonstrated that this enhanced ablation is only present when the optical absorption of the targeted tissue is higher, allowing for self-targeting treatments when using the correct laser wavelength.

It was also found in this chapter that photoacoustic imaging (PAI) and PUT can be performed with the same system. The PAI can be used in two ways. First is to identify the region that will be affected by PUT. Secondly by changing the wavelength of the laser it is possible to identify which wavelength would be most effective for PUT.

Chapter 4 also examined the effects of changing the parameters PUT. As expected increasing the laser or ultrasound energy increased the area of ablation. It was also found that increasing the duration of the ultrasound pulse increased the area of ablation, even though the laser burst was approximately 5 ns long. This was further explored by changing the timing of the laser and ultrasound and demonstrating that only the portion of the ultrasound pulse that arrived after the laser would enhance cavitation. These results provide evidence that increasing the duration of the ultrasound pulse enhances ablation through cloud cavitation, where the shock wave generated by the collapse of one bubble causes cavitation in surrounding nucleation sites. The longer ultrasound pulse is suspected to enhance the cavitation in the rest of the cloud.

These results suggest that PUT may be valuable in tattoo removal, by determining the optimal wavelength to use and then performing the treatment at lower intensities to minimize complications.

6.2.4 Chapter 5

In Chapter 5 it was found that the photoacoustic (PA) wave generated by the laser hitting the surface of a slab of soft tissue generates a PAI wave is generated at the surface that is largely positive but has a long duration. As the wave travels deeper it has stronger peak negative pressure, but the duration is shorter. Both types of waves can cause or enhance cavitation, although the surface wave has a stronger effect on maximum bubble size while the deeper wave has a stronger effect on reducing the cavitation threshold.

If the optical absorption at the surface of the sample is high, then most of the laser energy will be absorbed very quickly. As a result, even if some of the laser energy reaches deeper tissues the PA wave from the deep tissue will be overpowered by the PA wave from the surface. The deeper

tissue will no longer be directly targeted by the laser. Instead the PA wave in the deeper tissue will be largely similar and be determined by the optical properties of the surface no matter what the optical properties of the deeper tissue are. To avoid this complication laser wavelengths with good penetration through the surface tissues should be used whenever targeting deeper tissues.

Chapter 5 identified an additional difficulty when targeting deeper tissues. To generate a strong PA wave, the laser energy should be concentrated, however as the laser light travels through the surface tissues some spreading will occur. As a result, the PA wave generated in deeper tissue is weaker.

To counteract the spreading of the laser beam, chapter 5 presented the results of targeting deeper tissues using a focused beam geometry. With a focused geometry the laser enters the skin in a ring at an angle that causes the laser energy to focus to a point. This has two benefits to producing a strong PA wave. First the laser light is more concentrated at the focal point, allowing for a smaller area to generate a stronger PA wave. Secondly the ring of illumination on the skin will have a larger radius when deeper tissues are targeted, which in turn increases the area of treatment. The total energy of the beam can be increased with the area to maintaining the same dosage of laser energy to any given point on the skin while increasing the amount of laser energy that can reach the focal point.

Chapter 5 performed simulations using optical properties which were comparable to those of the animals in Chapter 3. The result was that the laser energy was largely absorbed within the first millimeter, which in turn generated a PA wave that was able to reach over 5 mm deep (where the scar tissue was in chapter 3). This may contribute to why the results of PHIL, PHIFU, and PUT were so similar. The Chapter 5 results suggest that the PHIL treatment as performed in Chapter 3 was functioning in a very similar fashion to PHIFU. Because neither treatment was selectively

targeting the scar tissue based on its optical properties, PUT could not have been either. As a result, all three treatments were applying pressure waves to all the soft tissue of the knee.

6.3 Future work

6.3.1 Further investigation into the treatment of arthrofibrosis

Based on the complete recovery of all the treated animals in chapter 3, further development of these PHIL, PHIFU and PUT are warranted. Based on the results presented in the previous chapters, the following potential improvements can be recommended.

The wavelength of the laser used to target scar tissue should be changed to the near infrared range, where collagen has an absorption peak, but other soft tissues have very low optical absorption. This will allow for PHIL and PUT to selectively target the scar tissue as was originally intended. Additionally, the geometry of the laser delivery should be changed so it is delivered through a focused ring, which will allow for more efficient PA wave generation.

PAI of the joint using the system for PUT can be used to identify scar tissue prior to treatment. A low intensity laser pulse can be used, and the PA signal from the scar tissue can be detected through the ultrasound transducer. Once the location of the scar tissue has been detected more targeted treatments can be delivered. The change in laser wavelength and geometry allows the tissue at the focal point of the laser and ultrasound to be tested with minimal interference from the surface.

Different animal models for arthrofibrosis should be tested. Once PAI can be used it will be possible to detect scar tissue in the joint, and therefore prior knowledge of the location of the scarring is not needed. This allows for a wider variety of animal models to be tested including naturally occurring injuries.

A notable limitation to the research presented in this dissertation is a lack a specific information about some fundamental properties of scar tissue. For example, the optical properties of scar tissue have not been previously published, instead the properties of collagen-1 are used to represent scar tissue in general. Additionally, the acoustic properties of scar tissue have not been published but these properties determine what type of acoustic reflections may be present. Finally, the distribution in sizes of cavitation nucleation sites in various soft tissue is not known. Tissues which have larger nucleation sites would be more susceptible to cavitation-based treatments. An additional limitation to this research is these properties can be heterogeneous. Differences can be seen in different regions of various soft tissues, as well as changes over time.

6.3.2 Other applications of PUT

An important additional application for PUT could be the treatment of scars in the skin. In addition to new treatments for patients, investigation could lead to other insights into the treatment of scar tissue using PUT which may be applied to arthrofibrosis.

The results of chapter 4 demonstrate that PUT has potential as a new treatment for tattoo removal. PUT may be beneficial because it is able to perform photoacoustic analysis of the optical absorption of different tattoo dyes to identify the optimal laser wavelength to use. Furthermore, the reduced laser power needed for removal allow for the laser beam to be less focused, increasing the treatment spot size and reducing the time of each treatment.

Using the PAI and treatment potential for PUT, it may be possible to treat some cancers which are close to the surface of the skin. Cancers such as melanoma and breast cancer are likely candidates. Additionally, recent advancements in targeted drug delivery to cancer cells may also be used to deliver dyes to the tumors, which are not dangerous to other healthy cells that may also be affected.

The tumor could be identified through PAI, and then treatment could be immediately started wide area around the tumor to treat nearby cancer cells that have spread.

Appendix 1

Pain Assessment Scoring Scheme

Using the method described below, the use of analgesics will be based on the animal's clinical condition. The animals will be daily assessed for pain using the following pain assessment paradigm:

1. Standing
    a. 0 = continuous weight bearing
    b. 1 = intermittent weight bearing
    c. 2 = completely non-weight bearing
2. Gait with movement
    a. 0 = continuous weight bearing
    b. 1 = intermittent weight bearing
    c. 2 = toe touches, non-weight bearing
    d. 3 = completely non-weight bearing
3. Swelling
    a. 0 = none
    b. 1 = mild
    c. 2 = Pronounced
4. Pain on palpation of operated limb
    a. 0 = none
    b. 1 = mild pain (occasional vocalization)
    c. 2 = moderate pain (frequent vocalization)
    d. 3 = severe pain (vociferous vocalization, withdraws limb, bites, struggles)
5. Behavior
    a. 0 = normal cage exploration, food and water consumption, animal calm in cage
    b. 1 = minimal exploration, food and water consumption
    c. 2 = no cage exploration, hunched position – movement when stimulated, anorexic for 24 hrs
    d. 3 = no cage exploration, hunched position, piloerection, no movement, anorexic, increased respiratory rate or labored breathing
6. Body temp
    a. 0 = 101.3°F to 104°F
    b. 1 = > 103°F with lameness score of 5 or > 104°F with lameness score < 5
    c. 2 = > 104°F for 24 hrs post treatment and anorexic
    d. 3 = > 104°F for 48 hrs post treatment and anorexic
7. Appearance of incision site
    a. 0 = clean, no chewing, no redness
    b. 1 = mild chewing, redness, suture intact
    c. 2 = severe chewing, incision open
    d. 3 = incision infected (redness, swelling, purulent drainage)

Criteria for intervention

0-3 total score or ≤1 score in a category: No intervention

4-9 total score or >1 score in a category: Notify ACU veterinary personnel. Administer analgesic and re-evaluate pain score in 24 hours.

10-11 total score: Notify ACU veterinary personnel. Administer analgesic and re-evaluate pain score in 1 hr.

***** Obtained from the Animal Care Unit at the University of Kansas

References

Abdel, M. P., Morrey, M. E., Grill, D. E., Kolbert, C. P., An, K. N., Steinmann, S. P., . . . Morrey, B. F. (2012). Effects of joint contracture on the contralateral unoperated limb in a rabbit knee contracture model: a biomechanical and genetic study. *J Orthop Res, 30*(10), 1581-1585. doi:10.1002/jor.22106

Akai, M., Shirasaki, Y., & Tateishi, T. (1997). Electrical stimulation on joint contracture: an experiment in rat model with direct current. *Arch Phys Med Rehabil, 78*(4), 405-409.

Akeson, W. H., Woo, S. L., Amiel, D., & Doty, D. H. (1977). Rapid recovery from contracture in rabbit hindlimb. A correlative biomechanical and biochemical study. *Clin Orthop Relat Res*(122), 359-365.

Al-Turkaiki, M. H. S. (1986). The human knee : functional anatomy, biomechanics, and instabilities & assessment techniques. In (1st ed.. ed.). Al-Zulfi [Saudi Arabia]: Al-Zulfi Saudi Arabia : the author.

Altshuler, G. B., Anderson, R. R., Manstein, D., Zenzie, H. H., & Smirnov, M. Z. (2001). Extended theory of selective photothermolysis. *Lasers Surg Med, 29*(5), 416-432. doi:10.1002/lsm.1136

American National Standard for Safe Use of Lasers ANSI Z136.1-2007, § Section 8 (2007).

Anderson, R. R., & Parrish, J. A. (1983). Selective photothermolysis: precise microsurgery by selective absorption of pulsed radiation. *Science, 220*(4596), 524-527.

Apfel, R. E., & Holland, C. K. (1991). Gauging the likelihood of cavitation from short-pulse, low-duty cycle diagnostic ultrasound. *Ultrasound Med Biol, 17*(2), 179-185. doi:10.1016/0301-5629(91)90125-g

Barlow, J. D., Hartzler, R. U., Abdel, M. P., Morrey, M. E., An, K. N., Steinmann, S. P., . . . Sanchez-Sotelo, J. (2013). Surgical capsular release reduces flexion contracture in a rabbit model of arthrofibrosis. *J Orthop Res, 31*(10), 1529-1532. doi:10.1002/jor.22385

Beute, T. C., Miller, C. H., Timko, A. L., & Ross, E. V. (2008). In vitro spectral analysis of tattoo pigments. *Dermatol Surg, 34*(4), 508-515; discussion 515-506. doi:10.1111/j.1524-4725.2007.34096.x

Bogle, M. A., Ubelhoer, N., Weiss, R. A., Mayoral, F., & Kaminer, M. S. (2007). Evaluation of the multiple pass, low fluence algorithm for radiofrequency tightening of the lower face. *Lasers Surg Med, 39*(3), 210-217. doi:10.1002/lsm.20472

Brown, M. R. D., Farquhar-Smith, P., Williams, J. E., ter Haar, G., & deSouza, N. M. (2015). The use of high-intensity focused ultrasound as a novel treatment for painful conditions-a description and narrative review of the literature. *British Journal of Anaesthesia, 115*(4), 520-530. doi:10.1093/bja/aev302

Burgess, M. T., Apostolakis, I., & Konofagou, E. E. (2018). Power cavitation-guided blood-brain barrier opening with focused ultrasound and microbubbles. *Phys Med Biol, 63*(6), 065009. doi:10.1088/1361-6560/aab05c

Cheuy, V. A., Foran, J. R. H., Paxton, R. J., Bade, M. J., Zeni, J. A., & Stevens-Lapsley, J. E. (2017). Arthrofibrosis Associated With Total Knee Arthroplasty. *J Arthroplasty, 32*(8), 2604-2611. doi:10.1016/j.arth.2017.02.005

Chung, D. J., Cho, S. H., Lee, J. M., & Hahn, S. T. (2012). Effect of microbubble contrast agent during high intensity focused ultrasound ablation on rabbit liver in vivo. *Eur J Radiol, 81*(4), e519-523. doi:10.1016/j.ejrad.2011.06.002

Cosgarea, A. J., DeHaven, K. E., & Lovelock, J. E. (1994). The surgical treatment of arthrofibrosis of the knee. *Am J Sports Med, 22*(2), 184-191. doi:10.1177/036354659402200206

Cui, H., & Yang, X. (2011). Enhanced-heating effect during photoacoustic imaging-guided high-intensity focused ultrasound. *Applied Physics Letters, 99*(23), 3. doi:10.1063/1.3669441

Cui, H., & Yang, X. (2013). Laser enhanced high-intensity focused ultrasound thrombolysis: an in vitro study. *J Acoust Soc Am, 133*(2), EL123-128. doi:10.1121/1.4778375

Cui, H., Zhang, T., & Yang, X. (2013). Laser-enhanced cavitation during high intensity focused ultrasound: An in vivo study. *Appl Phys Lett, 102*(13), 133702. doi:10.1063/1.4800780

Cui, H. Z., Zhang, T., & Yang, X. M. (2013). Laser-enhanced cavitation during high intensity focused ultrasound: An in vivo study. *Applied Physics Letters, 102*(13), 4. doi:10.1063/1.4800780

Daoudi, K., Hoogenboom, M., den Brok, M., Eikelenboom, D., Adema, G. J., Futterer, J. J., & de Korte, C. L. (2017). In vivo photoacoustics and high frequency ultrasound imaging of mechanical high intensity focused ultrasound (HIFU) ablation. *Biomed Opt Express, 8*(4), 2235-2244. doi:10.1364/BOE.8.002235

Deng, C. X., Xu, Q., Apfel, R. E., & Holland, C. K. (1996). Inertial cavitation produced by pulsed ultrasound in controlled host media. *J Acoust Soc Am, 100*(2 Pt 1), 1199-1208. doi:10.1121/1.416304

Di Vita, G., Patti, R., D'Agostino, P., Caruso, G., Arcara, M., Buscemi, S., . . . Cillari, E. (2006). Cytokines and growth factors in wound drainage fluid from patients undergoing incisional hernia repair. *Wound Repair Regen, 14*(3), 259-264. doi:10.1111/j.1743-6109.2006.00120.x

Duck, F. A. (1990). Acoustic Properties of Tissue at Ultrasonic Frequencies. In F. A. Duck (Ed.), *Physical Properties of Tissues* (pp. 73-135). London: Academic Press.

El Agha, E., Kramann, R., Schneider, R. K., Li, X., Seeger, W., Humphreys, B. D., & Bellusci, S. (2017). Mesenchymal Stem Cells in Fibrotic Disease. *Cell Stem Cell, 21*(2), 166-177. doi:10.1016/j.stem.2017.07.011

Enad, J. G. (2014). Arthroscopic Lysis of Adhesions for the Stiff Total Knee Arthroplasty. *Arthroscopy Techniques, 3*(5), E611-E614. doi:10.1016/j.eats.2014.07.001

Enad, J. G. (2014). Arthroscopic lysis of adhesions for the stiff total knee arthroplasty. *Arthrosc Tech, 3*(5), e611-614. doi:10.1016/j.eats.2014.07.001

Everest, F. A. (2001). *The master handbook of acoustics* (4th ed.). New York: McGraw-Hill.

Facchetti, L., Schwaiger, B. J., Gersing, A. S., Guimaraes, J. B., Nardo, L., Majumdar, S., . . . Consortium, A.-A. (2017). Cyclops lesions detected by MRI are frequent findings after ACL surgical reconstruction but do not impact clinical outcome over 2 years. *European radiology, 27*(8), 3499-3508. doi:10.1007/s00330-016-4661-3

Farny, C. H., Wu, T., Holt, R. G., Murray, T. W., & Roy, R. A. (2005). Nucleating cavitation from laser-illuminated nano-particles. *Acoustics Research Letters Online, 6*(3), 138-143. doi:10.1121/1.1897823

Ferguson, M. W., & O'Kane, S. (2004). Scar-free healing: from embryonic mechanisms to adult therapeutic intervention. *Philos Trans R Soc Lond B Biol Sci, 359*(1445), 839-850. doi:10.1098/rstb.2004.1475

Feril, L. B., Jr., Tachibana, K., Ogawa, K., Yamaguchi, K., Solano, I. G., & Irie, Y. (2008). Therapeutic potential of low-intensity ultrasound (part 1): thermal and sonomechanical effects. *J Med Ultrason (2001), 35*(4), 153-160. doi:10.1007/s10396-008-0194-y

Finsterbush, A., & Friedman, B. (1973). Early changes in immobilized rabbits knee joints: a light and electron microscopic study. *Clin Orthop Relat Res*(92), 305-319.

Fitzsimmons, S. E., Vazquez, E. A., & Bronson, M. J. (2010). How to treat the stiff total knee arthroplasty?: a systematic review. *Clin Orthop Relat Res, 468*(4), 1096-1106. doi:10.1007/s11999-010-1230-y

Franca, K., Chacon, A., Ledon, J., Savas, J., Izakovic, J., & Nouri, K. (2013). Lasers for cutaneous congenital vascular lesions: a comprehensive overview and update. *Lasers Med Sci, 28*(4), 1197-1204. doi:10.1007/s10103-012-1220-2

Fukui, N., Fukuda, A., Kojima, K., Nakajima, K., Oda, H., & Nakamura, K. (2001). Suppression of fibrous adhesion by proteoglycan decorin. *J Orthop Res, 19*(3), 456-462. doi:10.1016/s0736-0266(00)90016-0

Fukui, N., Nakajima, K., Tashiro, T., Oda, H., & Nakamura, K. (2001). Neutralization of fibroblast growth factor-2 reduces intraarticular adhesions. *Clin Orthop Relat Res*(383), 250-258. doi:10.1097/00003086-200102000-00029

Fukui, N., Tashiro, T., Hiraoka, H., Oda, H., & Nakamura, K. (2000). Adhesion formation can be reduced by the suppression of transforming growth factor-beta1 activity. *J Orthop Res, 18*(2), 212-219. doi:10.1002/jor.1100180208

Fullerton, L. R., Jr., & Andrews, J. R. (1984). Mechanical block to extension following augmentation of the anterior cruciate ligament. A case report. *Am J Sports Med, 12*(2), 166-168. doi:10.1177/036354658401200215

Gan, S. D., & Graber, E. M. (2013). Laser hair removal: a review. *Dermatol Surg, 39*(6), 823-838. doi:10.1111/dsu.12116

Gasse, P., Mary, C., Guenon, I., Noulin, N., Charron, S., Schnyder-Candrian, S., . . . Couillin, I. (2007). IL-1R1/MyD88 signaling and the inflammasome are essential in pulmonary inflammation and fibrosis in mice. *The Journal of clinical investigation, 117*(12), 3786-3799. doi:10.1172/JCI32285

Ghani, H., Maffulli, N., & Khanduja, V. (2012). Management of stiffness following total knee arthroplasty: a systematic review. *Knee, 19*(6), 751-759. doi:10.1016/j.knee.2012.02.010

Golob, V., Jeler, S., & Gomilšek, J. P. n. (1996). Photoacoustic spectroscopy — A new method for dye identification in the substrate-dye system. *Dyes and Pigments, 31*(3), 233-244. doi:10.1016/0143-7208(95)00098-4

Gomes, J. L. E., Leie, M. A., de Freitas Soares, A., Ferrari, M. B., & Sanchez, G. (2017). Posterior Capsulotomy of the Knee: Treatment of Minimal Knee Extension Deficit. *Arthrosc Tech, 6*(5), e1535-e1539. doi:10.1016/j.eats.2017.06.033

Grevelink, J. M., Duke, D., van Leeuwen, R. L., Gonzalez, E., DeCoste, S. D., & Anderson, R. R. (1996). Laser treatment of tattoos in darkly pigmented patients: efficacy and side effects. *J Am Acad Dermatol, 34*(4), 653-656. doi:10.1016/s0190-9622(96)80068-5

Hallaj, I. M., & Cleveland, R. O. (1999). FDTD simulation of finite-amplitude pressure and temperature fields for biomedical ultrasound. *J Acoust Soc Am, 105*(5), L7-12. doi:10.1121/1.426776

Hartman, C. W., Ting, N. T., Moric, M., Berger, R. A., Rosenberg, A. G., & Della Valle, C. J. (2010). Revision total knee arthroplasty for stiffness. *J Arthroplasty, 25*(6 Suppl), 62-66. doi:10.1016/j.arth.2010.04.013

Hazlewood, D., Feng, Y., Lu, Q., Wang, J., & Yang, X. (2018). Treatment of post-traumatic joint contracture in a rabbit model using pulsed, high intensity laser and ultrasound. *Phys Med Biol, 63*(20), 205009. doi:10.1088/1361-6560/aadff0

Hazlewood, D., Feng, Y., Lu, Q., Yang, X., & Wang, J. (2018). Novel rabbit model of moderate knee contracture induced by direct capsular damage. *J Orthop Res*. doi:10.1002/jor.24038

Hazlewood, D., & Yang, X. (2019). Enhanced laser surface ablation with an integrated photoacoustic imaging and high intensity focused ultrasound system. *Lasers Surg Med*. doi:10.1002/lsm.23072

Hildebrand, K. A., Sutherland, C., & Zhang, M. (2004). Rabbit knee model of post-traumatic joint contractures: the long-term natural history of motion loss and myofibroblasts. *J Orthop Res, 22*(2), 313-320. doi:10.1016/j.orthres.2003.08.012

Hinz, B., Phan, S. H., Thannickal, V. J., Prunotto, M., Desmouliere, A., Varga, J., . . . Gabbiani, G. (2012). Recent developments in myofibroblast biology: paradigms for connective tissue remodeling. *The American journal of pathology, 180*(4), 1340-1355. doi:10.1016/j.ajpath.2012.02.004

Ho, D. D., London, R., Zimmerman, G. B., & Young, D. A. (2002). Laser-tattoo removal--a study of the mechanism and the optimal treatment strategy via computer simulations. *Lasers Surg Med, 30*(5), 389-397. doi:10.1002/lsm.10065

Ho, W. S., Chan, H. H., Ying, S. Y., & Chan, P. C. (2002). Laser treatment of congenital facial port-wine stains: long-term efficacy and complication in Chinese patients. *Lasers Surg Med, 30*(1), 44-47. doi:10.1002/lsm.10003

Hu, Z., Zhang, H., Mordovanakis, A., Paulus, Y. M., Liu, Q., Wang, X., & Yang, X. (2017). High-precision, non-invasive anti-microvascular approach via concurrent ultrasound and laser irradiation. *Scientific Reports, 7*, 40243. doi:10.1038/srep40243

Huang, J., Holt, R. G., Cleveland, R. O., & Roy, R. A. (2004a). Experimental validation of a tractable numerical model for focused ultrasound heating in flow-through tissue phantoms. *Journal of the Acoustical Society of America, 116*(4), 2451-2458. doi:10.1121/1.1787124

Huang, J., Holt, R. G., Cleveland, R. O., & Roy, R. A. (2004b). Experimental validation of a tractable numerical model for focused ultrasound heating in flow-through tissue phantoms. *J Acoust Soc Am, 116*(4 Pt 1), 2451-2458. doi:10.1121/1.1787124

Hutchinson, J. R., Parish, E. N., & Cross, M. J. (2005). Results of open arthrolysis for the treatment of stiffness after total knee replacement. *J Bone Joint Surg Br, 87*(10), 1357-1360. doi:10.1302/0301-620X.87B10.16228

Hutchinson, J. R. M., Parish, E. N., & Cross, M. J. (2005). Results of open arthrolysis for the treatment of stiffness after total knee replacement. *Journal of Bone & Joint Surgery, British Volume, 87-B*(10), 1357-1360. doi:10.1302/0301-620x.87b10.16228

Hwang, J. H., Zhou, Y., Warren, C., Brayman, A. A., & Crum, L. A. (2010). Targeted venous occlusion using pulsed high-intensity focused ultrasound. *IEEE Trans Biomed Eng, 57*(1), 37-40. doi:10.1109/TBME.2009.2029865

Hynynen, K. (1991). The threshold for thermally significant cavitation in dog's thigh muscle in vivo. *Ultrasound Med Biol, 17*(2), 157-169. doi:10.1016/0301-5629(91)90123-e

Hynynen, K., McDannold, N., Clement, G., Jolesz, F. A., Zadicario, E., Killiany, R., . . . Rosen, D. (2006). Pre-clinical testing of a phased array ultrasound system for MRI-guided noninvasive surgery of the brain--a primate study. *Eur J Radiol, 59*(2), 149-156. doi:10.1016/j.ejrad.2006.04.007

Ipach, I., Schafer, R., Lahrmann, J., & Kluba, T. (2011). Stiffness after knee arthrotomy: evaluation of prevalence and results after manipulation under anaesthesia. *Orthop Traumatol Surg Res, 97*(3), 292-296. doi:10.1016/j.otsr.2011.01.006

Issa, K., Kapadia, B. H., Kester, M., Khanuja, H. S., Delanois, R. E., & Mont, M. A. (2014). Clinical, objective, and functional outcomes of manipulation under anesthesia to treat knee stiffness following total knee arthroplasty. *J Arthroplasty, 29*(3), 548-552. doi:10.1016/j.arth.2013.07.046

Izikson, L., Farinelli, W., Sakamoto, F., Tannous, Z., & Anderson, R. R. (2010). Safety and effectiveness of black tattoo clearance in a pig model after a single treatment with a novel 758 nm 500 picosecond laser: a pilot study. *Lasers Surg Med, 42*(7), 640-646. doi:10.1002/lsm.20942

Jackson, D. W., & Schaefer, R. K. (1990). Cyclops syndrome: loss of extension following intra-articular anterior cruciate ligament reconstruction. *Arthroscopy, 6*(3), 171-178.

Jo, J., & Yang, X. (2016). Laser-enhanced high-intensity focused ultrasound heating in an in vivo small animal model. *Appl Phys Lett, 109*(21), 213702. doi:10.1063/1.4968509

Jo, J., & Yang, X. (2016). Laser-enhanced high-intensity focused ultrasound heating in an in vivo small animal model. *Applied Physics Letters, 109*(21), 213702. doi:doi:http://dx.doi.org/10.1063/1.4968509

Karabut, M. M., Gladkova, N. D., & Feldchtein, F. I. (2016). Fractional Laser Photothermolysis in the Treatment of Skin Defects: Possibilities and Effectiveness (Review). *Sovremennye Tehnologii V Medicine, 8*(2), 98-108. doi:10.17691/stm2016.8.2.14

Karu, T. (1987). Photobiological fundamentals of low-power laser therapy. *Ieee Journal of Quantum Electronics, 23*(10), 1703-1717. doi:10.1109/jqe.1987.1073236

Keller, J. B., & Miksis, M. (1980). Bubble oscillations of large amplitude. *The Journal of the Acoustical Society of America, 68*(2), 628-633. doi:10.1121/1.384720

Kendall, R. T., & Feghali-Bostwick, C. A. (2014). Fibroblasts in fibrosis: novel roles and mediators. *Frontiers in pharmacology, 5*, 123. doi:10.3389/fphar.2014.00123

Kent, K. M., & Graber, E. M. (2012). Laser tattoo removal: a review. *Dermatol Surg, 38*(1), 1-13. doi:10.1111/j.1524-4725.2011.02187.x

Kim, D. H., Gill, T. J., & Millett, P. J. (2004). Arthroscopic treatment of the arthrofibrotic knee. *Arthroscopy, 20 Suppl 2*, 187-194. doi:10.1016/j.arthro.2004.04.036

Klein, A., Baumler, W., Landthaler, M., & Babilas, P. (2011). Laser and IPL treatment of port-wine stains: therapy options, limitations, and practical aspects. *Lasers Med Sci, 26*(6), 845-859. doi:10.1007/s10103-011-0903-4

Kucera, T., Urban, K., Karpas, K., & Sponer, P. (2007). [Restricted motion after total knee arthroplasty]. *Acta Chir Orthop Traumatol Cech, 74*(5), 326-331.

Kuo, P.-L. (2010). Joint capsule loosening by high-intensity pulsed ultrasound. In (pp. 2111-2114): IEEE.

Kurosaka, M., Yoshiya, S., Mizuno, K., & Yamamoto, T. (2002). Maximizing flexion after total knee arthroplasty: the need and the pitfalls. *J Arthroplasty, 17*(4 Suppl 1), 59-62. doi:https://doi.org/10.1054/arth.2002.32688

Lam, L. O., Swift, S., & Shakespeare, D. (2003). Fixed flexion deformity and flexion after knee arthroplasty. What happens in the first 12 months after surgery and can a poor outcome be predicted? *Knee, 10*(2), 181-185. doi:10.1016/s0968-0160(02)00102-3

Laumann, A. E., & Derick, A. J. (2006). Tattoos and body piercings in the United States: a national data set. *J Am Acad Dermatol, 55*(3), 413-421. doi:10.1016/j.jaad.2006.03.026

Lavigne, A. B. W., R.P. (1972). Preliminary results on immobilisationinduced stiffness of monkey knee joints and posterior capsule. *Proceedings of the Biological Engineering Society*, 177-179.

Le, H. V., Lee, S. J., Nazarian, A., & Rodriguez, E. K. (2017). Adhesive capsulitis of the shoulder: review of pathophysiology and current clinical treatments. *Shoulder Elbow, 9*(2), 75-84. doi:10.1177/1758573216676786

Lee, H. S., Jang, W. S., Cha, Y. J., Choi, Y. H., Tak, Y., Hwang, E., . . . Kim, M. N. (2012). Multiple pass ultrasound tightening of skin laxity of the lower face and neck. *Dermatol Surg, 38*(1), 20-27. doi:10.1111/j.1524-4725.2011.02158.x

Leighton, T. G. (1994). *The Acoustic Bubble*: Academic Press.

Lewis, P. M., Thomson, R. H., Rosenfeld, J. V., & Fitzgerald, P. B. (2016). Brain Neuromodulation Techniques: A Review. *Neuroscientist, 22*(4), 406-421. doi:10.1177/1073858416646707

Li, S., Qin, Y., Wang, X., & Yang, X. (2018). Bubble growth in cylindrically-shaped optical absorbers during photo-mediated ultrasound therapy. *Phys Med Biol, 63*(12), 125017. doi:10.1088/1361-6560/aac7bc

Li, X., Yan, L., Wang, J., Sun, Y., Wang, Q., Lu, Z., . . . Hu, J. (2013). Comparison of the effects of mitomycin C and 10-hydroxycamptothecin on an experimental intraarticular adhesion model in rabbits. *Eur J Pharmacol, 703*(1-3), 42-45. doi:10.1016/j.ejphar.2013.02.001

Linares, H. A., Kischer, C. W., Dobrkovsky, M., & Larson, D. L. (1972). The histiotypic organization of the hypertrophic scar in humans. *J Invest Dermatol, 59*(4), 323-331.

Lowe, N. J., Lask, G., Griffin, M. E., Maxwell, A., Lowe, P., & Quilada, F. (1995). Skin resurfacing with the Ultrapulse carbon dioxide laser. Observations on 100 patients. *Dermatol Surg, 21*(12), 1025-1029. doi:10.1111/j.1524-4725.1995.tb00552.x

Loyola-Sanchez, A., Richardson, J., Beattie, K. A., Otero-Fuentes, C., Adachi, J. D., & MacIntyre, N. J. (2012). Effect of Low-Intensity Pulsed Ultrasound on the Cartilage Repair in People With Mild to Moderate Knee Osteoarthritis: A Double-Blinded, Randomized, Placebo-Controlled Pilot Study. *Archives of Physical Medicine and Rehabilitation, 93*(1), 35-42. doi:10.1016/j.apmr.2011.07.196

Madanshetty, S. I., Roy, R. A., & Apfel, R. E. (1991). Acoustic microcavitation: its active and passive acoustic detection. *J Acoust Soc Am, 90*(3), 1515-1526. doi:10.1121/1.401891

Mano, S., Palinkas, J., Szabo, J., Nagy, J. T., Bako, K., & Csernatony, Z. (2015). Application of a vibrating device for the prevention of flexion contracture after total knee arthroplasty. *Eur J Orthop Surg Traumatol, 25*(1), 167-172. doi:10.1007/s00590-014-1466-4

Manstein, D., Herron, G. S., Sink, R. K., Tanner, H., & Anderson, R. R. (2004). Fractional photothermolysis: a new concept for cutaneous remodeling using microscopic patterns of thermal injury. *Lasers Surg Med, 34*(5), 426-438. doi:10.1002/lsm.20048

Masciocchi, C., Conchiglia, A., Gregori, L. M., Arrigoni, F., Zugaro, L., & Barile, A. (2014). Critical role of HIFU in musculoskeletal interventions. *Radiologia Medica, 119*(7), 470-475. doi:10.1007/s11547-014-0414-z

Mayr, H. O., Weig, T. G., & Plitz, W. (2004). Arthrofibrosis following ACL reconstruction--reasons and outcome. *Arch Orthop Trauma Surg, 124*(8), 518-522. doi:10.1007/s00402-004-0718-x

McDonald, F. A., & Wetsel, G. C. (1978). Generalized theory of the photoacoustic effect. *Journal of Applied Physics, 49*(4), 2313-2322. doi:10.1063/1.325116

McLaughlan, J. R., Cowell, D. M. J., & Freear, S. (2017). Gold nanoparticle nucleated cavitation for enhanced high intensity focused ultrasound therapy. *Phys Med Biol, 63*(1), 015004. doi:10.1088/1361-6560/aa97e9

Medrado, A. R., Pugliese, L. S., Reis, S. R., & Andrade, Z. A. (2003). Influence of low level laser therapy on wound healing and its biological action upon myofibroblasts. *Lasers Surg Med, 32*(3), 239-244. doi:10.1002/lsm.10126

Mikula, J. D., Slette, E. L., Dahl, K. D., Montgomery, S. R., Dornan, G. J., O'Brien, L., . . . Hackett, T. R. (2017). Intraarticular arthrofibrosis of the knee alters patellofemoral contact biomechanics. *Journal of experimental orthopaedics, 4*(1), 40. doi:10.1186/s40634-017-0110-8

Mitsuyasu, H., Matsuda, S., Miura, H., Okazaki, K., Fukagawa, S., & Iwamoto, Y. (2011a). Flexion Contracture Persists If the Contracture is More Than 15 degrees at 3 Months After Total Knee Arthroplasty. *Journal of Arthroplasty, 26*(4), 639-643. doi:10.1016/j.arth.2010.04.023

Mitsuyasu, H., Matsuda, S., Miura, H., Okazaki, K., Fukagawa, S., & Iwamoto, Y. (2011b). Flexion contracture persists if the contracture is more than 15 degrees at 3 months after total knee arthroplasty. *J Arthroplasty, 26*(4), 639-643. doi:10.1016/j.arth.2010.04.023

Morrey, B. F., Askew, L. J., & Chao, E. Y. (1981). A biomechanical study of normal functional elbow motion. *J Bone Joint Surg Am, 63*(6), 872-877.

Moya-Angeler, J., Bas, M. A., Cooper, H. J., Hepinstall, M. S., Rodriguez, J. A., & Scuderi, G. R. (2017). Revision Arthroplasty for the Management of Stiffness After Primary TKA. *J Arthroplasty, 32*(6), 1935-1939. doi:10.1016/j.arth.2017.01.010

Naito, K., Watari, T., Muta, T., Furuhata, A., Iwase, H., Igarashi, M., . . . Kaneko, K. (2010). Low-Intensity Pulsed Ultrasound (LIPUS) Increases the Articular Cartilage Type II Collagen in a Rat Osteoarthritis Model. *Journal of Orthopaedic Research, 28*(3), 361-369. doi:10.1002/jor.20995

Nesterenko, S., Morrey, M. E., Abdel, M. P., An, K. N., Steinmann, S. P., Morrey, B. F., & Sanchez-Sotelo, J. (2009). New rabbit knee model of posttraumatic joint contracture: indirect capsular damage induces a severe contracture. *J Orthop Res, 27*(8), 1028-1032. doi:10.1002/jor.20845

Paltauf, G., & Schmidt-Kloiber, H. (1999). Photoacoustic cavitation in spherical and cylindrical absorbers. *Applied Physics A: Materials Science & Processing, 68*(5), 525-531. doi:10.1007/s003390050935

Perry, J. (1987). Contractures. A historical perspective. *Clin Orthop Relat Res*(219), 8-14.

Petsche, T. S., & Hutchinson, M. R. (1999). Loss of extension after reconstruction of the anterior cruciate ligament. *J Am Acad Orthop Surg, 7*(2), 119-127.

Ritter, M. A., Lutgring, J. D., Davis, K. E., Berend, M. E., Pierson, J. L., & Meneghini, R. M. (2007). The role of flexion contracture on outcomes in primary total knee arthroplasty. *J Arthroplasty, 22*(8), 1092-1096. doi:10.1016/j.arth.2006.11.009

Rodova, M., Lu, Q., Li, Y., Woodbury, B. G., Crist, J. D., Gardner, B. M., . . . Wang, J. (2011). Nfat1 regulates adult articular chondrocyte function through its age-dependent expression mediated by epigenetic histone methylation. *J Bone Miner Res, 26*(8), 1974-1986. doi:10.1002/jbmr.397

Ross, E. V., Domankevitz, Y., Skrobal, M., & Anderson, R. R. (1996). Effects of CO2 laser pulse duration in ablation and residual thermal damage: implications for skin resurfacing. *Lasers Surg Med, 19*(2), 123-129. doi:10.1002/(SICI)1096-9101(1996)19:2<123::AID-LSM1>3.0.CO;2-U

Ross, V., Naseef, G., Lin, G., Kelly, M., Michaud, N., Flotte, T. J., . . . Anderson, R. R. (1998). Comparison of responses of tattoos to picosecond and nanosecond Q-switched neodymium: YAG lasers. *Arch Dermatol, 134*(2), 167-171. doi:10.1001/archderm.134.2.167

Ruthenborg, R. J., Ban, J. J., Wazir, A., Takeda, N., & Kim, J. W. (2014). Regulation of wound healing and fibrosis by hypoxia and hypoxia-inducible factor-1. *Molecules and cells, 37*(9), 637-643. doi:10.14348/molcells.2014.0150

Rutherford, R. W., Jennings, J. M., Levy, D. L., Parisi, T. J., Martin, J. R., & Dennis, D. A. (2018). Revision Total Knee Arthroplasty for Arthrofibrosis. *J Arthroplasty, 33*(7S), S177-S181. doi:10.1016/j.arth.2018.03.037

Schairer, W. W., Vail, T. P., & Bozic, K. J. (2014). What Are the Rates and Causes of Hospital Readmission After Total Knee Arthroplasty? *Clinical Orthopaedics and Related Research, 472*(1), 181-187. doi:10.1007/s11999-013-3030-7

Schiavone Panni, A., Cerciello, S., Vasso, M., & Tartarone, M. (2009). Stiffness in total knee arthroplasty. *J Orthop Traumatol, 10*(3), 111-118. doi:10.1007/s10195-009-0054-6

Schiavone Panni, A., Cerciello, S., Vasso, M., & Tartarone, M. (2009). Stiffness in total knee arthroplasty. *Journal of Orthopaedics and Traumatology : Official Journal of the Italian Society of Orthopaedics and Traumatology, 10*(3), 111-118. doi:10.1007/s10195-009-0054-6

Schollmeier, G., Sarkar, K., Fukuhara, K., & Uhthoff, H. K. (1996). Structural and functional changes in the canine shoulder after cessation of immobilization. *Clin Orthop Relat Res*(323), 310-315. doi:10.1097/00003086-199602000-00044

Schwarzkopf, R., William, A., Deering, R. M., & Fitz, W. (2013). Arthroscopic lysis of adhesions for stiff total knee arthroplasty. *Orthopedics, 36*(12), e1544-1548.

Shah, M., Foreman, D. M., & Ferguson, M. W. (1994). Neutralising antibody to TGF-beta 1,2 reduces cutaneous scarring in adult rodents. *J Cell Sci, 107 (Pt 5)*(5), 1137-1157.

Shelbourne, K. D., & Patel, D. V. (1999). Treatment of limited motion after anterior cruciate ligament reconstruction. *Knee Surg Sports Traumatol Arthrosc, 7*(2), 85-92. doi:10.1007/s001670050127

Sivakumar, P., Kitson, C., & Jarai, G. (2019). Modeling and measuring extracellular matrix alterations in fibrosis: challenges and perspectives for antifibrotic drug discovery. *Connect Tissue Res, 60*(1), 62-70. doi:10.1080/03008207.2018.1500557

Steplewski, A., Fertala, J., Beredjiklian, P. K., Abboud, J. A., Wang, M. L., Namdari, S., . . . Fertala, A. (2016). Auxiliary proteins that facilitate formation of collagen-rich deposits in the posterior knee capsule in a rabbit-based joint contracture model. *J Orthop Res, 34*(3), 489-501. doi:10.1002/jor.23007

Steplewski, A., Fertala, J., Beredjiklian, P. K., Abboud, J. A., Wang, M. L. Y., Namdari, S., . . . Fertala, A. (2017). Blocking collagen fibril formation in injured knees reduces flexion contracture in a rabbit model. *J Orthop Res, 35*(5), 1038-1046. doi:10.1002/jor.23369

Stewart, N., Lim, A. C., Lowe, P. M., & Goodman, G. (2013). Lasers and laser-like devices: part one. *Australas J Dermatol, 54*(3), 173-183. doi:10.1111/ajd.12034

Tanzi, E. L., & Alster, T. S. (2002). Treatment of atrophic facial acne scars with a dual-mode Er:YAG laser. *Dermatol Surg, 28*(7), 551-555. doi:10.1046/j.1524-4725.2002.01319.x

Tardy, N., Thaunat, M., Sonnery-Cottet, B., Murphy, C., Chambat, P., & Fayard, J. M. (2016). Extension deficit after ACL reconstruction: Is open posterior release a safe and efficient procedure? *Knee, 23*(3), 465-471. doi:10.1016/j.knee.2016.01.001

Tavakkoli, J., & Sanghvi, N. (2011). Ultrasound-guided HIFU and Thermal Ablation. In (pp. 137-161).

ter Haar, G. (2007). Therapeutic applications of ultrasound. *Prog Biophys Mol Biol, 93*(1-3), 111-129. doi:10.1016/j.pbiomolbio.2006.07.005

Trafeli, J. P., Kwan, J. M., Meehan, K. J., Domankevitz, Y., Gilbert, S., Malomo, K., & Ross, E. V. (2007). Use of a long-pulse alexandrite laser in the treatment of superficial pigmented lesions. *Dermatol Surg, 33*(12), 1477-1482. doi:10.1111/j.1524-4725.2007.33319.x

Tsumaki, N., Kakiuchi, M., Sasaki, J., Ochi, T., & Yoshikawa, H. (2004). Low-intensity pulsed ultrasound accelerates maturation of callus in patients treated with opening-wedge high tibial osteotomy by hemicallotasis. *Journal of Bone and Joint Surgery-American Volume, 86A*(11), 2399-2405.

Tuchin, V. V. (2007). *Tissue optics : light scattering methods and instruments for medical diagnosis* (2nd ed.). Bellingham, Wash.: SPIE/International Society for Optical Engineering.

Tufail, Y., Yoshihiro, A., Pati, S., Li, M. M., & Tyler, W. J. (2011). Ultrasonic neuromodulation by brain stimulation with transcranial ultrasound. *Nat Protoc, 6*(9), 1453-1470. doi:10.1038/nprot.2011.371

Tung, Y. S., Vlachos, F., Feshitan, J. A., Borden, M. A., & Konofagou, E. E. (2011). The mechanism of interaction between focused ultrasound and microbubbles in blood-brain barrier opening in mice. *J Acoust Soc Am, 130*(5), 3059-3067. doi:10.1121/1.3646905

Tyler, W. J. (2011). Noninvasive neuromodulation with ultrasound? A continuum mechanics hypothesis. *Neuroscientist, 17*(1), 25-36. doi:10.1177/1073858409348066

Usher, K. M., Zhu, S., Mavropalias, G., Carrino, J. A., Zhao, J., & Xu, J. (2019). Pathological mechanisms and therapeutic outlooks for arthrofibrosis. *Bone Res, 7*(1), 9. doi:10.1038/s41413-019-0047-x

Usuba, M., Miyanaga, Y., Miyakawa, S., Maeshima, T., & Shirasaki, Y. (2006). Effect of heat in increasing the range of knee motion after the development of a joint contracture: An experiment with an animal model. *Archives of Physical Medicine and Rehabilitation, 87*(2), 247-253. doi:10.1016/j.apmr.2005.10.015

Vachon, P. (1999). Self-mutilation in rabbits following intramuscular ketamine-xylazine-acepromazine injections. *Can Vet J, 40*(8), 581-582.

van der Windt, D. A., van der Heijden, G. J., van den Berg, S. G., ter Riet, G., de Winter, A. F., & Bouter, L. M. (1999). Ultrasound therapy for musculoskeletal disorders: a systematic review. *Pain, 81*(3), 257-271. doi:10.1016/s0304-3959(99)00016-0

Vangipuram, R., Hamill, S. S., & Friedman, P. M. (2018). Accelerated tattoo removal with acoustic shock wave therapy in conjunction with a picosecond laser. *Lasers Surg Med, 50*(9), 890-892. doi:10.1002/lsm.22945

Wang, J. (2000). Spatial orientation of the microscopic elements of cortical repair bone. *Clin Orthop Relat Res*(374), 265-277. doi:10.1097/00003086-200005000-00024

Wang, J., Gardner, B. M., Lu, Q., Rodova, M., Woodbury, B. G., Yost, J. G., . . . Anderson, H. C. (2009). Transcription factor Nfat1 deficiency causes osteoarthritis through dysfunction of adult articular chondrocytes. *J Pathol, 219*(2), 163-172. doi:10.1002/path.2578

Wang, L., Jacques, S. L., & Zheng, L. (1995). MCML—Monte Carlo modeling of light transport in multi-layered tissues. *Computer Methods and Programs in Biomedicine, 47*(2), 131-146. doi:10.1016/0169-2607(95)01640-f

Wang, L. V., & Hu, S. (2012). Photoacoustic tomography: in vivo imaging from organelles to organs. *Science, 335*(6075), 1458-1462. doi:10.1126/science.1216210

Wang, L. V., & Wu, H.-i. (2007). *Biomedical optics : principles and imaging*. Hoboken, N.J.: Wiley-Interscience.

Wang, L. V., & Wu, H. (2007). *Biomedical Optics: Principles and Imaging*: Wiley.

Watson, R. S., Gouze, E., Levings, P. P., Bush, M. L., Kay, J. D., Jorgensen, M. S., . . . Ghivizzani, S. C. (2010). Gene delivery of TGF-beta1 induces arthrofibrosis and chondrometaplasia of synovium in vivo. *Laboratory investigation; a journal of technical methods and pathology, 90*(11), 1615-1627. doi:10.1038/labinvest.2010.145

Weber, J., Beard, P. C., & Bohndiek, S. E. (2016). Contrast agents for molecular photoacoustic imaging. *Nat Methods, 13*(8), 639-650. doi:10.1038/nmeth.3929

Werner, B. C., Cancienne, J. M., Miller, M. D., & Gwathmey, F. W. (2015). Incidence of Manipulation Under Anesthesia or Lysis of Adhesions After Arthroscopic Knee Surgery. *Am J Sports Med, 43*(7), 1656-1661. doi:10.1177/0363546515578660

Whiteside, P. J. D., Qian, C., Golda, N., & Hunt, H. K. (2017). Ultrasonic modulation of tissue optical properties in ex vivo porcine skin to improve transmitted transdermal laser intensity. *Lasers Surg Med, 49*(7), 666-674. doi:10.1002/lsm.22662

Wierer, G., Runer, A., Gfoller, P., Fink, C., & Hoser, C. (2017). Extension deficit after anterior cruciate ligament reconstruction: Is arthroscopic posterior release a safe and effective procedure? *Knee, 24*(1), 49-54. doi:10.1016/j.knee.2016.09.018

Williams, R., Havoonjian, H., Isagholian, K., Menaker, G., & Moy, R. (1998). A Clinical Study of Hair Removal Using the Long-pulsed Ruby Laser. *Dermatologic Surgery, 24*(8), 837-842. doi:10.1111/j.1524-4725.1998.tb04260.x

Wolin, P. M., Ingraffia-Welp, A., Moreyra, C. E., & Hutton, W. C. (2016). High-intensity stretch treatment for severe postoperative adhesive capsulitis of the shoulder. *Ann Phys Rehabil Med, 59*(4), 242-247. doi:10.1016/j.rehab.2016.04.010

Wong, K., Trudel, G., & Laneuville, O. (2015). Noninflammatory Joint Contractures Arising from Immobility: Animal Models to Future Treatments. *Biomed Res Int, 2015*, 848290. doi:10.1155/2015/848290

Woodward, J. A., Fabi, S. G., Alster, T., & Colon-Acevedo, B. (2014). Safety and efficacy of combining microfocused ultrasound with fractional CO2 laser resurfacing for lifting and tightening the face and neck. *Dermatol Surg, 40 Suppl 12*(12), S190-193. doi:10.1097/DSS.0000000000000228

Wu, X., Wang, H., Meng, C., Yang, S., Duan, D., Xu, W., . . . Zhao, J. (2015). Outcomes of arthroscopic arthrolysis for the post-traumatic elbow stiffness. *Knee Surg Sports Traumatol Arthrosc, 23*(9), 2715-2720. doi:10.1007/s00167-014-3032-3

Xu, L., Anderson, A. L., Lu, Q., & Wang, J. (2007). Role of fibrillar structure of collagenous carrier in bone sialoprotein-mediated matrix mineralization and osteoblast differentiation. *Biomaterials, 28*(4), 750-761. doi:10.1016/j.biomaterials.2006.09.022

Yao, D. K., Zhang, C., Maslov, K., & Wang, L. V. (2014). Photoacoustic measurement of the Gruneisen parameter of tissue. *J Biomed Opt, 19*(1), 17007. doi:10.1117/1.JBO.19.1.017007

Yeh, C. L., Li, P. C., Shih, W. P., Huang, P. S., & Kuo, P. L. (2013a). Imaging monitored loosening of dense fibrous tissues using high-intensity pulsed ultrasound. *Phys Med Biol, 58*(19), 6779-6796. doi:10.1088/0031-9155/58/19/6779

Yeh, C. L., Li, P. C., Shih, W. P., Huang, P. S., & Kuo, P. L. (2013b). Imaging monitored loosening of dense fibrous tissues using high-intensity pulsed ultrasound. *Physics in Medicine and Biology, 58*(19), 6779-6796. doi:10.1088/0031-9155/58/19/6779

Yu, T., Qi, Y., Gong, H., Luo, Q., & Zhu, D. (2018). Optical clearing for multiscale biological tissues. *J Biophotonics, 11*(2). doi:10.1002/jbio.201700187

Zabihian, B., Weingast, J., Liu, M., Zhang, E., Beard, P., Pehamberger, H., . . . Hermann, B. (2015). In vivo dual-modality photoacoustic and optical coherence tomography imaging of human dermatological pathologies. *Biomed Opt Express, 6*(9), 3163-3178. doi:10.1364/BOE.6.003163

Zell, K., Sperl, J. I., Vogel, M. W., Niessner, R., & Haisch, C. (2007). Acoustical properties of selected tissue phantom materials for ultrasound imaging. *Phys Med Biol, 52*(20), N475-484. doi:10.1088/0031-9155/52/20/N02

Zhang, H., Xie, X., Li, J., Qin, Y., Zhang, W., Cheng, Q., . . . Yang, X. (2018). Removal of choroidal vasculature using concurrently applied ultrasound bursts and nanosecond laser pulses. *Scientific Reports, 8*(1), 12848. doi:10.1038/s41598-018-31045-w

Zhang, H. F., Maslov, K., Stoica, G., & Wang, L. V. (2006). Functional photoacoustic microscopy for high-resolution and noninvasive in vivo imaging. *Nat Biotechnol, 24*(7), 848-851. doi:10.1038/nbt1220

Zhou, Y., & Gao, X. W. (2013). Variations of bubble cavitation and temperature elevation during lesion formation by high-intensity focused ultrasound. *J Acoust Soc Am, 134*(2), 1683-1694. doi:10.1121/1.4812895